Plasticity of the neuromuscular system in response to changes in dactyly

Inauguraldissertation

zur

Erlangung der Würde eines Doktors der Philosophie

vorgelegt der

Philosophisch-Naturwissenschaftlichen Fakultät

der Universität Basel

von

Bianka Anna Berki

Basel, 2022

Genehmigt von der Philosophisch-Naturwissenschaftlichen Fakultät auf Antrag von

Prof. Dr. Patrick Tschopp,

Prof. Dr. Dieter Ebert,

und Prof. Dr. Esther Stoeckli

Basel, den 16.11.2021

Prof. Dr. Marcel Mayor

Dekan

UNIVERSITY OF BASEL

Summary

Plasticity of the neuromuscular system in response to changes in dactyly

by Bianka Anna BERKI

Changes in limb morphology enabled the terrestrial lifestyle of tetrapods, as they adapted to different types of locomotion. The distal part of the limb – called the autopod, and encompassing the carpals/tarsals, metacarpals/metatarsals, and digits (fingers and toes) – in particular, went through drastic morphological changes during tetrapod evolution. Both digit patterns, as well as digit numbers, were modified during this process. While fossil data of stem-group tetrapods show that some ancestors possessed up to eight digits on one extremity, this number was reduced to five at the basis of the crown tetrapod group. Today, there is no known natural tetrapod population that surpasses the so-called 'pentadactyl state', and having more than five fingers is considered a pathology referred to as 'polydactyly'.

In the limb, not only the skeletal structure has to be modified during digit gains or losses, but also the soft tissues – like, e.g., the neuromuscular system - has to follow the skeletal changes, to form a fully functional unit. While polydactyly and the molecular alterations leading to it have been extensively studied at the skeletal level, little is known about the accompanying changes in the neuromuscular system.

The present work aims to bridge this gap, by studying the plasticity of the neuromuscular system in response to changes in digit numbers. First, we evaluated muscle and nerve patterns in the periphery of polydactyl limbs. Then, on a molecular and cellular level, we attempted to understand how muscle-specific motor neuron pools are modified in polydactyl individuals. We used chicken embryos, where *in-ovo* manipulation of the limb can result in mirror-image duplication of the digits, thus providing an ideal and well-established model for our study.

Using wholemount immunostaining of nerves and muscles followed by light sheet microscopy, we first reconstructed a 3D developmental time series of control wings and legs. There, our main finding uncovered a rotated pattern of the main nerve branches between wings and legs. Moreover, challenging the system with additional digits demonstrated a differential response of muscles and nerves in polydactyl limbs. Namely, while muscles seemed able to perfectly follow the pattern of skeletal mirror-image duplications, only two of the three main nerve branches responded and split to innervate the duplicated muscles.

These intriguing results motivated us to turn our attention toward the central nervous system. The cell bodies of limb-innervating motor neurons reside in the spinal cord and are organized into small subsets, so-called motor neuron pools. Each pool innervates one specific muscle, and the survival and maturation of these pools largely depend on target-muscle derived factors. The observed changes in innervation patterns pointed toward a potential modification of motor neuron survival and pool identity, a rationale we set out to explore in the second half of this thesis.

First, we showed that motor neuron numbers in the rostral LMC are decreased in the spinal cord of polydactyl individuals, due to increased cell death. This phenomenon was correlated to changes in the muscle patterns of the forearm, and the modification of fast versus slow muscle fiber composition in the limb, which might impair efficient innervation. In order to gain insights into the motor neuron pool compositions and transcriptomes, we performed, for the first time in chicken embryos, single-cell RNA-sequencing of spinal cord tissue. The resulting data identified putative digit-specific motoneuron pool markers but indicated only minor differences in cell-type distribution between polydactyl and control neural tubes. However, the traditional emulsion-based method might have failed to capture high enough numbers of motor neurons. Accordingly, we focused on a different, more direct approach, for an in-depth study of motor neuron pools innervating native and duplicated muscles in polydactyl embryos.

To this aim, we developed a method combining ex-ovo retrograde axonal labeling, manual purification of neurons, and the highly sensitive Smart-seq2 single-cell RNA-sequencing technique. Our results showed that our method is efficient in extracting embryonic motor neurons, that it captures a high number of genes per cellular transcriptome, and therefore represents a valuable tool for studying motor circuit formation. Preliminary comparative transcriptomic analysis of neurons coming from two motor neuron pools – innervating the EMR and FDQ wing muscles - revealed unique pool-specific signatures and further validated our technique.

Collectively, in the present thesis work, we describe the plasticity of the neuromuscular system in response to polydactyly, and how muscles and nerves integrate changes in the skeletal patterning. Furthermore, we show that changes in muscle identity and shifts in muscle fiber composition can affect motor neuron survival. Also, we developed a technique to study in great detail the transcriptomes of muscle-specific motoneurons, and we intend to use this methodology to better understand neuronal wiring and molecular muscle-neuron cross-talk during circuit formation. Our data provide the basis for further developmental studies and offer a framework for medical research, in order to better understand the etiologies of human polydactyl phenotypes.

Acknowledgements

First, I would like to thank **Prof. Dr. Esther Stoeckli** and **Prof. Dr. Dieter Ebert** for accepting to evaluate my work and to be present at my doctoral examination.

I would like to thank **Patrick Tschopp** for allowing me to do my PhD in his laboratory and for creating the perfect work environment for me to carry out my work. I would also like to thank you for guiding me through the difficult task of writing this manuscript.

My deepest gratitude goes to **Maëva Luxey** for her supervision, constant encouragement, and all the scientific and personal discussions we had throughout the years. Your good humor helped to lighten the mood, and your scientific knowledge guided me toward the successful completion of this work.

Thanks to all past and present members of the Tschopp lab, **Sabrina, Emmanuelle, Aline, Ana, Gabriela, Gabriele, Antoine, Alex, Fabio, Nico, Navaneeth, and Menghan** for all the fun moments, all the Friday Beer o'clock we had together, and please don't forget to take care of the plants once I am gone! I am deeply grateful to **Christian** for being a great friend and hiking partner, I hope to be back in the mountains with you very soon.

I am grateful to **Virginie, Selen, Erika, Lin, Roland, Tiago, Nassim** and all the other members of *'d Räppli Huus* for being awesome, becoming my second family during the year 2020 and helping me stay mentally sane during those difficult times.

I would also like to thank **Cassandra** and **Enikő** for their amazing friendship and support, and **Tina** for guiding me toward a more balanced and happier lifestyle. **Matthias**, thank you for making me see the beauty in evolution and paleontology. Your patience and amazing company made this past year so much easier and happier!

Végtelen hálával tartozom szüleimnek, akik egyetlen pillanatig sem kételkedtek abban, hogy eljutok idáig és képes leszek teljesíteni ezt a nehéz feledatot. Köszönöm Nektek, hogy támogattatok azóta hogy 2012-ben nekiindultam a nagyvilágnak és remélem viszonozni tudom egy nap mindazt amit értem tettetek.

I am grateful to my brother, **Gergő** and my sister-in-law, **Réka** for their moral support and kindness in moments of difficulty.

Lastly, I would like to thank the financial support of the Swiss National Science Foundation and the University of Basel as this work could not have been carried out without them.

Contents

List of Figures

Chapter 1

General introduction

1.1 A brief evolutionary history of the distal tetrapod limb

Species' character traits are constantly evolving in order to respond to an ever-changing environment and to aid in adapting to new ecological niches. As an example, the success of tetrapods lies in their ability to first evolve an amphibious and finally a completely terrestrial lifestyle. Indeed, from the Cambrian explosion ($\sim$ 520 million years ago (mya)) until the Upper Devonian period ($\sim$ 375 mya) vertebrates were restricted to aquatic environments [1]. The evolution of the tetrapod limb is closely connected to the transition from water to land. The origin of limbs is often traced back to the emergence of paired fins. The first pectoral paired appendages already appeared in jawless fishes (Agnatha), but only jawed fishes (Gnathostomata) possess pectoral and pelvic sets of fins [2–4]. Around 425 mya, in the late Silurian, gnathostomes then branched into ray-finned fish (Actinopterygii) and lobe-finned fish (Sarcopterigii). While Actinopterygians count for most extant fish groups, sarcopterygian comprise lungfish, coelacanths and tetrapods [5, 6].

At a skeletal level, the fins in these two clades are fundamentally different. The actinopterygian fin is wide at the base, with only a few parallel endoskeletal radials but most of the structure is composed of dermal fin rays, called lepidotrichia. On the other hand, in lobe-finned fish the endoskeletal part is expanded as dermal bones become reduced, while the fin is connected to the shoulder/pelvic girdle by a single articulated bone, the humerus-like (pectoral fin) or femur-like (pelvic fin) structure [7, 8]. This major change provided a better rotation and mobility than radials. The presence of ossified bones and the more slender shape of the fin brought about changes in the neuromuscular system as the fin could support muscles and the motor nerves started to organize into plexus at the base of the fin [9, 10].

Bones homologous to the humerus/femur (stylopod) and radius-ulna/tibia-fibula (zeugopod) of extant tetrapods appeared in the early Devonian [11]. However, the autopod (hand/feet, including carpal bones, metacarpals, and fingers) appeared later, once stem-tetrapods supposedly started an amphibious lifestyle. The first described Upper Devonian tetrapods with 'true' digits on their limbs were *Ichthyostega*, *Acanthostega*

and *Tulerpeton* (Figure 1) [12–14]. In living tetrapods, the autopod, especially the digits, are important for locomotion, traction, distribution of the weight of the animal across the limbs, and later for finer motor skills such as grabbing and object manipulation.

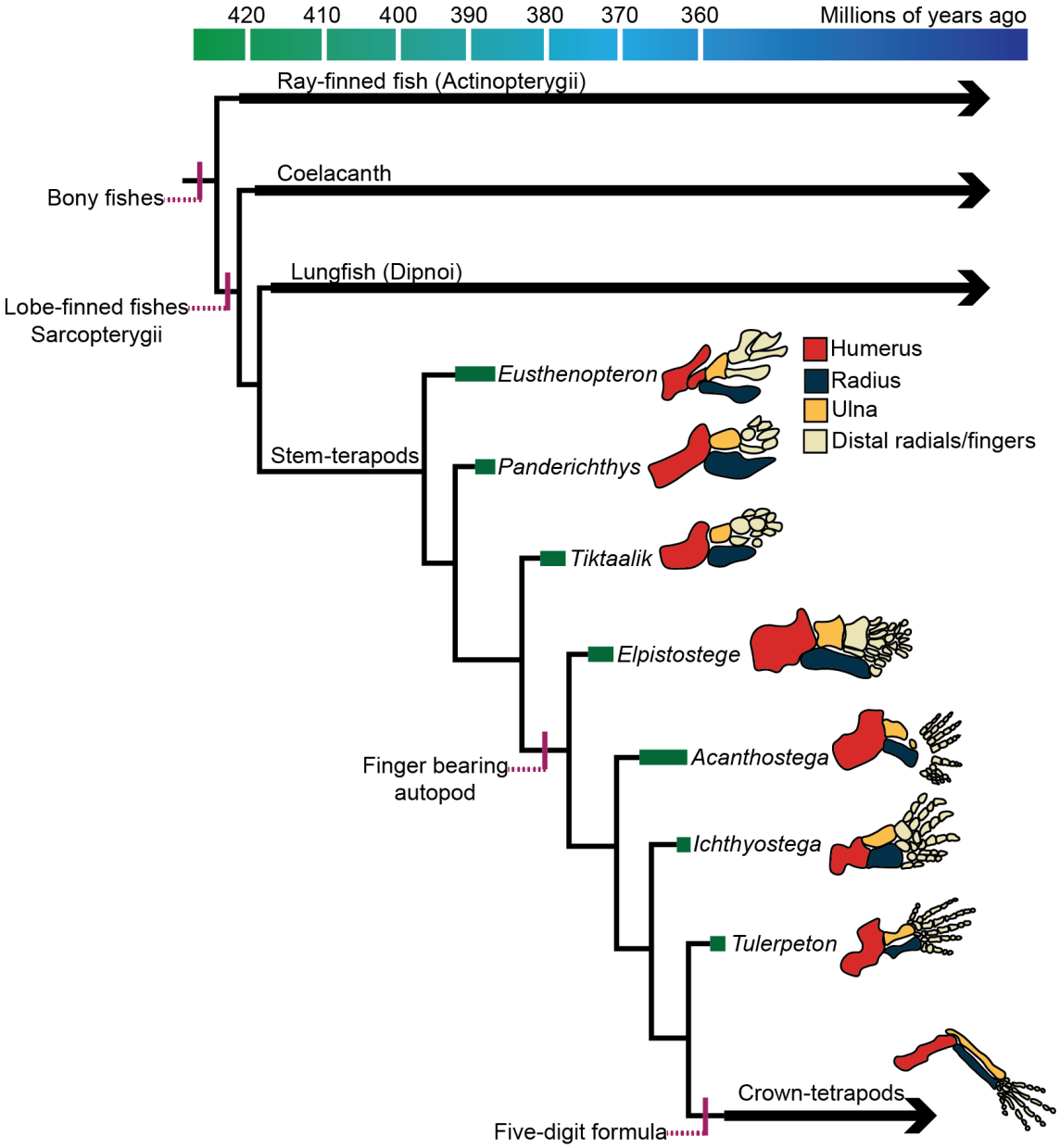

Figure 1: A brief history of the tetrapod limb A timed phylogenetic tree showcasing the changes of the limb structure in stem-tetrapod fossils. Figure adapted from [15, 16].

The way digits emerged in tetrapods is fairly controversial based on available fossil and developmental data. Two major theories were put forward regarding the origin of the digits: 1) digits are evolutionary novelties; 2) distal radials of sarcopterygian fins are at the origin of digits [17–21]. The first theory is supported by developmental genetic data comparing zebrafish and mouse Hox gene expression in fin folds/limb buds, which presumed that there is no homologous territory to the autopod region in ray-finned fish [22]. Furthermore, the activation of HOXD genes in the presumptive digit area depends

on a cis-regulatory system unique to tetrapods which also points toward a neomorphic nature of digits [23].

From a paleontological point of view, the 21st century brought about new fossil evidence in the form of *Tiktaalik roseae*, a stem tetrapod more closely related to crown tetrapods than previously found fossil species like *Eusthenopteron* or *Panderichthys* (Figure 1) [24]. The fin of *Tiktaalik* presents tetrapod-like proximal bones and small, distal endochondral bones, that can be interpreted as a primitive form of autopod bones, potentially digits. Moreover, CT scan analysis of a new intact *Panderichthys* pelvic fin showed similar small distal bones as *Tiktaalik* [25]. The recently recovered intact pelvic fin of *Elpistostege watsoni* – positioned between *Tiktaalik* and *Acanthostega* in the phylogeny, hence being the closest known relative of the finger-bearing tetrapods - showed that the distal radials are arranged in two rows of presumed carpals and two rows of putative digits in this animal [16].

Despite these paleontological and developmental data, it is difficult to pronounce a definite verdict on the potential neomorphic nature of the fingers. Additional fossils need to be recovered from the period of fin-to-(digit-bearing) limb transition in order to uncover the origin of digits.

An interesting phenomenon observed in stem- and crown-tetrapods is the variation of digit numbers. Namely, in extant tetrapods, only five digits or less are found in natural populations and a pentadactyl constraint is seemingly established. The condition of having more than five fingers on hands and feet is called polydactyly. Although the last common ancestor of the crown-group tetrapod was supposedly pentadactyl, autopods with more than five digits were recurrent in the stem-tetrapods. Indeed, *Ichthyostega* had seven digits on the hind limb, while the digit formula of the forelimb is unknown; *Acanthostega* had eight in the forelimb and *Tulerpeton* counted six digits both on fore- and hindlimbs [26]. It is unclear to this day, why the pentadactyl constraint was established and what factors and mechanisms prevent the appearance of polydactyly (more than five digits) phenotypes, even if multiple species, for example, pandas, moles, and turtles, attempted to 're-evolve' fingers [27–30]. Ancestral state reconstruction of the genus *Bachia* (belonging to a family of lizards) showed evidence that some species might have re-evolved digits after reducing from the five-digit state [31]. However the possibility of digit re-emergence in lizards and in other tetrapods is still debated [32–34].

Regardless of the exact scenarios of digit loss and re-emergence, all major anatomical changes throughout evolution arise from the modification of the developmental mechanism of the given feature. Indeed, developmental plasticity is key for the evolution of different traits [35]. Hence, it is logical to look for why a pentadactyl constraint was established in the development of the limb structures.

1.2 Tetrapod limb development

1.2.1 Limb initiation, outgrowth and digit patterning

The tetrapod limb emerges from a structure called the limb bud early in embryonic development. Although the position of the limb in the antero-posterior axis varies, especially in birds, the basic molecular mechanism of limb initiation is shared among tetrapods [36]. The induction of the limb starts with the interaction of retinoic acid (RA) signaling with beta-catenin and Hox gene signaling in order to induce the expression of the T-box transcription factors *TBX5* in the forelimb, or *TBX4* in the hind limb [37]. TBX5 in turn induces the expression of fibroblast growth factor 10 (FGF10) and together they initiate a program of epithelial-to-mesenchymal transition of the epithelial somatopleure as early as chicken stage 16 (51-56 hours of development) which becomes the limb bud mesenchyme [38](Figure 2A). FGF10 through WNT signaling induces the expression of *FGF8*, a crucial factor for the establishment of the apical ectodermal ridge (AER), a population of signaling cells driving the outgrowth of the limb [39]. FGFs diffusing from the AER maintains proliferation in the distal-most part of the limb bud providing the required cells for limb elongation [40, 41]. Implantation of *FGF10* expressing cells or FGF8 soaked beads into the flank of chicken embryos results in ectopic limb formation showing that both are sufficient to induce a limb bud and the outgrowth [40, 42].

While the AER is responsible for the expansion of the limb along the proximo-distal axis, the antero-posterior patterning is ensured by another organizing center called the zone of polarizing activity (ZPA). The existence of the ZPA was discovered when the posterior region of the chicken wing was implanted into the anterior margin and resulting in mirror-image duplication of the digits [43, 44]. RA and sonic hedgehog (SHH) signaling were identified as potential molecules responsible for the activity of the ZPA, as both are diffusible molecules, and RA or SHH soaked bead implantation into the anterior limb bud both reproduce the mirror-image duplication in chicken embryos [45, 46]. Later publications showed that the effect of RA-soaked bead implantation is indirect as it induces the expression of *SHH* by promoting *dHAND* expression and by repressing *GLI3* transcription in the anterior region [47].

In the autopod region, the antero-posterior patterning is crucial not only to determine the position and number of digits but also their identity (e.g. phalange number). The ZPA seems to coordinate the patterning of the more proximal bone structures via SHH and its functions in the patterning of autopod structures were suggested [48, 49]. Multiple mechanisms have been proposed to explain how SHH specifies digits. One is a French-flag, dose-dependent model, and another temporal-signal integration model [50–54]. The French-flag model argues that the concentration of the diffusing SHH is driving the arrangement of digits and the temporal integration suggests that the length of exposure also plays an important role in digit number and identity determination. Reduced duration of Shh expression in the limb seems to be a mechanism facilitating digit-loss in the Australian lizard genus *Hemiergis*, where closely related species are

ranging from pentadactyl to bidactyl. In bidactyl limbs, the *SHH* transcription is repressed earlier than in pentadactyl autopods, potentially leading to digit reduction [55]. In the pig and cow, possessing four and two toes respectively, the main receptor of SHH, PTCH1 is downregulated compared to five-digited autopods, leading to a decrease in the sensing of SHH. These examples together illustrate the different strategies that lead to digit loss via the regulation of the shh pathway [56, 57].

The limb-specific expression of *SHH* is controlled by a cis-regulatory element called ZPA regulatory sequence (ZRS) [58]. Due to this modular regulation, *SHH* transcription can be altered specifically in the limb bud without affecting the expression in other parts of the embryo, which leads to deleterious phenotypes [59]. This enhancer is located 1Mb upstream from the *SHH* gene in the intron of the *LMBR1* gene. Point mutations or longer deletions in the ZRS are cause of preaxial polydactyly in cats, dogs, the Silky chicken breed and also in human congenital disorders [58, 60–65]. Reporter gene analysis of these ZRS mutations showed either an extended region of expression of *SHH* in the posterior region or ectopic expression of Shh in the anterior margin of the limb bud, both resulting in preaxial polydactyly.

The molecular mechanisms underlying SHH signaling have been extensively studied [66]. The main effector in the context of digit patterning seems to be the transcription factor *GLI3*, as the phenotype of *GLI3* mutants and *GLI3* and SHH double mutants are identical [67, 68]. Without activation of the SHH pathway, GLI3 is a strong transcription repressor, however, upon activation of the SHH signaling, GLI3 acts as an activator of target gene expression [66, 69]. SHH is thought to relieve the repression of GLI3 in the distal portion of the limb in order to allow digit patterning [70]. Interestingly, limb specific GLI3 mutants (and *SHH, GLI3* double mutant) mice are heavily polydactylous in the forelimb as well as in the hindlimb [71]. This points toward the existence of a mechanism that patterns digits even in the absence of the SHH/GLI3 pathway. A Turing-type mechanism was put forward to explain this phenomenon, where a dynamic interaction between activator and inhibitor molecules determines a repetitive pattern of structures [72]. Namely, BMP, WNT and SOX9 – SOX9 is the earliest known chondrogenic marker – form a Turing-like system and the wavelength of patterning is controlled by HOXD11-13 and HOXA13 genes (Figure 2B) [73–76]. In this context, SHH and GLI3 are responsible for the proliferation of the presumptive digit area in the autopod plate, then the Turing-type mechanism involving Hox genes and BMP-WNT-SOX9 interaction determines the position and number of digits (Figure 2A) [77]. However, the role of SHH/GLI3 in determining digit identity (phalange number and length) is still important as in *GLI3* mutants the identity of anterior digits is lost and in *SHH/GLI3* double mutants both posterior and anterior digit identities are impaired [67, 68, 71, 77, 78].

Together, these studies demonstrate the plasticity of the skeletal patterning system in the autopod of vertebrates throughout development and suggest relative ease in changing digit numbers. The question thus arises: why are five digits seemingly the upper limit if genetically/molecularly it seems to be easy to become polydactyl? Skeletal elements

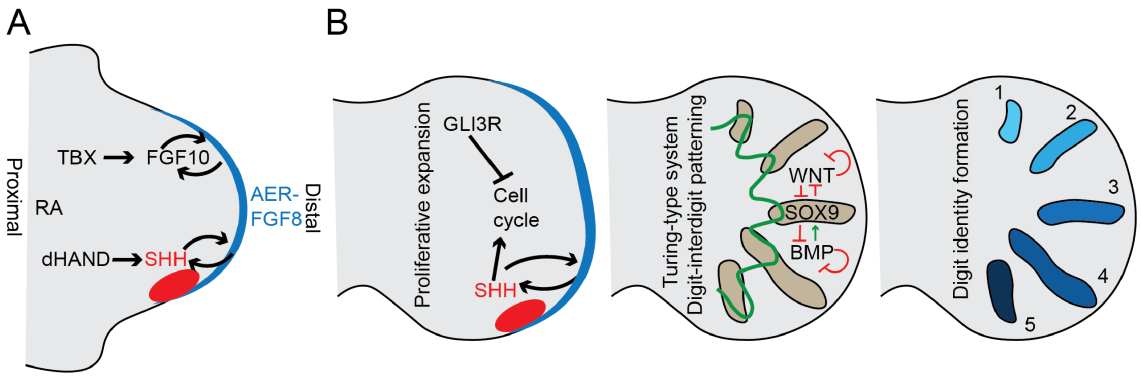

Figure 2: Schematic representation of the limb initiation and digit patterning (A) Simplified depiction of limb initiation processes and the molecules involved. Apical ectodermal ridge (AER) is represented in blue, Zone of polarizing activity (ZPA) in red, and limb mesenchyme in gray. (B) Concurrent mechanisms ensure digit condensation, digit positioning, and digit identity. Sonic hedgehog controls the expansion of the hand plate by acting on the proliferation. At the same time, BMP-SOX9-WNT Turing-type mechanism patterns digit and interdigit zones. Lastly, digit identity is determined by 5′ HoxD genes, potentially under the control of SHH signaling. Figure adapted from [77, 79]

are the support system of the limb, but they are not sufficient for creating a movable structure. The neuromuscular system has to follow the changes and should be considered when studying polydactyly.

1.2.2 Origin of muscle progenitors and muscle formation in the limb

Muscles are at the basis of all movement, as they generate force by contraction and set bones in motion. Unlike bones and connective tissue, limb muscles do not originate from the limb mesenchyme itself. Rather, they are derived from the somites, a repetitive structure specified from the paraxial mesoderm at either side of the neural tube [80]. Cells in the somite are organized into an epithelium at first, before going through an epithelial-to-mesenchymal transition and migrating away. The lateral half of the somite forms the dermomyotome, recognizable by the strong expression of Paired Box 3 transcription factor (PAX3), that gives rise to the limb muscle progenitors [81]. PAX7, another representative of the Pax-family, is also expressed in these progenitors and is required for the development of satellite cells, which are myogenic adult stem cells [82]. LBX1 is restricted to the migrating lineage of muscle progenitors and *LBX1* mutant mice show severe defects in limb muscle formation, especially in the dorsal limb [83, 84]. The main signal controlling the delamination of muscle progenitors from the dermomyotome is the HGF/c-MET pathway, where the receptor c-MET is present at the surface of muscle progenitor cells (Figure 3A) [85]. Further guidance in the limb is provided by SDF1/CXCR4 signaling (CXCR4 is expressed by progenitors), and EPHA4-EFNA5 interactions [86, 87].

Limb skeletal muscle progenitors first organize into dorsal and ventral pre-muscle masses and undergo massive proliferation under the influence of SHH signaling [89]. Muscle masses in the limb are pre-patterned by *TCF4*-expressing mesenchymal

fibroblasts and a population of embryonic fibro-adipogenic progenitors expressing *OSR1* (Figure 3B) [90–92]. The maturation and differentiation of muscle myoblasts involve exit from the cell cycle and fusion of myoblast into primary myotubes [93–95]. MYF5 and MYOD transcription factors are the master regulators of the myogenic cascade and double knock-out mice for these genes lack skeletal muscles, as no myoblasts or myotubes are formed [96–98]. Two waves of myotube formation have been observed during embryonic and fetal development: the first wave forms mostly slow-twitching muscle fibers and the second wave fast-twitching myofibers [99, 100]. *TCF4*-expressing fibroblasts and SHH signalling seem to play a role in slow-twitching myofibre formation [91, 101].

The connection between muscles and skeletal elements is essential for force transmission and movement [102]. The link between myotubes and bone is ensured by tendons that originate from limb mesenchymal connective tissue [103–105]. Tendons are composed of strong and dense connective tissue enriched in type I collagen and elastin [106]. The development of tendons and muscles appears to be independent of each other, however, the proper muscle belly formation and splitting of tendon primordia into individual tendons depend on the interaction between myotubes and tendons (Figure 3B) [107]. Tendon progenitor cells start expressing early on the gene scleraxis (*SXC*), a bHLH transcription factor. Loss-of-function of *SCX* only affects force-transmitting and intermuscular tendons, not the anchoring tendons, which suggests the involvement of other unknown molecules in the specification of different tendon types [108]. The expression of *FGF4* at the extremities of the forming muscle is known to facilitate the connection to the tendons and maintain the expression of *SXC* and another tendon gene

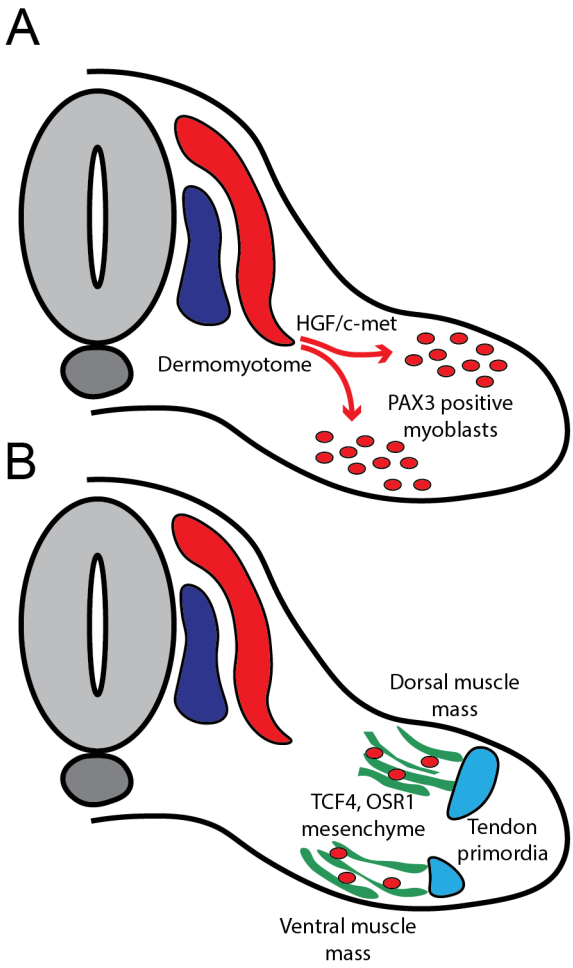

Figure 3: Schematic representation of early muscle progenitor migration and muscle formation (A) PAX3 positive muscle progenitors migrate from the dermomyotome into the limb under the effect of HGF present in the limb mesenchyme. (B) Muscle progenitors form dorsal and ventral muscle masses and are pre-patterned by TCF4 and OSR1 expressing mesenchymal cells. Figure adapted from [88]

tenascin (*TN*) in the tendon primordia [109]. Once the muscle-tendon connection is established, muscle fibers failing to connect with tendons are eliminated by RA-driven apoptosis, and well-delimited muscle bellies are formed [110].

For coordinated movement, a fine orchestration of muscle contraction is required, especially between dorsal extensor and ventral flexor muscle groups. This orchestration of muscle activity is ensured by the peripheral and central nervous systems which develop concomitantly to skeletal elements and muscles.

1.2.3 Limb innervating motor neuron specification and limb innervation

The nervous system is crucial for the perception of our environment, as well as for the control of our movements and locomotion. In vertebrates, the nervous system is composed of the central nervous system (CNS), including the brain and the spinal cord, originating from the ectoderm, and the peripheral nervous system connecting organs and limbs to the CNS. Neural induction takes place during gastrulation (before stage 4 in chicken) [111, 112]. In amniotes, Hensen's node was identified as the organiser of neural induction, similar to the Spemann-Mangold organiser in *Xenopus laevis* [113–115]. At the onset of neural induction, the border between neurectoderm and epidermal ectoderm starts to thicken and forms the neural folds while the neural plate bends to form the neural groove [116]. Later the two folds close up to form the neural tube which continues to close progressively from the caudal to the rostral end [117]. Where the two folds meet, the neural crest cells are specified and migrate away [118]. Neural crest cells are responsible for building the facial skeleton, teeth, pigment cells and parts of the peripheral nervous system, such as the dorsal root ganglia and Schwann-cells [119, 120].

Structurally, the neural tube is composed of a ventricular zone around the central canal, a mantle layer (also called the intermediate zone), and a marginal zone. The ventricular zone nests the stem cell niche while post-mitotic neurons migrate to the mantle zone to establish functional connections. Intriguingly, neural progenitors are spatially segregated into 11 different layers (laminae) along the dorso-ventral axis according to the function they later fulfill in the neural tube [122]. As an example, dorsal progenitors give rise to Laminae I-IV that later receive the sensory input of pain and touch, while motor neurons are born in the ventral layer [123, 124]. This distinctive layering is due to opposing morphogen gradients [122]. At the dorsal segment, the roof plate is expressing BMP and WNT that are essential for dorsal interneuron formation [125]. On the other side, the SHH-expressing notochord and the floor plate are critical for ventral neuron identity (Figure 4) [126–128]. The different concentrations and combinations of morphogens induce spatially delimited expression of transcription factors unique to each neural progenitor population (reviewed by [121]).

Motor neurons are derived from ventral progenitors, close to the ventral margin of the central canal, a layer called pMN. Their early unique molecular signature includes the homeodomain proteins PAX6, NKX6.1, bHLH factors OLIG1/2 and NRG2. The

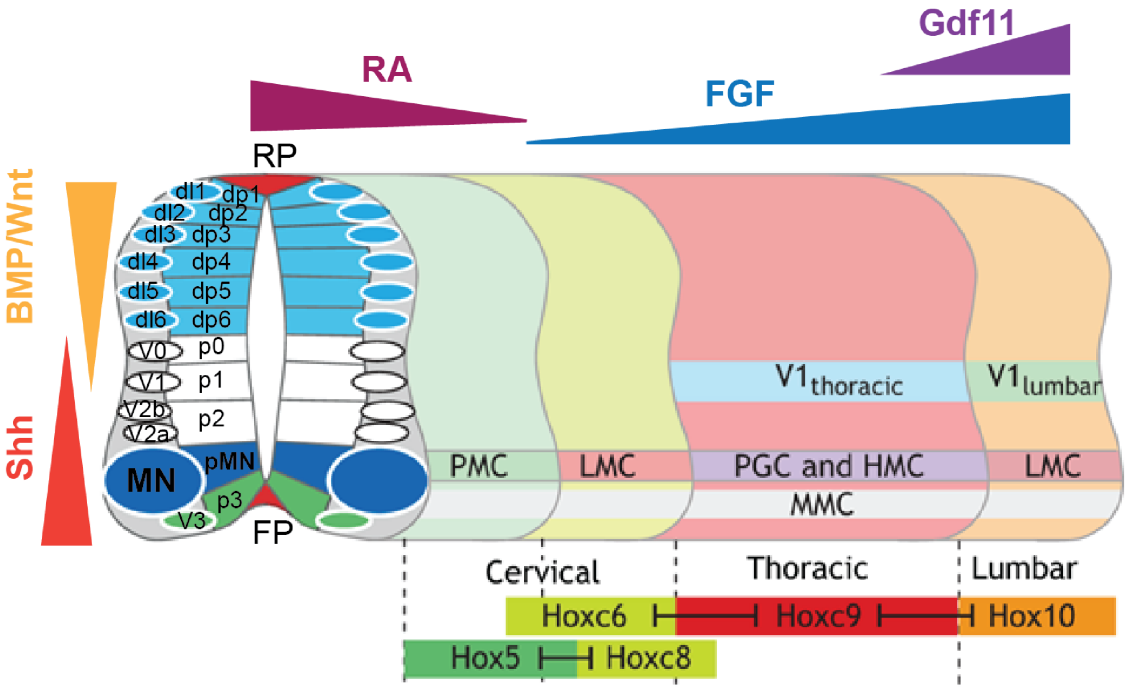

Figure 4: Recapitulation of the dorso-ventral and rostro-caudal patterning of the neural tube Opposing sonic hedgehog (SHH) and BMP/Wnt signaling to specify 11 different progenitor pools around the central canal of the spinal cord. Motor neurons are produced by the pMN at the ventral side and specified by high SHH levels. Post mitotic neurons are located in the mantle zone. Motor neurons are organized into columns along the rostro-caudal axis under the influence of rostral retinoic acid (RA) and FGF signaling. Hox genes are the main effectors in establishing the rostro-caudal organization, as they mutually exclude each other from segments. HOXC6 establishes the brachial LMC and the HOX10 gene expressing segment constitutes the lumbar LMC. Abbreviations: PMC: phrenic motor column, LMC: lateral motor column, MMC: median motor column, PGC: preganglionic motor column, HMC: hypaxial motor column. Figure adapted from [121].

specification of this group is highly dependent on SHH signalling, as in *SHH* mutant mice motor neurons (and other ventral populations) are absent [59, 129–132]. Interestingly, OLIG1/2 mutant mice not only lack the spinal motor neuron population, but also the oligodendrocyte lineage [133]. This phenomenon was explained by a switch from motoneuron production to oligodendrogenesis as the mutually exclusive *NKX2.2* expressing region starts to co-express *OLIG1/2* at later stages of development [134].

Post-mitotic motor neurons migrate away from the ventricular progenitor niche toward the ventral mantle zone. As motor neurons later extend projection toward target organs in the periphery, they organize around tightly regulated 'exit-points' where their axons can leave the central nervous system [135–138]. Motor neurons are recognisable by the expression of *MNX1* (also called *HB9*) and ISL LIM Homeobox 1 (*ISL1*) [139–141]. Limb innervating motor neurons are grouped in the lateral motor column (LMC) at the brachial and lumbar levels [139]. Their unique LMC identity is maintained by the Hox co-factor Forkhead Box P1 (FOXP1), and loss-of-function of *FOXP1* results in absence of LMC neurons [140]. The LMC is further sub-divided into medial (ISL1 positive) and lateral (LIM1/LHX1 positive) columns depending on whether the neurons innervate ventral or

dorsal limb muscles, respectively [142–144]. Interestingly, the motor neurons populating one or the other LMC columns are not generated at the same time. Medial LMC neurons are born first and they migrate to the ventral horn. The lateral LMC neurons migrate through the medial population in an "inside-out" manner [145, 146]. This migration is driven by Type-2 cadherins, as demonstrated by Price and colleagues [147]. Once limb innervating spinal motoneurons acquire a columnar fate, they are further divided into smaller groups, so-called motor neuron pools. Motor neuron pools are small subsets of LMC neurons destined to innervate a single specific muscle [148, 149]. They are spatially grouped together, potentially due to differential expression of cell adhesion molecules, and each motor neuron pool possesses a unique molecular signature. Some characteristics of the motor neuron pools are only refined upon contact with their target muscles, although their identity is specified early during neurogenesis [150].

Simultaneously to the dorso-ventral patterning described above, the neural tube is segmented into different parts along the rostro-caudal axis. The spinal cord is often divided anatomically into five distinct segments: cervical, brachial, thoracic, lumbar, and sacral. Similar to the dorso-ventral patterning, this is accomplished through opposing morphogen gradients, as well as the expression of *HOX* genes that mutually exclude each other from different segments. The HOX activator signals are RA (rostral), FGF and GDF11 (caudal) originating from paraxial mesoderm and Hensen's node (Figure 4) [151, 152]. *HOX5* genes limit the cervical spinal cord, *HOX6* and *HOX9* the brachial and thoracic regions, respectively, while *HOX10* is specifying the lumbar segment (Figure 4) [153–155]. LMC fate in the brachial spinal cord, innervating forelimb muscles, is mostly dependent on *HOXC6* and *HOXC8* expression, induced by RA signalling and inhibited by caudal *FGF* signalling [153, 156]. Interestingly, the boundary between brachial *HOXC8* and thoracic *HOXC9* seems to group digit innervating motor neuron pools together [157]. Similarly, the lumbar LMC is specified by the *HOXA10* and *HOXD10* genes and lumbar motor neurons innervate the hindlimbs (Figure 4) [154, 158–160].

Together, these intricate cross-regulations of multiple morphogens along the antero-posterior and dorso-ventral axis, and interactions of transcriptional regulators result in correct maturation and positioning of nerves in the spinal cord and eventually ensure proper innervation of various structures.

Neurons project long protrusions, so-called axons, across considerable distances toward target structures from the central nervous system to the periphery. They have to navigate various environments and integrate positional information relayed by signalling pathways along their trajectory [161–163]. Axons sense their environment via the growth cone, a dynamic actin-rich, motile region at the tip of the axon [164]. Different receptors are present on the growth cone that directly affect the actin-structure, and hence repulsing or attracting the axon [161, 165–167]. Axon guidance molecules can be long-range/diffusible (such as Netrins and class 3 Semaphorins) or short-range, requiring cell-cell contact (as Eph-Ephrin couples) [168–172]. In the spinal cord, commissural neuron projections are often used as a model to understand mechanisms

of axon guidance. Commissural neuron axons cross from the dorsal horn of the neural tube to the contralateral side through the floor plate and relay nociceptive, proprioceptive information and also control motor output [173–179].

In the case of limb innervating motor neurons, once the LMC is positioned, axons are projected through the 'exit-points' of the ventral horn toward the periphery. The brachial LMC expands approximately from the mid-cervical segment (C4) to the first thoracic vertebra (T1) in mouse [157]. Projecting axons are organized into narrow plexus – alongside sensory neurons from the dorsal root ganglia - at the basis of the limb and reorganize during a "waiting period" of around 24 hours [180]. At first, outgrowing nerves face a dorso-ventral "choice-point" as an intricate attraction-repulsion interaction guides them to the correct limb compartment. EPHA4 expressing lateral LMC axons are attracted by the ephrin-B (EFNB) ligands present in the dorsal mesenchyme while repulsed by EFNA ligands of the ventral region. Conversely, medial LMC axons express EPHB1, and are attracted to the ventral EFNA ligands and repulsed by dorsal EFNB as they invade ventral compartment Figure 5A) [143, 146, 181].

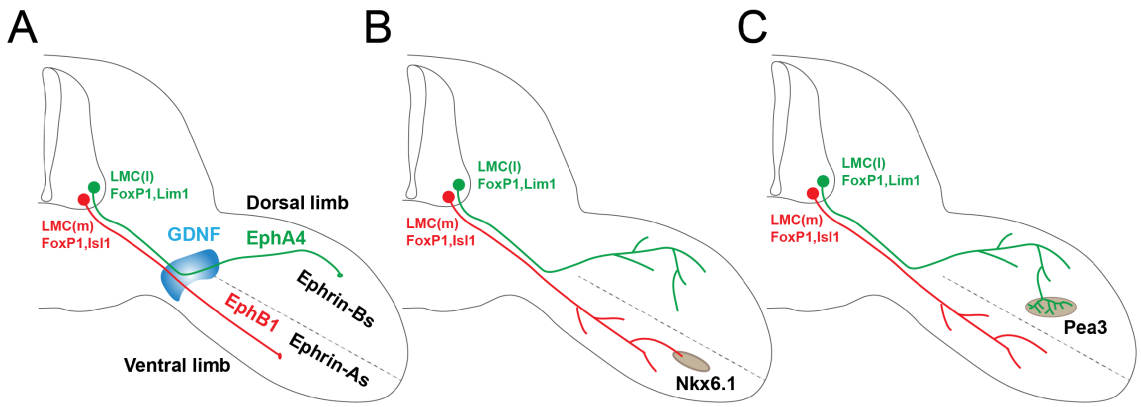

Figure 5: Axon guidance in the limb (A) LMC neuron projections are confronted with a dorso-ventral 'choice point' at the basis of the limb (GDNF). Lateral LMC (LMC(l)) neurons express REt and EPHA4, hence they are directed through the GDNF expressing tissue and attracted to the dorsal Ephrin-B positive mesenchyme. Medial LMC (LMC(m)) neurons are expressing EPHB1 and guided into the Ephrin-A expressing ventral mesenchyme. (B) Motor neurons are guided to their specific target muscles by primary (also called intermediate) motor neuron pool-specific genes, such as NKX6.1. (C) Target-derived factors activate end-plate arborization, and induce late motor neuron pool genes, such as Pea3, in the spinal cord.

After the dorso-ventral choice-point, nerves are further penetrating the limb and follow different paths in order to connect to the appropriate muscle. Limb innervating neurons have long axon projections, and autopod innervating nerves especially have to make a long route. The information about nerve trajectory seems to be relayed in two phases: primary information is encoded by the columnar HOX and LIM/ISL factors and early motor neuron pool transcription factors, such as RUNX1, SCIP, or NKX6.1, and the activated target genes drive the axons toward appropriate targets (Figure 5B) [139, 144, 182–184]. Then, upon contact with a muscle, target-derived factors such as neurotrophic factors not only promote motor neuron survival, but also refine motor neuron pool

identity by the expression of e.g. ETS factors (such as *PEA3* and *ER81*) or POU-factors (as *POU3F1*) (Figure 5C) [157, 185–191].

The contact between muscles and motor neurons is established via the neuromuscular junction (NMJ) [192, 193]. They represent synaptic sites where nerves transmit action potential to the muscle fiber that leads to muscle contraction. Muscles and nerves communicate by neurotransmitters released into the synaptic cleft [194, 195]. Motor neurons release acetylcholine (ACh) as a neurotransmitter and motoneurons are recognized by their expression of genes involved in the production of ACh (such as Choline Acetyltransferase (CHAT)), or in its transport toward the synaptic cleft (Vesicular acetylcholine transporter (VAChT)) [196, 197].

In order to keep muscle activity under control, or activate contraction when needed, proprioceptive sensory neurons also connect to intrafusal muscles [198]. These bipolar proprioceptive neurons are located in the dorsal root ganglion (DRG), a repetitive structure on either side of the neural tube, and the sensory neurons extend one projection toward the target muscles, and another into the spinal cord [199]. Upon entry into the spinal cord via the dorsal horn, sensory neurons relay information either mono-synaptically directly to the cell bodies of motor neurons, or di-synaptically via inhibitory interneurons, thus regulating motor output [187, 198, 200]. Motor neurons, muscles, and proprioceptive sensory neurons thus form the so-called spinal motor circuit and ensure a well-orchestrated and controlled movement of limb muscles.

Previous work thus suggests that motor neurons have a piece of predetermined pathfinding machinery in place when they enter the limb bud. Later their molecular identity gets refined by neuron-muscle crosstalk during the establishment of the NMJ. The potential plasticity of this elaborated system, and how it could adapt to a polydactylous environment, however, has not yet been investigated.

1.3 Aims of the thesis

The correct assembly of the neuromuscular system, and the skeletal apparatus it connects to, is at the origin of all movement, including diverse locomotor output such as walking, flying, and swimming. Strict spatiotemporal coordination is required for the correct assembly of the limb skeletal apparatus, and its integration with the neuromuscular system.

The previous sections of the introduction highlight the complexity of the assembly of the limb neuro-musculo-skeletal system. As shown in section 1.2.1, we have a fairly good understanding of how pentadactyly is maintained at the skeletal level by Shh/Gli3 and Hox genes, how digit loss can occur and how extra digits arise and are patterned in polydactyly. Conversely, very little is known about how the neuromuscular system can respond to polydactylies. In this work, using the chicken polydactyl model, I intend to

- evaluate the plasticity of the musculature and the peripheral nervous system in response to polydactyly. To this aim, we generate polydactylous chicken embryos and use wholemount immunostaining and light sheet microscopy to reconstruct, in 4 dimensions, the development of the musculature and nerve projections in control and polydactyl wing and leg autopods.
- assess the plasticity of the central nervous system in regards to motor neuron number and cell-type diversity in polydactyl and control spinal cords. To this aim, we use single-cell RNA-sequencing, for the first time in the chicken model, and present a map of the chicken spinal cord at a mid-gestation stage (HH36, day 10).
- gain insight into motor neuron pool molecular identity changes connected to 'native' and ectopic extra-muscles in polydactylous limbs. I developed a technique to trace back motor neuron pools from a single specific embryonic muscle (retrograde axonal labeling) and harvest individual labeled cells for single-cell RNA-sequencing (Smart-seq2). Then, we are able to compare the gene expression patterns of different motor neuron pools and learn how they differ from each other.

Together these results bring a better understanding of how the neuromuscular system, including the central and peripheral nervous system and musculature, respond to the presence of extra-digits.

Chapter 2

Development of the chick wing and leg neuromuscular systems and their plasticity in response to changes in digit numbers

2.1 Abstract

The tetrapod limb has long served as a paradigm to study vertebrate pattern formation. During limb morphogenesis, a number of distinct tissue types are patterned and subsequently must be integrated to form coherent functional units. For example, the musculoskeletal apparatus of the limb requires the coordinated development of the skeletal elements, connective tissues, muscles and nerves. Here, using light-sheet microscopy and 3D-reconstructions, we concomitantly follow the developmental emergence of nerve and muscle patterns in chicken wings and legs, two appendages with highly specialized locomotor outputs. Despite a comparable flexor/extensor-arrangement of their embryonic muscles, wings and legs show a rotated innervation pattern for their three main motor nerve branches. To test the functional implications of these distinct neuromuscular topologies, we challenge their ability to adapt and connect to an experimentally altered skeletal pattern in the distal limb, the autopod. Our results show that, unlike autopod muscle groups, motor nerves are unable to fully adjust to a changed peripheral organisation, potentially constrained by their original projection routes. As the autopod has undergone substantial morphological diversifications over the course of tetrapod evolution, our results have implications for the coordinated modification of the distal limb musculoskeletal apparatus, as well as for our understanding of the varying degrees of motor functionality associated with human hand and foot malformations.[1]

[1] Article published in Developmental Biology, see also A https://doi.org/10.1016/j.ydbio.2019.10.035;

2.2 Introduction

During vertebrate limb development, growth and patterning need to be precisely orchestrated in both space and time.Genetic analyses and experimental embryology studies have revealed the existence of multiple cross-regulatory signaling systems that confer developmental stability, while at the same time leave room for evolutionary modifications to occur therein [69, 201, 202]. This task, however, is complicated by functional units inside the limb that consist of multiple tissue types, some of which originate from different embryonic precursor pools. For example, skeletal cells of the limb musculoskeletal apparatus originate from lateral plate mesoderm precursors [203]. Somite-derived muscle cells migrate into the limb bud, form distinct muscle groups and attach to the developing skeletal elements via tendons [104, 107, 204–206]. Motor neurons residing in the spinal cord, and sensory neurons in the dorsal root ganglia, project their axons into the limb periphery to connect to these muscles in a highly stereotypical manner [150, 207, 208].Hence, embryonic patterning of these three tissues needs to be tightly coordinated, to successfully integrate skeletal, muscular and neural anatomy, and produce a fully operational limb. Likewise, evolutionary modifications in the pattern of any one of these tissues necessitate parallel alterations in the morphology of the others.
Over the course of vertebrate evolution, the skeleton of tetrapod limbs has greatly diversified, reflecting adaptations to a variety of different styles of locomotion. In the proximal parts of the limb the number of skeletal elements is largely conserved, with evolutionary modifications occurring predominantly through changes in length and girth of the respective bones [209]. Such alterations can be apparent even within a single species, due to different locomotor behaviours associated with the respective fore- and hindlimbs [210–212]. The most striking differences, however, have appeared in the skeleton of the autopod, with changes occurring in both digit patterns and numbers [213, 214]. Based on seminal work in traditional model organisms, we now have the ability to elucidate these evolutionary autopod diversifications at the molecular level [79, 202]. For example, variations in Sonic Hedgehog signalling pathway activity have been demonstrated to affect digit numbers in a wide range of tetrapod species [55–57, 62]. The resulting morphological changes in the autopod, however, have so far mainly been studied at the skeletal level, while muscle and nerve modifications in experimentally altered limbs have only been described at more proximal levels [101, 215].
Here, capitalizing on the power of whole-mount immunohistochemistry and light-sheet fluorescent microscopy (LSFM), we present a 3D-atlas of the developing neuromuscular system in distal chicken limbs. While early muscle patterning occurs in a largely uniform dorso-ventral manner, we find a relative rotation of the main motor nerves between wings and legs.While early muscle patterning occurs in a largely uniform dorso-ventral manner, we find a relative rotation of the main motor nerves between wings and legs. By experimentally altering the skeletal formula of the autopod, we challenge the developmental plasticity of these two distinct neuromuscular architectures to adapt to changes in dactyly. Intriguingly, we find that while the musculature

closely follows changes in skeletal topology, wing and leg innervation patterns are only partially responsive. This apparent discrepancy in patterning flexibility, between the muscular and nervous systems, has implications for the evolutionary diversification of the vertebrate autopod, as well as for the different congenital malformations affecting human hands and feet.

2.3 Results and discussion

2.3.1 3D-analysis of neuromuscular development in chicken limbs

In order to monitor the coordinated patterning of nerves and muscle groups, we first produced a 3D-atlas of the developing neuromuscular system in chicken fore- and hindlimbs. Through whole-mount double-immunohistochemistry against neuron-specific intermediate filament protein (neurofilament, *NF200*) and muscle-specific myosin heavy chain (MHC, *MF20*), we visualized the appearance of limb nerves and muscle groups, respectively. Following CUBIC clearing, LSFM image acquisition and 3D-reconstruction, segmentation -based tracing was used to delineate and pseudo-colour major nerves and muscle bundles (Fig. 1A,B; Fig. S1A,B; Fig. S2A,B) [216, 217].
At day 5 of development in the wing, growing axons are invading the bud and form two main fascicles, one dorsal (n. brachialis superior) and one ventral (n. brachialis inferior) (data not shown). Around day 6, further subdivisions become evident, giving rise to the three major nerve branches of the limb that contain the projecting axons of motor and sensory neurons: the radial nerve (cyan) on the dorsal side; the median (yellow) and ulnar nerve (magenta) on the ventral side. From there, the branches split further to innervate in a stereotypical and non-overlapping manner the musculature of the forming digit territories, which become visible at later time-points (day 7 to day 10) (Fig. 1C, Fig. S1C,E). Three main nerve branches also connect to the leg musculature. Dorsally, two arched nerves, the median (green) and lateral (orange) fibulars, share a common peroneal origin (Fig. S2C). On the ventral side, innervation of the foot is provided by the plantar nerve (Fig. S2E, purple).

In parallel to limb innervation, muscle precursors aggregate and differentiate into dorsal and ventral muscles masses, soon after their migration from the dermomyotome (data not shown)[218, 219].These two masses then split along the antero-posterior (A/P) and proximo-distal (Prox./Dist.) axes to form the individual muscles of the wing and the leg (Fig. 1D; Fig. S1D,F; Fig. S2D,F). At day 6, the hand/foot muscles masses are still continuous with the forearm/shank that has started to cleave along its A/P axis. From day 7 onwards this connection is progressively lost, with a spatial detachment of the forearm/shank and hand/foot muscles masses at the intermediate tendon primordia levels [107]. Starting around the same stage, discrete hand and foot muscles separate anteriorly-posteriorly from their primary muscle masses. Those

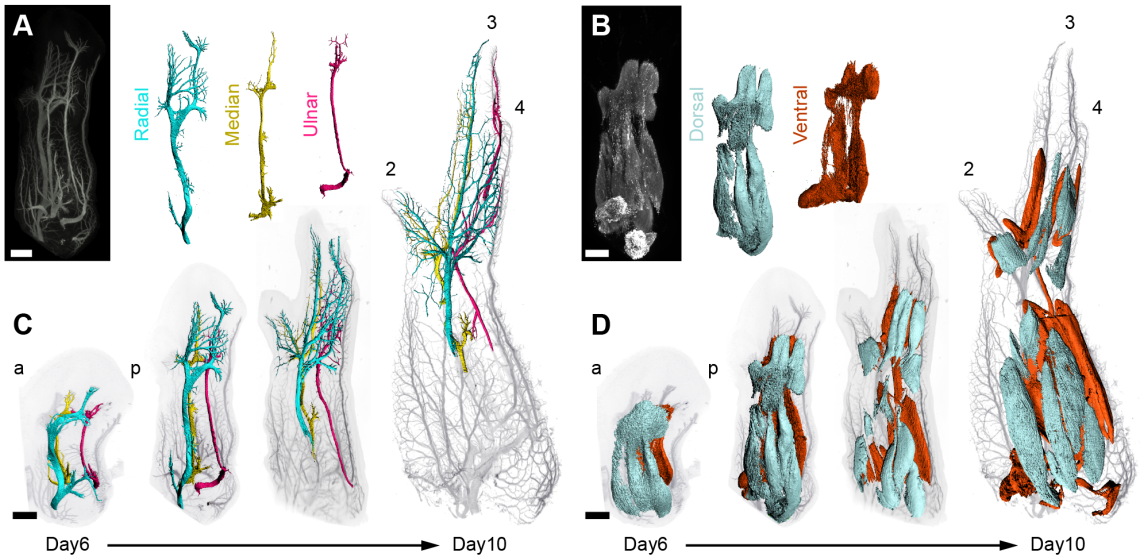

Figure 1: 3D-analysis of the developing neuromuscular system in the chicken forelimb (A, B) Image acquisition and analysis workflow used to identify nerves innervating the autopod and its corresponding muscle masses. Nerves and muscles were visualized with antibodies against neurofilament (NF200) and myosin heavy chains (MF20) and imaged with a light sheet microscope. After 3D reconstruction of the embryonic wings, surfaces were rendered using segmentation-based tracing to highlight structures of interest. The radial nerve (cyan) innervates the dorsal muscle mass (light blue), while the median nerve (yellow) anteriorly and the ulnar nerve (magenta) posteriorly connect to the ventral muscle mass (red). (C,D) Dorsal view of the neuromuscular development in the wing between day 6 and day 10 of development. In this time window, motor and sensory axons invade the developing wing and simultaneously muscle bellies segregate from dorsal and ventral muscle masses. The radial nerve innervates all three digits in the dorsal part whereas ventrally, the median arborizes into digit 1 and digit 2 and the ulnar in digit 2 and 3. A/P, anterior/posterior, Prox./Dist., proximal/distal. After day 7, limbs were cropped at zeugopod levels, to allow visualization of the intermediate tendon primordia location (forearm-hand junction). Scale bars represent approx. 500µm.

muscles become increasingly individualized, elongate and adopt their eventual fusiform shape from day 8 to day 10. As such, they give rise to a precise muscular topology, with eleven main muscles in the wing autopod and seven in the foot (Fig. S3A-D). At similar developmental stages both muscle individualization and peripheral nerve branching appear more advanced in the hindlimb than in the forelimb. These observations support the notion that a developmental heterochrony may exist between embryonic chicken limbs, with the development of legs being slightly more advanced then in wings [220]. Collectively, we present a comprehensive 3D-atlas of the developing neuromuscular system in chicken wings and legs at high spatial and temporal resolution.

2.3.2 Differential innervation patterns between the wing and the leg

Although both fore- and hindlimbs contain three major nerves-comprising motor axons, their A/P and D/V (dorso-ventral) layouts show striking differences. Namely, while a single nerve (radial, cyan) occupies the anterior-dorsal quadrant of the wing cross-section, this arrangement is inverted for the plantar nerve (purple) in the posterior-ventral sector of the leg (Fig. 2A,B). The median-ulnar (yellow, magenta) and

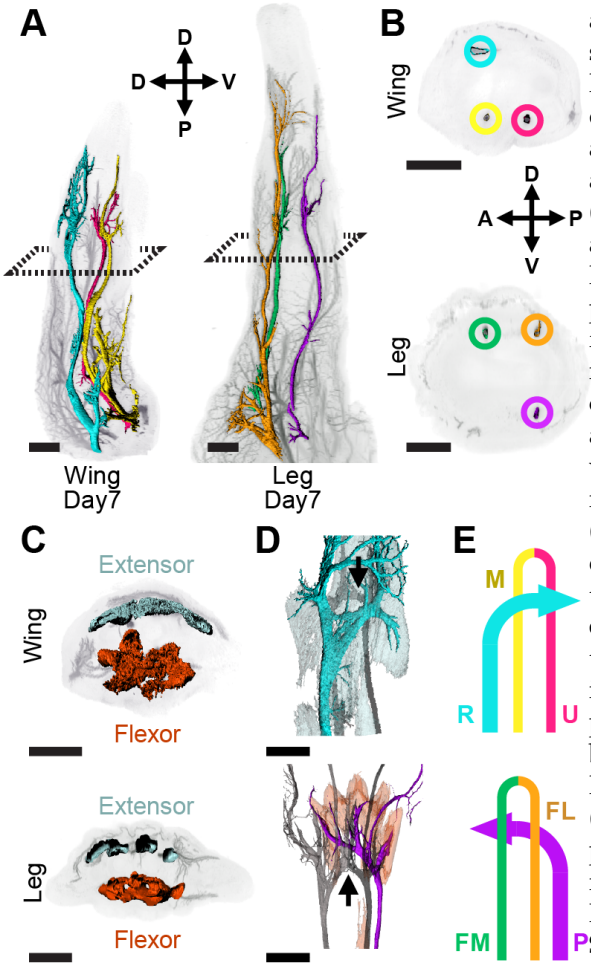

Figure 2: Differential innervation patterns in chicken wings and legs (A,B) Side views (A) and virtual cross sections (B) of the nervous systems at the indicated levels (A, dashed lines) of a 3D-reconstructed wing and leg at day 7 of development. Three main motor axon-containing nerves project into both wing and leg. In the wing, we find one dorsal-anterior (Radial, cyan) and two ventral nerves (Median and Ulnar, yellow and magenta). In the leg, one nerve (Plantar, purple) can be found posterior-ventrally, while two nerves (Median fibular and Lateral fibular, green and orange) innervate the dorsal musculature. (C) Virtual cross sections of the muscle masses at the autopod level at day 7 of development. In both wing and leg, dorsal and ventral masses give rise to extensor and flexor muscles, respectively. (D,E) Dorsal views (D) and schematics (E) of wing and leg innervation patterns. In the wing, the dorsal radial nerve reaches all extensor muscles by projecting from anterior to posterior, while the ventral plantar nerve innervates flexor muscles by turning from posterior to anterior in the leg. The paired nerve branches, ventral in the wing and dorsal in the leg, fuse distally to from an arched structure (D, arrow). D/V, dorsal/ventral, Prox./Dist., proximal/distal; A/P, anterior/posterior. R, radial nerve; M, median nerve; U, ulnar nerve; FM, medial fibular; FL, lateral fibular; P, plantar. Scale bars represent approx. 500µm.

median fibular-lateral fibular (green, orange) nerve pairs reside in the ventral and dorsal halves of the wing and leg, respectively. These distinct nerve arrangements are unlikely to result from the different rotations of the adult limbs, relative to the main body axis, as at the time of nerve invasion the orientations of fore- and hindlimbs are identical.

Accordingly, dorsal wing and leg extensor muscles are predominantly innervated by either single (wing) or double (leg) nerve branches, with the ventrally located flexors displaying the opposite configuration (Fig. 2C). In addition to differences in nerve branch arrangements along the A/P and D/V axes, the single nerves in the wing and the leg also display distinct A/P projection routes. While the radial nerve follows a distal curvature reaching from the anterior to the posterior side of the dorsal wing, the ventral plantar nerve takes an opposite trajectory, posterior to anterior in the foot (Fig. 2D,E). Moreover, both paired nerves, median-ulnar ventrally in the wing and median fibular-lateral fibular dorsally in the leg, fuse and produce an arched structure whose location coincides with the proximal onset of the respective autopod muscle groups (Fig. 2D,E; arrows). Hence, these results illustrate an inverted configuration for the basic innervation patterns of the chicken wing and the leg (Fig. 2B, Movie 3). Such an inverted arrangement of the major nerve branches in wings and legs also suggest a differential pre-disposition in their ability

to respond and adapt to changes in skeleton and/or muscle anatomy.

2.3.3 Innervation plasticity in polydactyl wings and legs

Limb innervation patterns develop in highly stereotypical fashion. Their ability to adapt to skeletal changes has been previously evaluated at proximal limb levels [215, 221]. Based on these pioneering studies, we decided to re-visit this apparent plasticity of limb nervous system. We capitalized on the superior resolution offered by LSFM, and decided to focus on the distal limb, the autopod, i.e. the site of major evolutionary alterations and fine motor skills control. In order to challenge the system with extra digits, we took advantage of the chick limb model using a well-established model of vertebrate polydactyly. At day 3 of development, we implanted retinoic acid-soaked beads at the anterior margin of the developing limb. This experimental manipulation is known to lead to mirror-image duplications in limb skeletal patterns, via the ectopic induction of Shh expression anteriorly (Fig. S4) [45, 47, 222]. For autopods showing complete (wing) or partial (leg) mirror duplication, the effects on axonal pathfinding and muscle patterning were evaluated using the same staining and imaging procedures as described above.

Three days after bead implantation in the wing (day 6), both radial and median nerves seem affected and show important defasciculations at anterior-distal levels (Fig. 3A,B, arrow). The ulnar nerve, however, remains unchanged (Fig. 3B). At later stages (day 7 to day 9), we observe a complete bifurcation of the radial and median nerves, which now have invaded the polydactyl territory (Fig. 3B,C asterisks; Fig. S5A,B). At hindlimb levels, the first signs of nerves branching toward the extra digit territory also appear three days after bead implantation. The posteriorly located lateral fibular nerve is not affected, reminiscent of the fate of the ulnar nerve in the polydactyl wing (Fig. 3D-F). The anterior median fibular nerve branch, however, defasciculates and invades the anterior duplicated side, similar to the wing median nerve. Additionally, it forms an arched structure onto itself (Fig. 3E,F, arrowheads; Fig. S5C,D). In the ventral side of the polydactyl foot, the plantar nerve extends slightly further into the anterior part, with a more pronounced distal-to-proximal curvature than in controls (Fig. S5C,D), yet it does not split in response to the anterior addition of extra digits. Surprisingly, however, an ectopic projection from the lumbosacral plexus invades the anterior margin of the hindlimb field. At later stages, the plantar nerve and the ectopic projection meet distally and form an arch from which additional branches project to the duplicated digits, in a pattern similar to control limbs (Fig. 3E,F, arrow; Fig. S5C,D).

To assess the neuronal nature of these ectopic projections in polydactyl wings and legs, we performed immunohistochemistry to discriminate motor from sensory nerves. We employed a triple labeling approach, using a pan-neuronal (beta-tubulin, *'Tuj1'*) and a sensory neuron marker (transient adhesion glycoprotein-1, *'Tag-1'*), together with a muscle-specific staining (fast Myosin Heavy-Chain, *'MyHC'*) [217, 223, 224].This combination allowed us to distinguish motor and sensory neurons, as the projections of the former stained strongly for *'Tuj1'*, but were largely devoid of *'Tag-1'*, when exiting

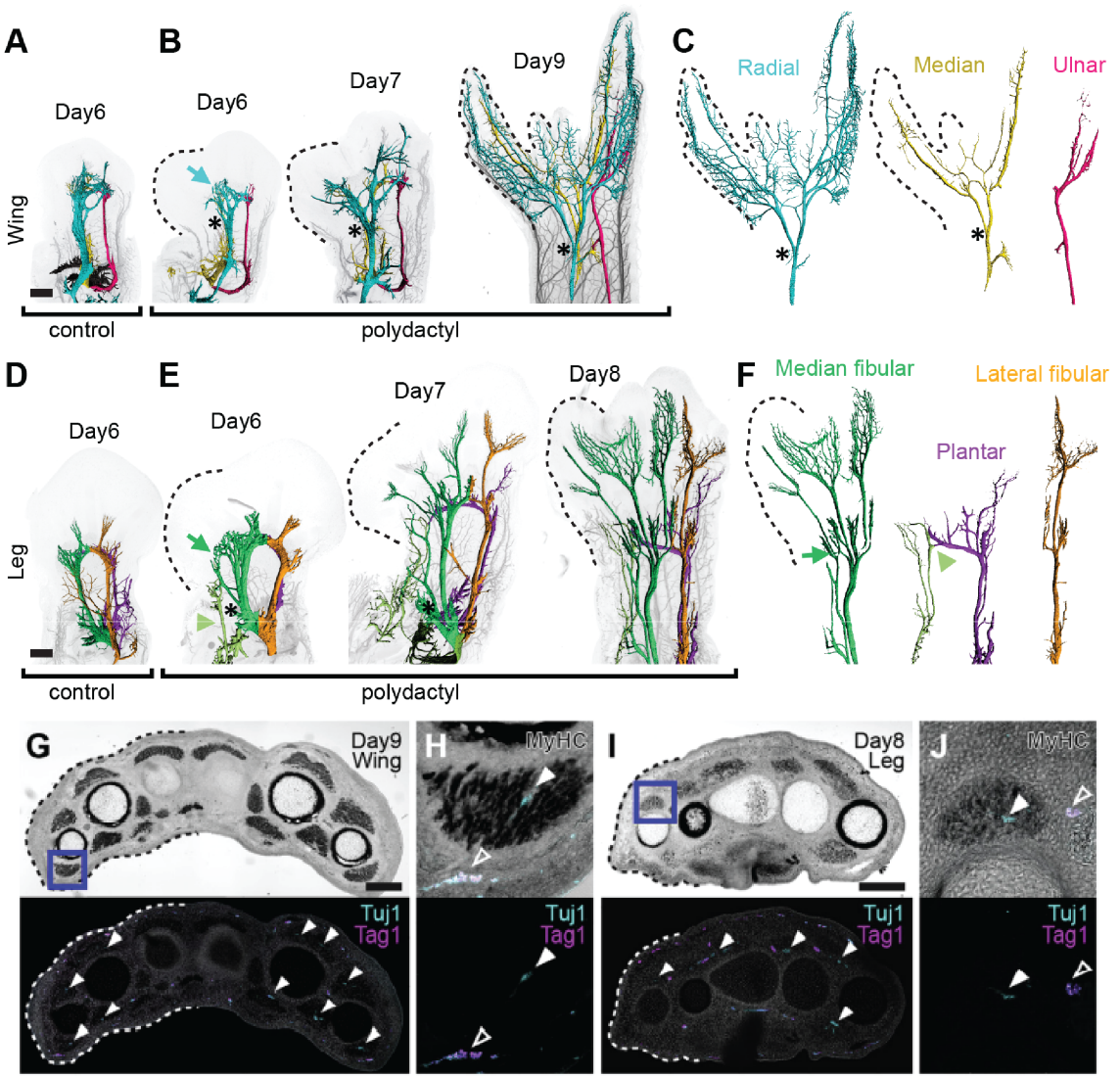

Figure 3: Modified motor and sensory innervation patterns in polydactyl wings and legs (A-C) Dorsal view of developmental progression of innervation patterns in control (A) and polydactyl wings (B). An arrow highlights the early defasciculation of the radial nerve (B), with the median following approximately one day later. Asterisks mark the ectopic bifurcation points of the respective nerves. The overall pattern of the ulnar nerve does not seem to be affected by the polydactyly (B,C). Both radial and median nerves bifurcate and innervate the duplicated digit territories (C, dotted lines). (D-F) Dorsal view of developmental progression of innervation patterns in control (D) and polydactyl legs (E). The median fibular nerve defasciculates to innervate the dorsal half of the extra digit, and forms a persistent arched structured with itself (E,F; arrows). In the ventral portion of the leg, an ectopic projection (E,F, lightgreen) emerges and fuses with the plantar nerve into an additional arch (F, arrowhead). The lateral fibular nerve does not respond to the presence of an extra digit. (G-J) Innervation of extra digit territories by both motor and sensory neurons in polydactyl wings (G,H) and legs (I,J). Motor axon projections inside muscle bundles stain for Tuj1 only (G-J, arrowheads), whereas as sensory nerves are Tuj1/ Tag-1 double-positive (H,J, empty arrowheads). Blue box in (G,I) corresponds to magnified view in (H,I) for FDQ′ and da respectively.. All images anterior to the left. Scale bars represent approx. 500µm in A-F, 250µm in G,I.

the lateral motor column (LMC) of the spinal cord (Fig. S6A). At proximal levels, in both native and duplicated autopod sides, we found evidence of innervation by motor as well as sensory axons (Fig. 3G-J). Importantly, nerves inside of muscles bundles stained

predominantly with *'Tuj1'* only, indicating that they were made of motor axons coming from the LMC (Fig. 3G-J, arrowheads). At more distal levels, i.e. beyond the autopod musculature, as well as inside the skin, only *'Tuj1'*/ *'Tag-1'* double-positive sensory nerves were detected (Fig. S6A,B).

Hence, in polydactyl fore- and hindlimbs, supernumerary digits are innervated by both motor and sensory neurons, along ventral and dorsal routes, through defasciculation and eventual nerve bifurcations at the level of the developing mesopod. This suggests the presence of an additional A/P "choice point" in the limb periphery, to ensure digit-specific innervation patterns [208]. Moreover, the response to such putative guidance signals seems plastic and can be modulated by the presence of additional digit territories. However, only two of the three major nerves seem responsive to project to the extra digits. Therefore, and in contrast to the symmetric addition of skeletal elements in polydactyl wings, the corresponding innervation patterns do not represent a full mirror-image duplication [70].

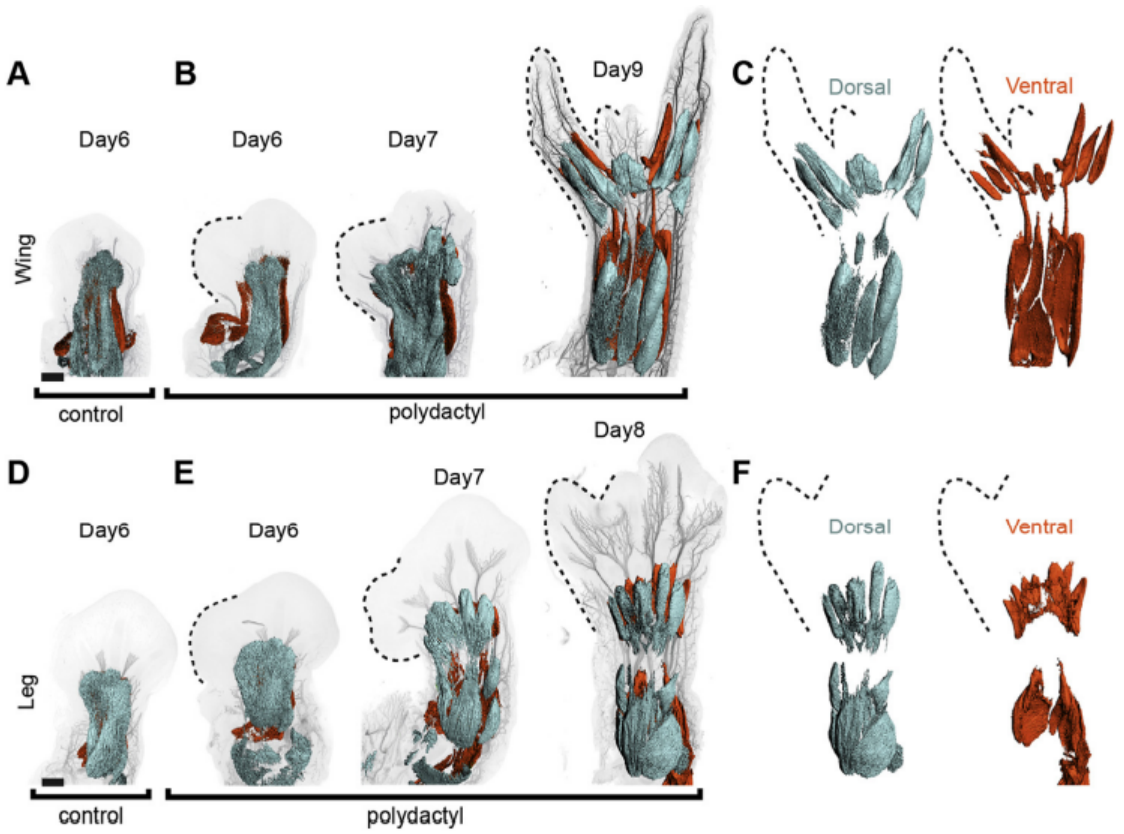

Figure 4: Modified muscle development in wing and leg polydactylies (A-F) Dorsal view of muscle development in control and polydactyl wings (A-C) and legs (D-F). At day 6, distal muscle masses are expanded along the anterior-posterior axis, and start to split at around day 7 (B). At day 9, wing dorsal (extensor, blue) and ventral (flexor, red) muscles are completely split and individualized into a complete mirror-duplicate pattern and connect to all digits in both native and duplicated halves of the autopod (dotted lines, C). Likewise, similar dynamics lead to all native and extra digits in the foot being matched by dorsal (extensor, blue) and ventral (flexor, red) muscle groups (dotted lines, F). All images anterior to the left, distal on top. Scale bars represent approx. 500µm.

2.3.4 Differential response of muscle and nerve patterns to a polydactyl autopod environment

We next analyzed the resulting changes in muscle patterns in polydactyl fore- and hindlimbs. Since alterations in the forearm musculature have been previously reported, we again focused our attention on the impact of wing and leg digit duplications on the respective autopod muscle groups [101]. In both situations, three days after bead implantation, the extensor and flexor masses appear expanded and the muscles fibers re-orient themselves towards the native and duplicated digit territories. At later stages (day 7 to day 8-9), we first observed the appearance of partial, supernumerary splits in the expanded muscles masses. These splits eventually resolve into completely individualized extra muscle bundles, regardless of whether a true mirror-duplication of the skeletal structure (wing) or the addition of a single anterior digit (leg) occur (Fig. 4A-F).

In case of the duplicated wing, the morphology of these additional muscles allows for the identification of their homeotic identities, which closely follow the underlying skeletal topology (Fig. 5A,B). As a result, duplicated posterior-ventral muscles seem now ectopically contacted by the anterior split branch of the median nerve, instead of the ulnar, thus having altered their connectivity to the spinal cord compared to their native, control-side counterparts (e.g. FDQ', Fig. 5B; Fig. 3C,H). For the leg, the partial duplication of the autopod skeleton complicates a clear muscle identity assignment. As for the wing, however, a pair of ectopic muscles appears – one dorsal, one ventral to the anterior extra digit (Fig. 5C,D). Hence, unlike for the nervous system, all extra digits in wings and legs are matched with corresponding, additional muscle bundles, thereby perfectly complementing the skeletal alterations at the level of the musculature.

To follow the temporal dynamics of these extensive reorganizations, and estimate the potential variability associated with, we assessed muscle and nerve alterations along our experimental time lines. We followed muscle changes at the level of splitting and individualization, whereas nerves were scored for defasciculations, bifurcations and potential ectopic fusions. Plotting these results along spatiotemporal axes revealed a posterior-to-anterior sequence of muscle maturation in the wing, which is recapitulated on the mirror-duplicated side (Fig. 5E). A similar trend can be observed for the leg musculature, and both duplicated sides in wings and legs show a slight developmental delay compared to their native counterparts (Fig. 5E,F). At the innervation level, the first visible signs of nerve re-arrangements appear roughly a day earlier than for the musculature, and the two most posterior branches, the ulnar (wing) and the lateral fibular (leg), remain unaffected throughout development (Fig. 5G,H). Thus, as for the final pattern alterations, the underlying temporal dynamics are different between nerves and muscles, indicating that they are subject to distinct patterning mechanisms.

Collectively, we report differences in the developmental plasticity of the autopod neuromuscular system in response to additional digits. On the one hand, muscle groups seem perfectly able to adapt their patterning to ectopic cues in the polydactyl autopod (e.g. muscle connective tissue and tendon attachment sites), refine their shapes

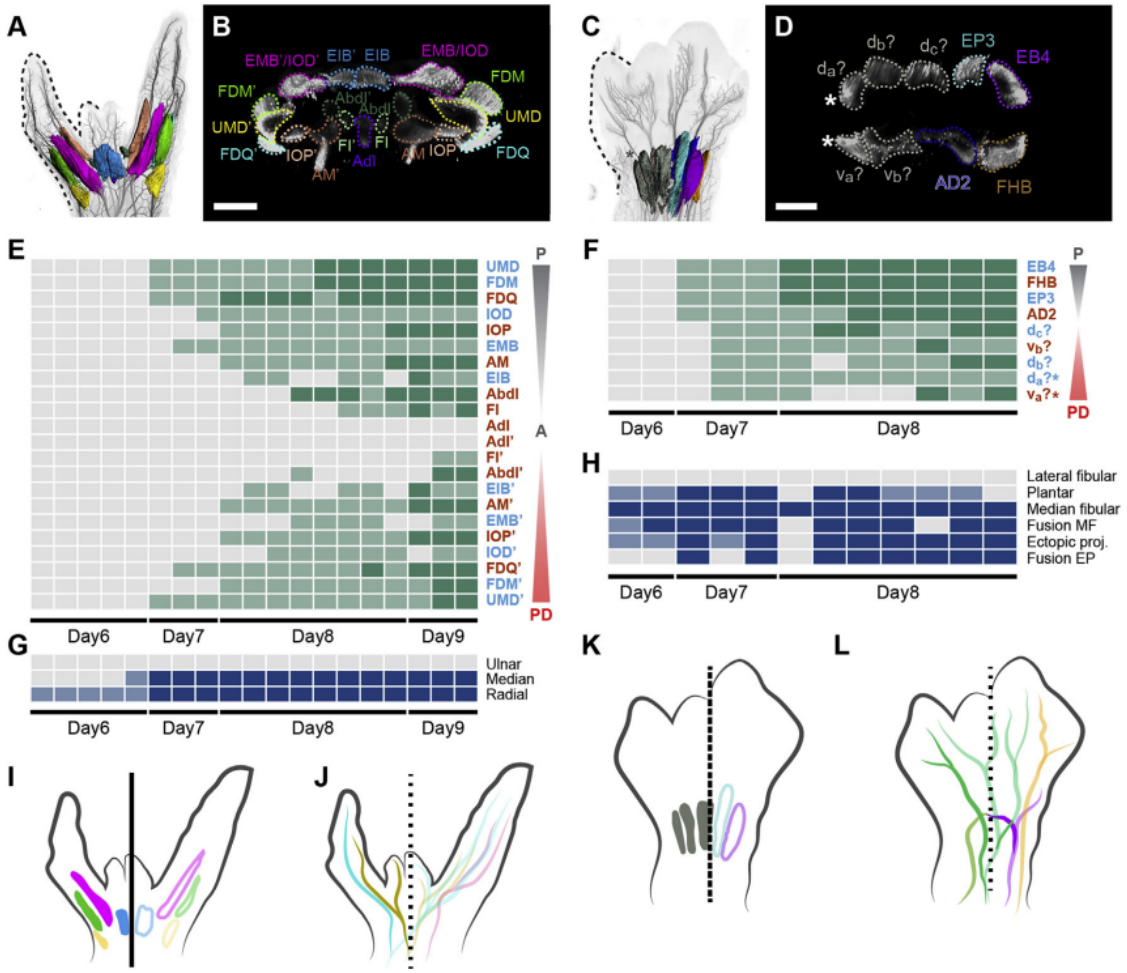

Figure 5: Differential response of muscle and nerve patterning to wing and leg polydactylies (A-D) Full mirror-duplication of the wing musculature (A,B), and extra dorsal and ventral muscle bundles matching the single supernumerary digit in the foot (C,D). (A,B) Dorsal view (A) and virtual cross section (B) of the musculature in a polydactyl wing at day 9 of development. Muscle identity is indicated by pseudo-coloration of muscles groups. (C,D) Dorsal view (C) and virtual cross section (D) of the musculature in a polydactyl leg at day 8 of development. Identifiable muscles are indicated by pseudo-coloration, supernumerary muscles with an asterisk. (E-H) Temporal and spatial appearance of muscle (E,F) and nerve (G,H) pattern alterations. Dorsal (light blue) and ventral (maroon) muscles are arranged top to bottom, from posterior-native, to anterior, to polydactyl side. Muscle masses are scored as partially split (light green) or completely individualized (dark green), nerve alterations (e.g. bifurcations) as partial (light blue) or complete (dark blue, see Material and Methods for details). (I-L) Schematics of muscle and innervation patterns in polydactyl wings (I,J) and legs (K,L). While muscles are completely mirror-duplicated (I, continuous line), or follow the underlying skeletal topology (K, broken line), nerves are only partially responsive (J,L, dotted lines). Only two wing nerves, median (yellow) and radial (cyan), out of three show alterations (J, solid colors). Likewise, the median fibular (green) and plantar (purple) only show changes in morphology (L, solid colors). Moreover, we observe the emergence of an ectopic projection (light green) joining the plantar nerve. A/P, anterior/posterior, PD, polydactyl. For muscle abbreviations, refer to Fig. S3. Scale bars represent approx. 500µm.

accordingly and connect to the underlying skeletal elements (Fig. 5I,K) [92, 104, 225, 226].

Invading nerves, on the other hand, show less flexibility in their response to autopod alterations (Fig. 5J,L). They seem constrained by their projection routes, i.e. from where they send axons into the limb periphery, and remain attached to their cell bodies in the

developing spinal cord [208]. Importantly, not only does this physical connection to the spinal cord restrict these nerves sterically, but it is also shapes the molecular make-up of their growth cones via spinal cord-intrinsic patterning systems [184, 208, 227]. As such it modulates the extent to which growing nerves can respond to alterations in peripheral axon guidance molecules. From an evolutionary perspective, our results thereby imply the presence of distinct developmental constraints, due to the need for coordinated patterning alterations in all components of the limb musculoskeletal apparatus. Namely, the fact that nerve projection routes are not entirely dependent on peripheral cues will impose functional patterning barriers that may prevent certain autopod morphologies from being realized. Moreover, the rotated configuration we describe for fore- and hindlimb innervation patterns highlights that any discussion of serial homology and individualization of tetrapod limbs should not focus exclusively on skeletal elements, but consider the entire musculoskeletal apparatus as a functional unit [21, 228, 229]. From a medical point of view, our findings offer a conceptual framework to understand the varying degrees of motor abilities observed in different forms of human hand and foot polydactylies [230, 231].

2.4 Contributions

Experimental embryology and polydactyl induction was done by the author. Lightsheet imaging was carried out by the author at the Imaging Core Facility, Basel, and image analysis pipeline was optimised by the author. Cryosectioning, staining and confocal imaging was done by the author. Wholemount immunostaining was optimised and carried out by Maëva Luxey.

2.5 Material and methods

2.5.1 Experimental polydactyly

Fertilized chicken eggs (Gallus gallus domesticus) were purchased from local vendors in Switzerland. Eggs were incubated, opened and staged according to standard protocols [232, 233]. AG1-X2 resin (BioRad laboratories) were derivatised with formic acid and washed in water to adjust the pH around 4.5-5. They were then soaked in all-trans-retinoic acid (1 mg/ml dissolved in DMSO, Sigma) for at least 20 min at room temperature and washed in DMEM with phenol red (GIBCO™ GlutaMax), before being grafted into the anterior-distal margin of chick wing or leg buds at day 3 of development (HH19) (see [233, 234]. Polydactyl embryos were dissected after 3 to 6 days post implantation. In total, we analysed 19 polydactyl wings with mirror digit duplication and 12 legs with an extra digit.

2.5.2 Whole-Mount immunostaining and tissue clearing

Embryos were dissected and immediately fixed in Dent's fix (4:1 Methanol:DMSO) for at least one week and stored at -20°C until immunostaining. To remove pigmentation and increase signal-to-noise ratio, we bleached the dissected embryos overnight at 4°C in Dent's bleach solution (4:1:1; Methanol:DMSO:hydrogen peroxide) [107]. The following day, samples were re-rehydrated in decreasing MeOH/PBT (1x PBS-1%, Triton X-100) series, washed 2 times in PBT and then blocked for one hour in PBT-5% DMSO-5% sheep serum (blocking solution) at room temperature on a shaker. For double-immunostaining, samples were incubated in blocking solution with primary antibodies against neurofilament (*NF200*, Sigma, dilution 1:500) and muscle specific myosin heavy chain (*MF20*, DSHB, dilution 1:100) and placed at 4°C, with rotation for 2 nights. This was followed by one-hour washes in PBT along the day. Next, samples were incubated in secondary antibodies (α-mouse AF488 and α-rabbit Cy3; Jackson ImmuResearch, dilution 1:500) diluted in blocking solution for 2 nights at 4°C. After 6 washes of one hour in PBT at room temperature, samples were quickly washed 2 times in 1x PBS before clearing. Tissue clearing was carried out with CUBIC method as described previously [235].Briefly, samples went through delipidation in CUBIC 1 solution followed by 2% agarose embedding and 48h incubation in CUBIC 2 solution before imaging.

2.5.3 Light-sheet microscopy

Images were acquired on a ZEISS lightsheet Z1 microscope using the Zen 2014 software (ZEISS). The lightsheet was generated by lasers (wavelength 488nm and 561nm) and dual side illumination was applied (Illumination optics Lightsheet Z.1 5×/0.1 ZEISS). Fluorescent signals were detected with 5X air detection objectives for clearing chambers (Lightsheet Z.1 detection optics 5×/0.16 clearing, n=1.45, ZEISS) and acquired with PCO.Edge sCMOS cameras (liquid cooled, 1920 x 1920 pixels, 16-bit readout). Stained and cleared samples were submerged in a chamber filled with CUBIC 2 solution. Tiles were defined with TileScan (ZEISS) for big samples, step size was optimized by Zen. All images were acquired in 16-bit.

2.5.4 3D imaging and image processing

After acquisition, Zeiss .czi light-sheet microscopy files for all tiles, were loaded in ArivisVision4D (Arivis) and stitched together. All planes were exported (.tiff) and loaded in Imaris 9.1.2 (Bitplane) to create an Imaris file (.ims) and to carry out further analyses. 3D volumes were created, nerves and muscles were segmented by thresholding and surfaces were created with the Imaris "surface" plug-in. Main nerves were identified and pseudo colored (Labels) for visualization purposes. At later stages, surface rendered nerves innervating the skin were removed manually. Optical slices were obtained with the Imaris "Ortho Slicer" and "Oblique Slicer" plug-ins. To visualize the shape of the limbs after surface rendering, the gamma was set to 2 and the maximum value was set

high. Images (.tiff) and videos were created with Imaris "snapshot" and "animation" plug-ins. For figures, separate images of the surface rendered data and the shape of the limbs were taken and superposed in Fiji [236]. Movies, created in Imaris, were put side-by-side and captions were added in Adobe Premier Pro 2017 (®Adobe ®Creative Cloud).

2.5.5 Phenotypic scoring of polydactyl limbs

For phenotypic scoring of polydactyl limbs, we selected only wings showing mirror-image duplications with 43234 or 432234 digit formulas, and legs with five digits. Changes in muscle patterning were scored as 'partial', i.e. differential fiber orientation and elongation at the tip of the bundle (color code = light green, Fig. 5E,F; see e.g. 'Day 7' in Fig. 4B) or 'complete', i.e. individualization of muscle bundles into their characteristic shapes (color code = dark green, Fig. 5E,F; see e.g. 'Day 9' in Fig. 4B) Likewise, we classified alterations in native nerve projection routes into two categories: 'defasciculation' (color code = light blue, Fig. 5G,H; see e.g. arrow in Fig. 3B), and 'complete split' (color code = dark blue, Fig. 5G,H; see e.g. asterisks in Fig. 3B). Moreover, we assessed the emergence of the ectopic projection in the leg (light blue = proximally restricted, dark blue = distally extended), its potential fusion with the plantar nerve (dark blue), as well as the fusion of the median fibular with itself, (light blue = partial, dark blue = complete).

2.5.6 Immunostaining on cryosections

Embryonic tissues were fixed in 4% PFA, cryoprotected in sucrose and sectioned at 20µm thickness. Immunohistochemistry was performed using standard protocols [237]. Samples were stained with primary antibodies against *Tuj-1* (mouse, MMS-435P, 3µg/ml concentration, Covance), *Tag1* (rabbit, kind gift of E. Stoeckli, dilution 1:1000, [224]) and fast Myosin Heavy-Chain (MyHC) conjugated to Alkaline Phosphatase (mouse, A4335; MY32-AP; dilution 1:100; Sigma) in order to visualize all neuron fibers, sensory neurons and skeletal muscles, respectively. Stainings were revealed using fluorescent secondary antibodies (1:500, Jackson ImmunoResearch) or NBT/BCIP reactions.

2.5.7 Confocal microscopy

Confocal images were acquired on an Olympus FLUOVIEW FV3000, using either 10x/0.4 (air, ApoPlan, Olympus) or 60x/1.3 (silicon oil immersion ApoPlan, Olympus) objectives. Continuous laser beams were generated at 488nm and 647nm wavelength (OBIS, Coherent). For 10x overviews, tiled images were stitched in Fiji. All images were globally adjusted for contrast and brightness using ImageJ.

2.6 Supplementary Figures

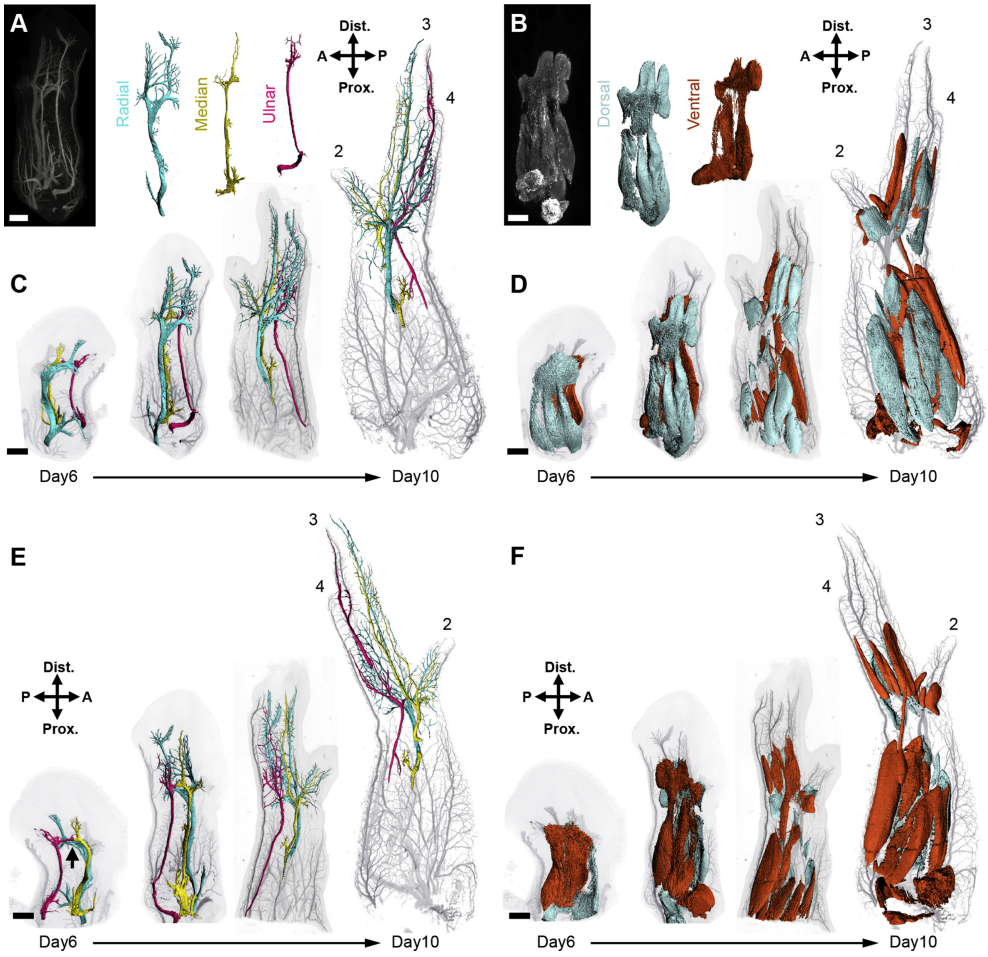

Figure S1. 3D analysis of the developing neuromuscular system in the chicken wing. (A-D) Workflow and dorsal view of the developing wing neuromuscular system. To allow for better comparisons of the dorsal and ventral halves, panels of Fig. 1 are reproduced here. (E) Ventral view of the developing wing neuromuscular system. The two main ventral nerves, the median (yellow) and ulnar (magenta), are joining together to form an arched structure (arrow) before projecting to the digits. The ulnar nerve innervates digit 4 and the median digit 2 and 3. (F) In the ventral muscle masses (red), autopodial muscles are separating from the forearm muscles at a slightly later stage than in dorsal. A/P, anterior/posterior, Prox./Dist., proximal/distal. Scale bars represent approx. 500µm.

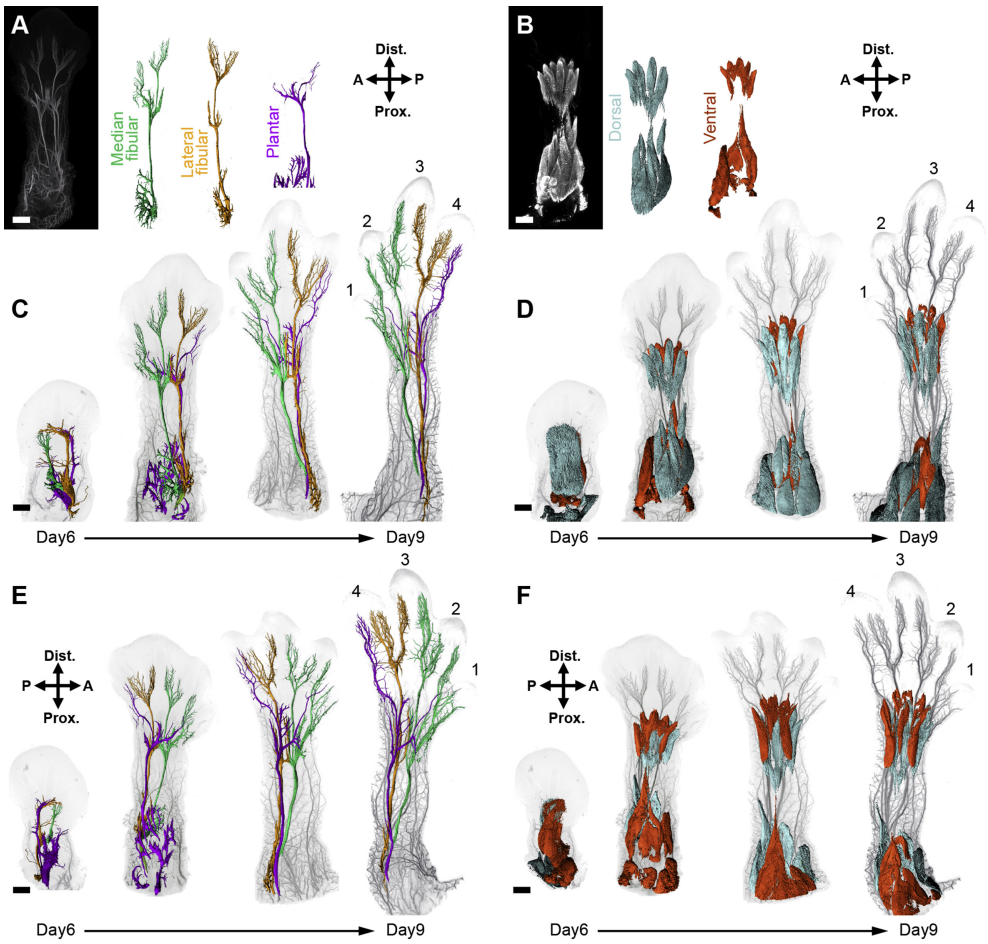

Figure S2. 3D analysis of the developing neuromuscular system in the chicken leg. (A,B) Images showing the workflow for image analysis of lighsheet microscope data. As described in Figure 1, nerves and muscles were stained (NF200 and MF20) then surfaces were created to highlight the structures of interest. (C,D) Dorsal view of the developing leg neuromuscular system. Like in the wing, three main nerves are observed: median fibular (green) and lateral fibular (orange) in dorsal, innervating the dorsal muscle masses (light blue) and plantar (violet) in ventral, connecting to the ventral muscles (red). The median and lateral fibular nerves are joining together and form an arc, similarly to the median and ulnar nerves in wing. (E,F) Ventral view of the developing leg neuromuscular system. The plantar nerve alone innervates all ventral muscles by turning from posterior to anterior. A/P, anterior/posterior, Prox./Dist., proximal/distal. Scale bars represent approx. 500µm.

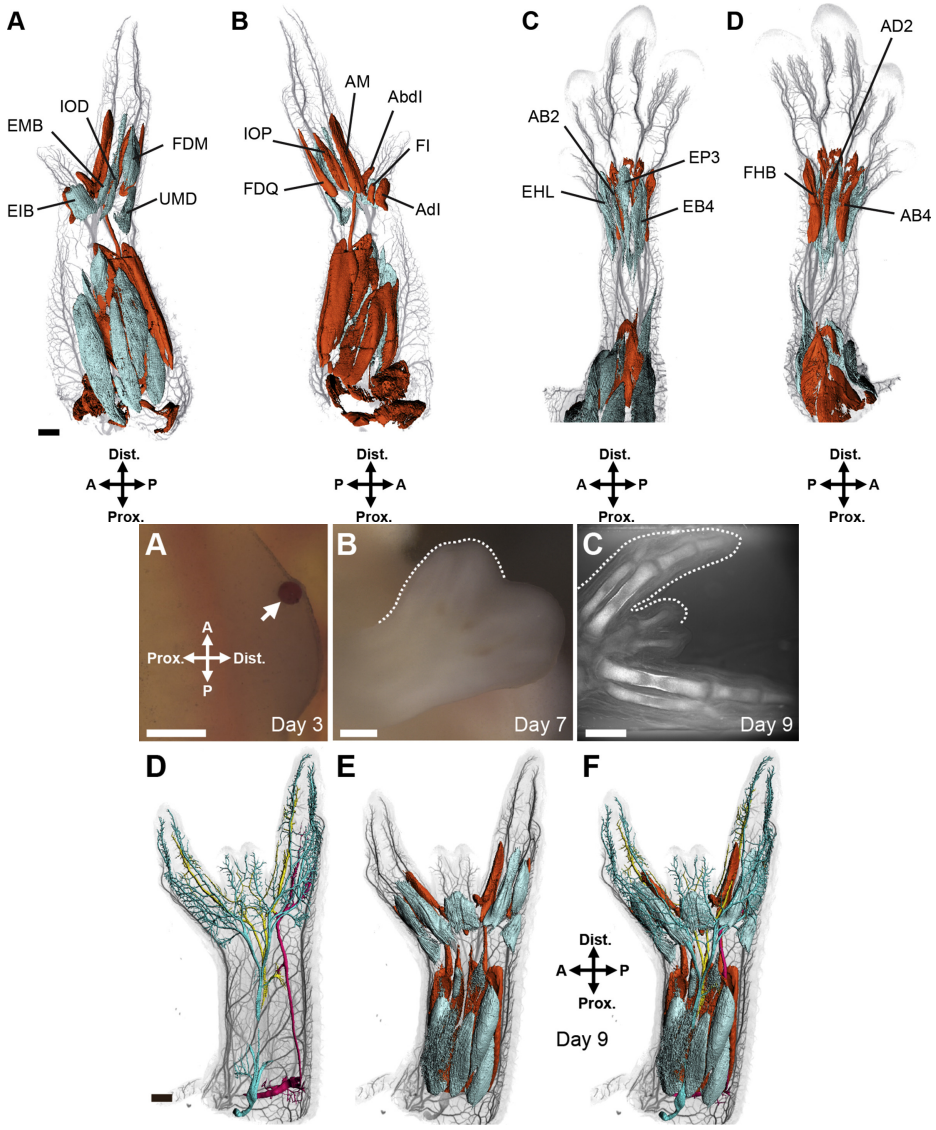

Figure S4. Generating complete mirror digit duplications. (A) Implantation of a RA-soaked bead (arrow), in the sub-AER mesenchyme of an anterior wing bud at day 3. (B) Four days after bead implantation, a mirror duplication of the wing is observed (dotted line). (C) Bright field image after CUBIC clearing reveals a complete digit mirror duplication (dotted line) at the skeletal level at day 9. (D-F) Dorsal view of innervation (D) and muscular (E) patterns, visualized in the same polydactyl wing at day 9 (F). A/P, anterior/posterior, Prox./Dist., proximal/distal. Scale bars represent approx. 500µm.

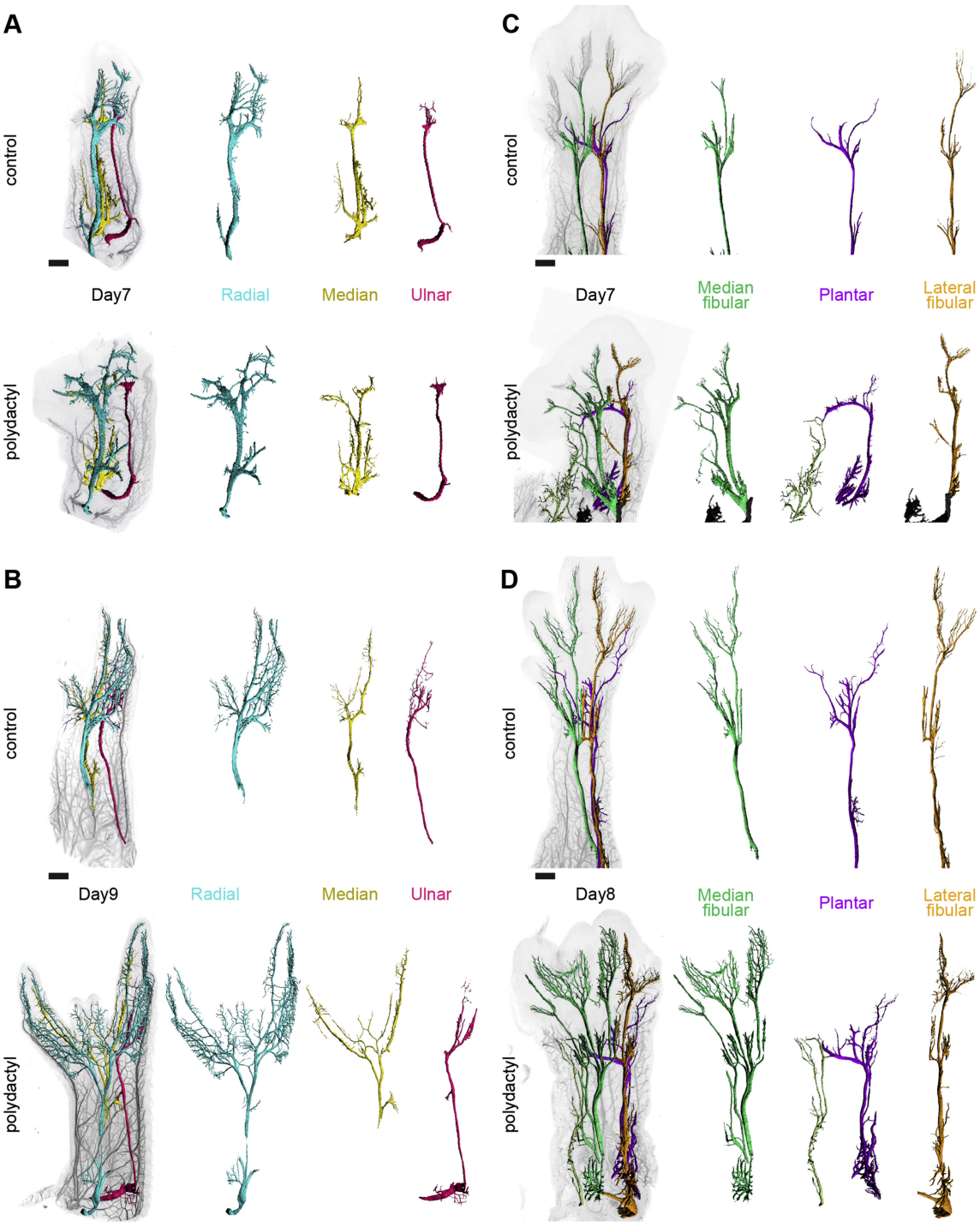

Figure S5. Comparison of innervation patterns in control and polydactyl limbs (A-D) Side-by-side comparisons of innervation patterns for control (top) and polydactyl (bottom) wings (A,B) and legs (C,D) at day 7 (A,C) and day 9 (B,D) of development. Scale bars represent approx. 500µm.

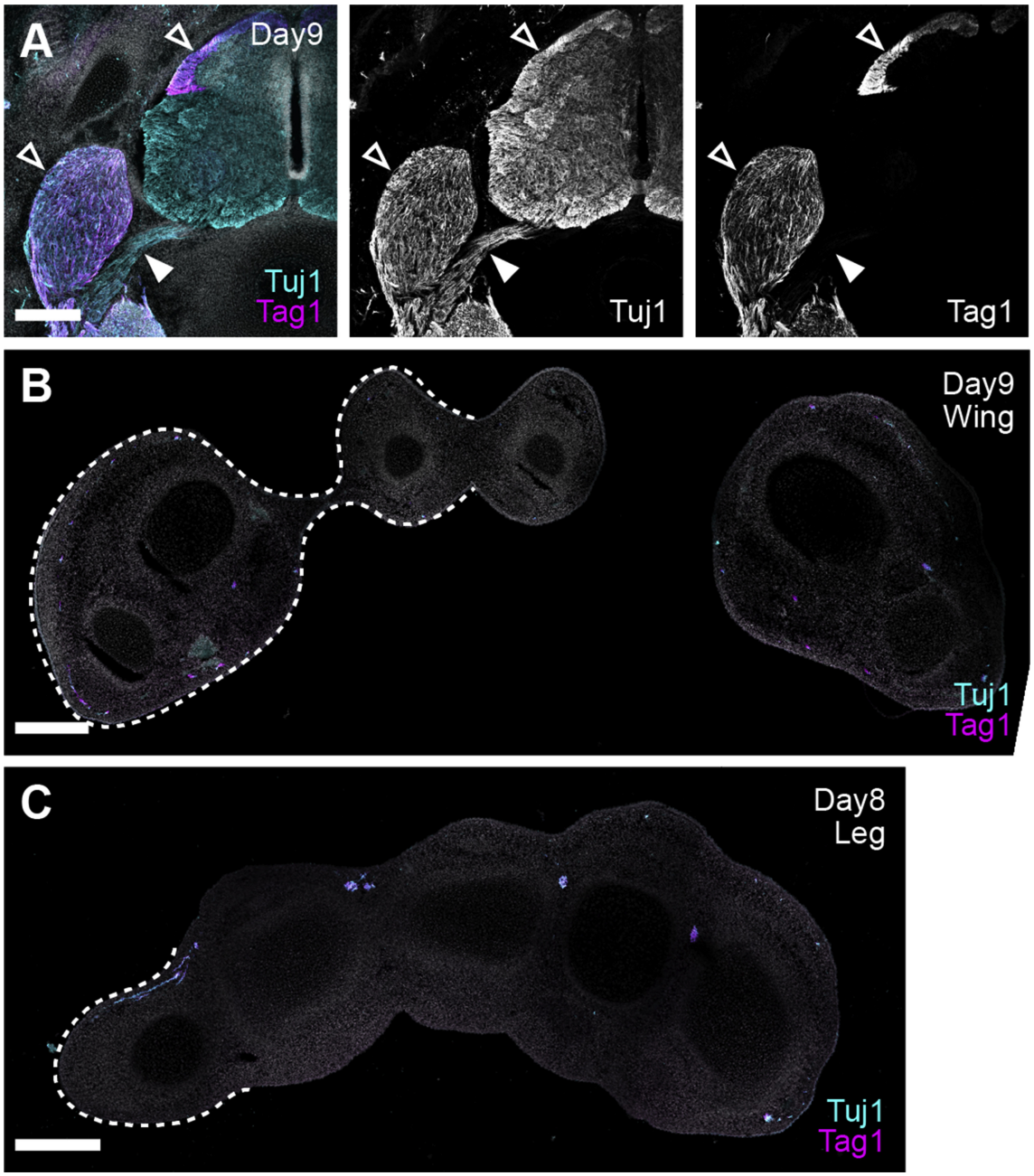

Figure S6. Distinguishing motor and sensory nerves. (A) Double-immunohistochemistry for Tuj1 (pan-neuronal) and Tag-1 (sensory neurons). At brachial levels of the developing spinal cord, Tag-1 marks entering sensory nerves as well as the dorsal root ganglion (empty arrowheads). Tuj1, however, stains all neuronal structures, including Tag-1-negative motor axons exiting ventrally from the lateral motor column to project to the limb periphery (arrowhead). (B,C) At distal levels, i.e. past the autopod musculature, only Tuj1/ Tag-1 double-positive nerves are detected, both in the wing (B) as well as the leg (C).

Chapter 3

Plasticity of the central nervous system and changes in muscle fiber-type in response to polydactyly

3.1 Abstract

The assembly of the neuromuscular system is key for movement execution. During embryonic development, motor neurons are generated in excess in the spinal cord and only the ones receiving target-released factors through their axons will survive the programmed cell death wave and gain the final motor neuron pool identity. Our previous data showed muscle duplication in polydactyl embryos and ectopic branches connecting to the duplicated muscles. The availability of extra muscles and their apparent innervation by ectopic projections made us question how motor neuron survival and motor neuron pool identity are modified in polydactyly.

Using chicken mirror image duplication polydactyl models, we compared motor neuron numbers during the period of naturally occurring neuron cell death. Decreased motor neuron numbers and increased LMC neuron death were observed in the rostral polydactyl spinal cord, which we correlated with muscle patterning changes and fiber-type shifts in the peripheral muscles. In an attempt to uncover motor neuron pool identity changes in the polydactyl neural tube, we performed single-cell RNA-sequencing on polydactyl and control spinal cords. The data set revealed slight cell-type distribution differences in the two types of neural tubes but failed to capture enough motor neurons to shed light on motor neuron pool identity changes. Despite these difficulties, potential digit-specific motor neuron pool markers were identified.

Together, these results show that polydactyly perturbs the patterning and cellular composition of muscles, consequently the decrease innervation efficiency and motor neuron survival. Further work will aid in uncovering motor neuron identity in polydactyly, and learning more about motor circuit formation in the presence of extra digits.

3.2 Introduction

Accurate innervation of muscles by motor neurons is key for locomotion and fine motor control. A multitude of muscles constitute the tetrapod limb and for movement to occur, flexor and extensor muscles are required to work in a synchronized manner [238]. During limb development, bones are formed from the condensation of mesenchymal tissue and muscle progenitors are migrating from the dermomyotome. Later they form muscle bellies attaching to the skeletal elements via tendons [239–241]. For movement control, spinal motoneurons are projecting axons toward the muscles to connect them to the central nervous system and regulate muscle fiber contraction [208]. Together these structures, originating from various embryonic tissues, form a functional neuro-musculo-skeletal apparatus of the limb.

Spinal neurons are born from stem cells at the ventricular zone of the neural tube [121, 129, 242]. The position and identity of the progenitors are defined by different gradients of morphogens along the dorso-ventral and rostro-caudal axis. Sonic hedgehog (SHH) expression by the notochord and floor plate, as well as WNT and BMPs diffusing from the roof plate, determine the different dorso-ventral layers of progenitors, from which post-mitotic neurons are born [129, 243]. Simultaneously, rostro-caudal position is dictated by retinoic acid (RA) and fibroblast growth factor (FGF) inducing HOX gene expression [152, 153]. Limb innervating motoneurons acquire their fate under the influence of HOXC6, HOXC8 at the brachial, and HOX10 at the lumbar level, and they are grouped in the lateral motor column (LMC) [121, 142, 155]. Later in development, they are further divided into median and lateral LMCs before they project axons into the limb and navigate mesenchymal axon guidance cues to reach their target muscles [244].

Spinal motor neurons are produced in excess at the early stages of development. It is estimated that more than double of the needed cells is generated and a wave of apoptosis adjusts the number of motor neurons [245]. The connection between targets in the periphery and motoneuron death or survival has been studied since the beginning of the 20th century, when the first limb ablation experiments were performed on chicken embryos [246]. Those experiments provided evidence that in absence of limb targets, motor neurons undergo cell death, even if the limb is removed before the initiation of axon projections (day 3 of development), indicating that LMC neurons are unable to survive in absence of the periphery. This observation brought about the hypothesis that systems matching with post-synaptic targets are crucial for spinal motor neuron survival.

Later research focused on uncovering the factors present in the periphery influencing motoneuron survival. Chicken embryos and *Xenopus* tadpoles with additional grafted legs showed decreased motor neuron death in the lumbar LMC, presumably due to 'quantitative matching' between available muscles and motoneurons [247, 248]. However, hormonal enlargement of Xenopus tadpoles before metamorphosis and quail-chick leg bud swaps demonstrated that the effective size of target muscles is not the

determining factor for motor neuron survival, but available synaptic sites and number of myotubes are [249, 250].

Synaptic connections are key for the control of muscle contractions and the survival of motor neurons. Pharmacological paralysis of chicken embryos in-ovo by curare or α-Botulotoxin prevented programmed cell death in the lumbar LMC [251]. Conversely, electric overstimulation or pharmacological activation of limb muscle contraction enhanced motoneuron cell death [252]. During target muscle innervation, the neuron's electrical properties and firing pattern must match the fiber type. Muscles are constituted of slow-twitching (Type I) and fast-twitching (Type II) muscle fibers [100]. In mammals, these two fiber types are intermingled within a muscle, but in chicken embryos, those fibers are separated. Entire muscles are built from fast fibres (such as posterior iliotibial) or contain discrete fast/slow regions (as illiofibularis) [253, 254]. Interestingly, previous studies showed that motor neurons are determined to innervate fast or slow muscles very early on. In experimental embryonic limb rotation, limb translocation, motor neurons are "forced" to innervate different muscles, the neural projections tend to connect to the same fiber types as their original target. [255, 256]. Motor neuron numbers seem not to be affected by projecting to a different muscle fiber type, but this aspect needs further investigation [257].

Intriguingly, not only motor neuron survival is affected by contact with peripheral targets, but also by the molecular signature of motor neurons. Post-mitotic LMC neurons strongly express the Hox co-factor FOXP1 [140]. Dorsally projecting lateral LMC and ventrally projecting median LMC neurons express *LHX1* and *ISL1*, respectively [143]. Limb innervating motor neurons are further divided into smaller functional units, so-called motoneuron pools, under the control of HOX factors, to ensure proper pathfinding and muscle connectivity [139, 184]. Motoneuron pools are sets of neurons innervating one particular muscle. Prior to contact with their target, axons navigate a complex environment interacting with multiple axon guidance molecules until they reach the accurate muscle. Hox-induced, motor neuron pool-specific transcription factors, e.g. NKX6.1, RUNX1, POU3F1, are necessary for correct guidance [139, 183]. Interestingly, muscle target-derived GDNF is required for the expression of PEA3 in motoneurons, to further refine the respective motoneuron pool identity [191].

Our previous publication studied in depth the early development of limb neuromuscular system up to mid-gestation, described in detail the spatio-temporal dynamics of muscle belly formation and nerve connections in 3D [258]. Moreover, in surgically generated polydactyl chicken embryos, we demonstrated the plasticity of the peripheral muscle and nerve projections in response to changes in the skeletal pattern. Briefly, in chicken embryonic limbs with mirror image duplication, muscles in the autopod are also mirror image duplicated and follow perfectly the skeletal pattern. As a result, a fully polydactyl limb has seven extra muscles and 3 extra fingers. As for the innervation, ectopic projections of the radial (in dorsal) and median (in ventral) nerves are projecting into the duplicated side, while the ulnar nerve seems unaffected by the presence of extra digits.

As the interaction and communication between motor neurons soma in the spinal cord and the periphery is crucial for proper motor wiring and motor neuron survival, we focused our attention on the spinal motor neurons. Based on previous studies, we hypothesized that due to the presence of a higher number of muscles in the polydactyl limb, nerves have more targets to connect to, hence more motoneurons might escape cell death. Furthermore, the anterior ventral duplicated muscles (FDQ' and IOP') are connected by the median nerve branches while their posterior counterparts are normally innervated by the ulnar nerve. Following the logic of "one motor pool – one muscle", we expect reorganization/expansion of certain motor neuron pools compared to others or even the apparition of a new motor neuron pool identity with distinct transcriptional footprints.

To address these questions, firstly, we harvested polydactyl embryos at the onset of cell death (day 6), at an intermediate time point (day 8), and at the time when the major wave of programmed cell death in motoneurons is presumed to be over (day 10), and we counted all LMC neurons on sections. Our results suggest that cell death is enhanced among the polydactyl motor neurons in the rostral part – innervating proximal limb muscles – but no major changes were observed in the caudal part, insinuating that the presence of extra muscles in the autopod did not trigger enhanced survival of the motor neurons. These observations are possibly and partially due to muscle identity changes and alterations in the cellular composition of limb muscles. Indeed, immunostaining of slow muscle fibers revealed that the anterior duplicated muscles (FDQ' and IOP') are mostly built of fast muscle fibers instead of slow fibers as their control counterparts.

Secondly, using single-cell RNA sequencing (scRNA-seq) of the caudal-most region of the brachial LMC – as digit innervating neurons are harbored there [148, 157]– in control and polydactyl neural tubes, we provide the first transcriptomic data for mid-gestation chicken embryo spinal cord. From our data set, we recovered all major cell types and looked for overrepresented or (solely) present cell types in control versus polydactyl neural tubes. This analysis revealed a myelin-forming oligodendrocyte group expressing *PMP2* on top of other myelin genes such as *MBP* and *PLP1* to be enriched in the polydactyl spinal cord. Furthermore, we captured a higher number of spinal fluid-contacting neurons (CSF-cN) in the polydactyl neural tube compared to the control. These findings require further expression pattern and functional analysis in order to validate their relevance in this context. Lastly, although only a small number of motor neurons were captured by the emulsion-based scRNA-seq, re-clustering of cholinergic neurons from our data set provided potential molecular markers for different groups of motor neurons at this developmental stage and projecting toward the autopod.

Collectively, our results show evidence that in mid-gestation polydactyl embryos the changes in muscle identity and cellular composition alter spinal motor neuron cell death. Furthermore, we provide a scRNA-seq data set of the developing neural tube in control and polydactyl chicken embryos, which revealed future molecular markers for motor

neuron groups. Also, our data set can serve as a valuable resource for future cross-species comparative studies of spinal cord development.

3.3 Results

3.3.1 Motor neuron number in polydactyl chicken embryos

Almost double of the needed amount of motor neurons are generated during development and LMC neurons are competing for target-derived trophic factors for survival (Figure 1A) [245, 259]. Retrograde axonal tracing experiments uncovered motoneuron positional changes in polydactyl chicken embryos, however, the effect of extra digits on the survival of motoneurons remains unexplored [215].

To address this, we used experimentally manipulated chicken embryos with mirror-image duplications in the wing. Polydactyl chicken embryos are particularly interesting and convenient models for this study as it is not a result of genetic mutation or systemic treatment of the embryo with drugs. Only one limb receives a local source of retinoic acid that triggers polydactyly, while the contralateral limb develops normally (Figure 1A). Consequently, the LMC neurons innervating the unoperated limb are supposed to develop normally, while motoneurons projecting to the polydactyl limb potentially have to adjust. Importantly, however, both can be observed simultaneously on neural tube sections within the same individual (Figure 1A).

To evaluate possible changes in motor neuron numbers, we counted all FOXP1 positive cells in the brachial LMC in operated embryos. On day six (HH29), when innervation of limb muscles and cell death is initiated, there are no detectable differences in motor neuron numbers between polydactyl and control side (Figure 1B). On developmental day 8 (HH34), approximately from the middle of the LMC toward the rostral end 15% fewer motoneurons were counted in the polydactyl limb innervating LMC, than in the control LMC (Figure 1C). This effect was accentuated on day 10 (HH36), as the polydactyl LMC contained 23% less FOXP1 positive neurons. At the caudal end, we observed a slight trend of polydactyl embryos having more motor neurons, especially at day 10, which is more visible when the ratio 'control/polydactyl' is plotted (Supplementary Figure 1C).

However, it is far less pronounced than the difference at the rostral end. Furthermore, the variability among biological replicates is substantial: we observed vast differences in motor neuron number among individuals possibly due to slight age differences despite the thorough staging of the embryos. Embryo 'b' for example illustrates this difference well at day 10: it was harvested seven days after operation, but the LMC is shorter, with a higher number of motor neurons per section, and thus resembles the profile of a younger embryo (Supplementary Figure 1C).

Somatic spinal motor neurons stop being produced after 5.5 days of development, as the progenitors switch to oligodendrogenesis [260, 261]. As of day 6 the neuron numbers are

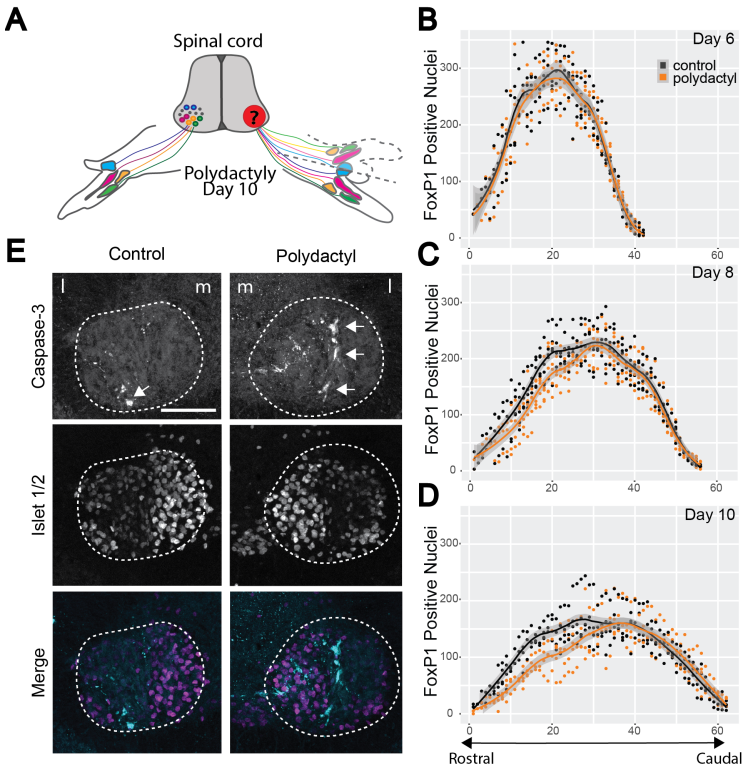

Figure 1: Impact of polydactyly on programmed cell death of LMC motor neurons (A) Schematic representation of target-related motoneuron survival and refining of connections. (B-D) Total number of FoxP1+ cells per section (50µm) all along the brachial LMC at (B) day 6 (n=5), (C) day 8 (n=5) and (D) day 10 (n=4) of development. Orange and black lines represent the mean of control and polydactyl sides respectively. (E) Activated Caspase-3 staining show increased cell death in the LMC of polydactyl limbs (n=2). White dashed lines outline the LMC, and white arrows point to activated Caspase-3 staining. m: median side, l: lateral side; Scale bar represent 100µm

equal between control and polydactyl embryos, which points to motor neuron cell death as the likely cause of the cell number differences observed at later stages.

To address this, we performed activated Caspase-3, a marker of cell death, staining on serial sections on day 8 and compared the cell death rates in control and polydactyl LMCs (Figure 1E). Indeed, at the rostral end of the polydactyl neural tube, more activated Caspase-3 cells were counted. This trend continued along most of the spinal cord. At the caudal end, however, there was no notable difference in cell death between control and polydactyl LMC (data not shown).

Altogether, our data show a decrease in motor neuron number in the rostral LMC innervating the polydactyl limbs, due to enhanced motor neuron cell death. Also, a minor increase was observed at the caudal end of the polydactyl LMC compared to the control one. However, it is less striking than the changes observed in the rostral end. Nevertheless, it might point toward a moderately enhanced survival of caudal – i.e. digit innervating - motor neurons [148, 149, 157]. Next, we intend to explore the possible causes for these changes in motor neuron death.

3.3.2 Cellular composition of muscles and innervation in polydactyl embryos

Besides muscle patterning changes in the autopod, Duprez and colleagues showed polydactyl chicken wings that multiple muscles were missing or shifted towards a posterior identity in the forearm [101]. Furthermore, the composition of muscles in fast and slow fibers was modified. Namely, fast twitching muscles were replaced by slow twitching ones and provided evidence that the rearrangement of the slow twitching

myofibres happens prior to the cleavage of the muscle masses, before innervation is initiated. The changes of anatomical identity and switch in fiber-type potentially antagonize motor innervation, as the electrical property of motor neurons are determined during early specification. Failed systems-matching between neuron and target results in the death of the motoneuron, which could explain the increased cell death in the polydactyl rostral LMC [148]. As the autopod musculature received no attention in previous publications, we decided to analyze the cellular composition in fast- and slow-twitching muscle fibers in control and polydactyl limbs.

We sectioned control and polydactyl limbs and stained them for myosin heavy chains (all muscle fibers) and slow-myosin heavy chains, to distinguish between fast and slow fibers by subtraction. The ventral muscle IOP is mainly built of slow fibers while the FDQ muscle has a distinct dorsal slow fiber region and a ventral fast-type segment (Figure 2A and B). The dorsal autopod muscle FDM is entirely fast-twitching, and the EMB/IOD seems to be slow type.

In the polydactyl autopod, where muscles are mirror-image duplicated, the posterior FDQ muscle shows the same slow-fiber distribution as the control FDQ, while the duplicated FDQ' muscle is composed of fast type. Similarly, the IOP muscle is stained for slow-myosin chain, but the IOP' is not.

Clearly, despite the mirror-image appearance of duplicated muscle in the polydactyl autopod, the cellular composition is different between muscles with similar identities and there seems a shift toward fast-twitching muscle fibers.

3.3.3 Neuron diversity in control and polydactyl spinal cords

Modification of the skeletal and muscle patterning in polydactyl chicken embryos clearly affects motor neurons in the spinal cord. To explore further alterations in the neural tube, we decided to use emulsion-based single-cell RNA-sequencing (10X Genomics) to globally assess the cellular composition of control and polydactyl neural tubes. The aim of this experiment is to capture glial and neuronal cell types and evaluate changes in transcription and cell numbers with a particular focus on digit innervating motor neuron pools.

To this end, we harvested polydactyl embryos at embryonic day 10, dissected the caudal LMC, and separated the control and polydactyl side by cutting the roof and floor plate (Figure 3A). In addition, in two embryos, we trimmed off the dorsal neural tube and processed the ventral part only, in hope of enriching somatic motor neurons, including LMC motor neurons (Figure 3A). A total of 8 samples (four control and four polydactyls) were dissociated and sequenced.

As a first step, samples were combined together in function of the mode of sample preparation: dorsal neural tube trimming or no dorsal neural tube trimming (Figure 3B). Globally, more cells were captured in neural tubes with dorsal trimming, as we aimed to recover 10000 cells per sample instead of 6000 as in the non-trimmed spinal

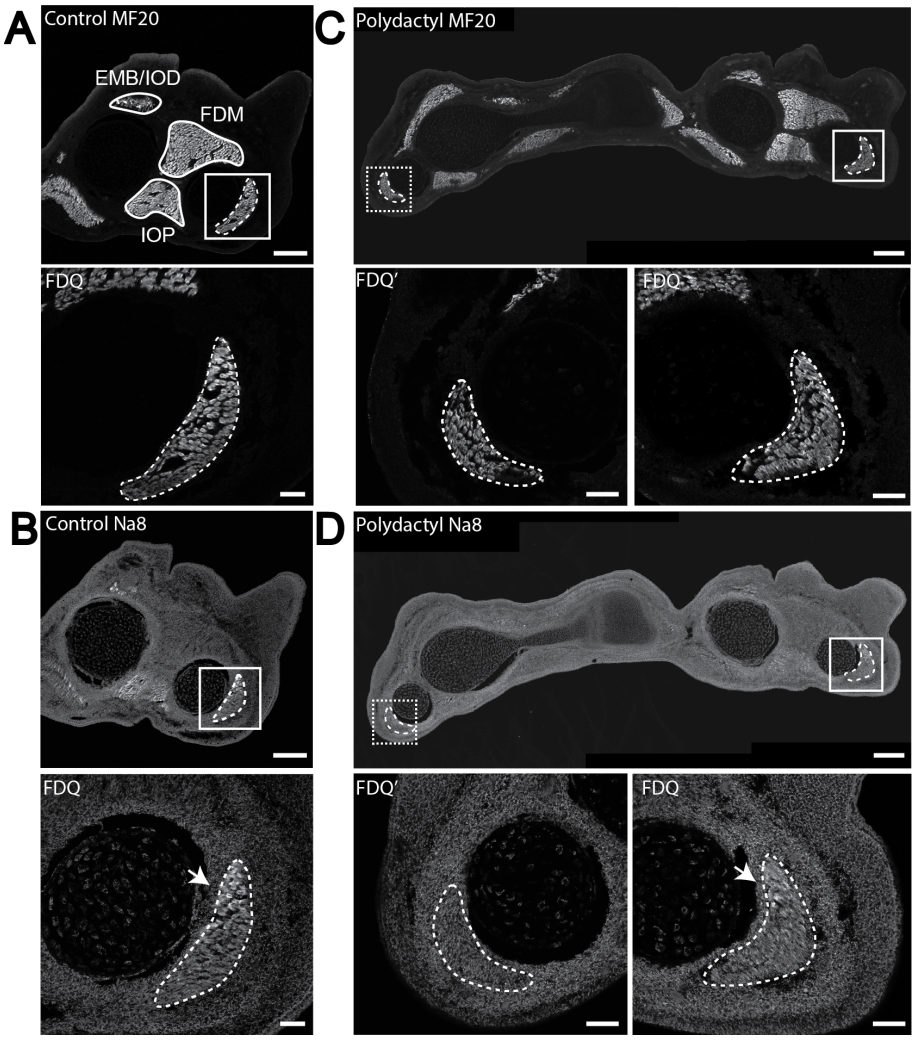

Figure 2: Changes in muscle fiber composition between control and polydactyl limbs (A) MF20 (staining myosin heavy chain) staining on the contralateral limb. The bottom image is a zoom on the most posterior muscle, the FDQ (30X). (B) Na8 antibody staining recognizes slow muscle fibers in control limbs (adjacent slide to (A)). Zoom on the FDQ muscle showed slow muscle fibers in the dorsal part of the muscle. (C) MF20 staining on a polydactyl limb, the mirror image duplication of the posterior muscles can be appreciated. (D) Na8 immunostaining on a polydactyl limb. The FDQ muscle shows a similar phenotype to the nascent FDQ, but Na8 signal is undetectable in the duplicated FDQ' muscle. All images are oriented with anterior on the left, posterior on the right, dorsal up, and ventral down. Scale bar represents 150µm on top images of each panel and 50µm on zoomed-in images.

cord. Cells were clustered together based on highly variable genes and major cell types were identified based on published marker gene expression. We recovered neurons (3155 cells/2086 cells; non-trimmed/trimmed), oligodendrocytes (4624/7950), and neural progenitor cells (6055/10959) in total. In samples without dorsal neural tube, we recovered fewer *TUBB3* positive neuron cells. This is likely due to the elimination of dorsal neural populations. However, despite the removal of the dorsal neural tube, motor neuron marker gene expression (acetylcholine-transferase, *CHAT*) shows a low number of motoneurons recovered in the non-trimmed neural tube and virtually none in

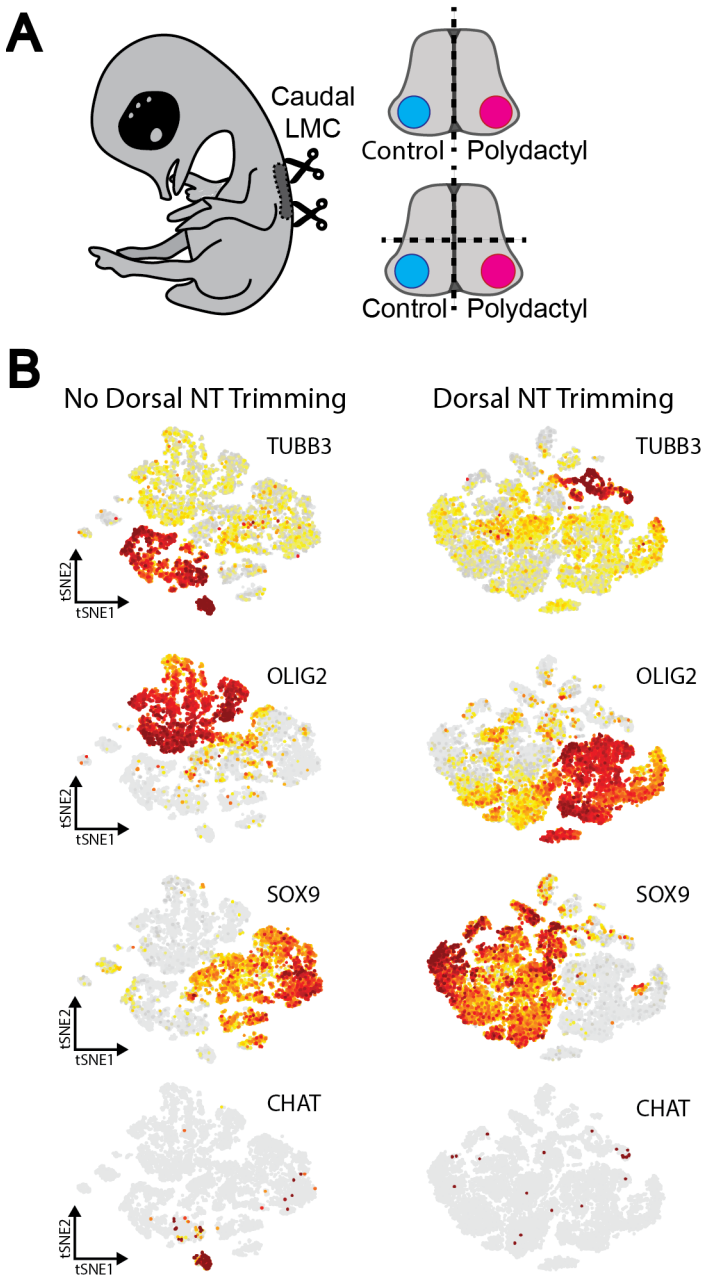

Figure 3: Cellular diversity in the caudal brachial neural tube (A) Overview of the sample preparation workflow for single-cell RNA-sequencing. The caudal brachial neural tube was dissected in polydactyl embryos at developmental day 10. In 2 embryos the roof and floor plate were cut resulting in two control as well as two polydactyl samples. In two additional embryos, the dorsal neural tube was trimmed off in order to enrich ventral horn neurons producing – including motor neurons - resulting in two additional control and polydactyl samples. All dissected neural tube segments were dissociated, loaded on 10X Chromium microfluidic chips, and sequenced individually giving 8 samples in total. (B) tSNE plot of combined samples without dorsal neural tube trimming (control 1/2 and poly 1/2) and with dorsal neural tube trimming (control 3/4 and poly 3/4). Major cell types were identified by the expression of *TUBB3 (TUJ1)* (neurons), *OLIG2* (oligodendrocytes) and *SOX9* (neural progenitors and other glia). By the expression of Choline Acetyl Transferase (*CHAT*) the group of cholinergic motor neurons was identified.

the trimmed (Figure 3B).

Next, we integrated all eight samples, clustered them, and identified the cell types in more detail (Figure 4A). Described marker genes were used to annotate a total of 35 clusters belonging to 13 distinct cell types. We identified 1) eight clusters of neural progenitor cells (NPC), also called, radial glia (RG) by the expression of *SOX2, SOX9, FABP7* and *SLC1A3*; 2) 9 clusters of oligodendrocyte progenitors (OPC) by *SOX8, SOX10, OLIG2* and *PDGFRA*; 3) 4 clusters of myelin-forming oligodendrocytes (MFOL) by *MBP* and *PLP1*; 4) a small progenitor pool by *NOTCH1, HES5, HES6* and *DLL1*; 5) 4 neuron clustersby *TUBB3, NEFL, NEFM, NEFH*; 7) Motor neuron (MN) cluster by *CHAT, SLC18A3*; 8) 2 distinct clusters of the floor plate (FP) by *SHH, NKX6.1*; 8) a roof plate (RP) cluster by *RESPO1, LMX1B* and *MSX1*; 9) one microglia cluster by *CSF1R, TREM2*

; 10) two clusters of blood (BL) by *HBBA* and *HBA1*; 11) one cluster of blood vessel cells by *CDH5*, *CLDN5*; 12) a cluster of cerebrospinal fluid-contacting neurons (CSF-cNS) by *GATA2/3*, *PKD2L1*; and 13) one cluster of boundary cap cells (BC) by the expression of *EGR2* (also known as *KROX20*).

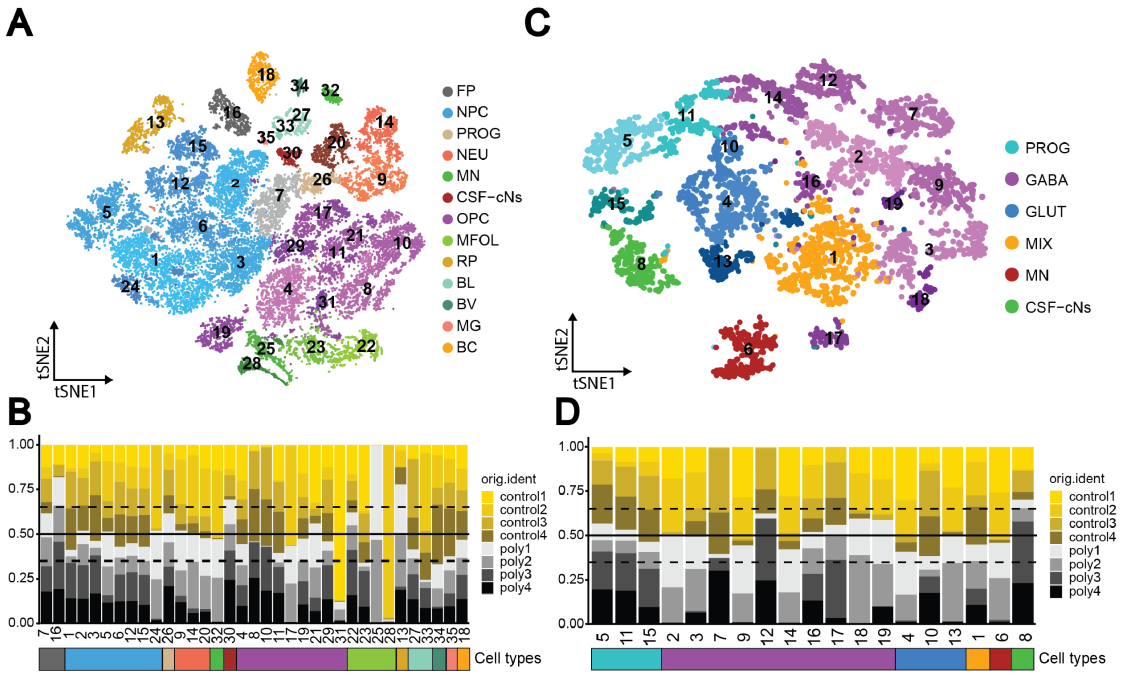

Figure 4: Integrated analysis of all cells combined together from all 8 samples (A) tSNE plot and clustering of all 8 samples integrated together. Each cluster was identified using published cell type markers. Abbreviations: Floor Plate (FP), Neural Progenitor Cells (NPC), Progenitors (PROG), Neurons (NEU), Motoneuron (MN), Spinal Fluid-Contacting Neurons (CSF-cN), Oligodendrocyte Progenitors Cells (OPC), Myelin-Forming Oligodendrocytes (MFOL), Roof Plate (RF), Blood (BL), Blood Vessels (BV), Microglia (MG), Boundary cap cells (BC). (B) Barplot showing the distribution of cells coming from different samples, scaled by the size of the clusters. Shades of yellow represent control samples, and shades of gray show polydactyl samples. The black line represents 50%, the dotted lines represent 35% and 65%. (C) Clustering of all neurons (*TUBB3*+ also called *TUJ1*) cells to identify the neuron types captured by the single-cell experiment. Abbreviations: Progenitors (PROG), GABAergic inhibitory neurons (GABA), Glutamatergic excitatory neurons (GLUT), Mixed GABAergic and Glutamatergic (MIX), Motoneurons (motor neuron), Spinal Fluid-Contacting Neurons (CSF-cN). (D) Barplot displaying the distribution of cells coming from different samples among clusters. Shades of yellow represent control samples, and shades of gray show polydactyl samples. The dotted lines represent 35% and 65%, the black line represents 50%.

To see whether certain cell types are overrepresented in control or polydactyl samples, we plotted how cells of the different samples are distributed among the 35 clusters (Figure 4B). Most clusters from the NPC-s and OPC-s are well balanced between control and polydactyl samples. Overall, progenitors seem to be easier to dissociate and capture resulting in an overrepresentation of those populations in our setting, compared to histological assessments of the relative sizes of these populations. Several clusters indicate technical or sampling issues, such as cluster 24 (NPC) which only contain cells from three samples out of eight, and cluster 28 (MFOL) solely composed of cells from one sample. Cells from polydactyl samples are overrepresented in clusters 13 and 16.

However, those represent RP and FP, whose numbers can be easily affected by the dissection during the separation of the two halves of the neural tube (Figure 3A).

Oligodendrocyte progenitor clusters 8 and 10 are mostly composed of cells from control 3-4 and polydactyl 3-4. Inspection of Hox gene code has shown that the neural tube pieces dissected in embryos 1 and 2 (resulting in control 1-2 and polydactyl 1-2 samples) are slightly more caudal than in embryos 3 and 4. This might explain that some clusters are only composed of cells originating from embryos 1-2 or embryos 3-4. Possibly, oligodendrocyte progenitor cells are moderately differentiated according to their position along the antero-posterior axis.

Interestingly, however, clusters 22 and 23 are both myelin-forming oligodendrocytes, but cluster 22 contains more cells from polydactyl samples and 23 cells coming from control samples. This might reflect a shift in the oligodendrocyte population or oligodendrocyte maturation between control and polydactyl LMC. Genes differentially expressed between the two clusters showed that while both clusters expressed myelin-forming genes such as *PLP1*, *MBP* or *NCP*, cluster 22 is a *PMP2+*, *NFASC+*, *NCAM1-* and *NKX2.2-* population while cluster 23 is *PMP2-*, *NFASC-*, *NCAM1+* and *NKX2.2+*.

As a next step, we used *TUBB3* (also called *TUJ1*) to select the neuron population and re-clustered in order to identify specific neuron subtypes. This allowed us to identify the motor neuron cluster (MN) (*SLC18A3, CHAT*), 9 inhibitory (GABAergique) clusters (*GAD1, GAD2, NRXN*3) and 3 excitatory (Glutamatergique) neuron clusters (*SLC17A6, TLX3*), 3 progenitor clusters (*SOX9, FABP7*), and a cluster of CSF-cNS (*PKD2L1*) (Figure 4C). As above, we inspected the distribution of cells in these clusters according to their sample of origin. Some distributions seem to reflect the dorsal trimming of the neural tube as dorsal populations only comprise control 1-2 and poly 1-2, such as clusters 5, 9, 13, and 18. However, as ventral populations are showing similar tendencies (cluster 2, 6 (motor neuron), and 14) it might be due to dissection or sampling issues. Also, a higher number of the cerebrospinal fluid contacting neurons (CSF-cNs, cluster 8) neurons were captured in polydactyl samples.

Lastly, we took the motor neuron cluster (294 cells) and decided to re-cluster and look for coherent molecular signatures among them (Figure 5A-B). In the resulting six clusters two (cluster 5 and 6) expressed *HOXC8* (see Figure 5B), a hallmark of caudal brachial LMC, all others expressed *HOXC9*, sign of a thoracic identity [153]. *FOXP1* and *ISL1* were strongly expressed in cluster 3, 5 and 6 indicating LMC identity. Differentially expressed (DE) gene analysis was performed among the clusters, and significantly expressed genes are represented in Figure 5B. These genes represent a variety of gene families, with different functions such as signalling molecules (e.g. *MAPK4, NOG*), transcription factors (e.g. *DBX2, RUNX2, LMO1*), axon guidance molecules (e.g.*SLIT2, SEMA3C /5B*) and cell adhesion molecules such as cadherins (*CDH2*), proto-cadherins (*PCDH8 /9 /17*) and receptor-type protein tyrosine phosphatases (*PTPRO /RD /RT*). Cell adhesion molecules were shown to be involved in motor neuron pool formation and maintenance and their

combinatorial expression plays a role in motor neuron pool positioning [147, 262, 263]. Furthermore, cell adhesion molecules, such as protocadherins are involved in axon fasciculation [264–266].

The expression patterns of selected genes ($\sim$ 4 of each cluster) were studied by in situ hybridization at embryonic day 10. Several genes from different clusters gave no signal at all (for example *PLXND1*, *PCDH18*), possibly due to no expression in the exact segment of the embryo section, or because the gene is not expressed at all. Others were restricted to a subset of motor neurons, however, genes present within the same cluster showed little coherent expression patterns (Figure 5C). Cluster 2 seems to regroup Medial Motor Column (MMC) motor neurons as most genes are strongly expressed in the MMC (Figure 5C). Genes from cluster 1, 3 and 6 showed broader, such as *CADM1*), or more restricted expression pattern such as *PCDH17* or *PLXNA4*. Interestingly, in cluster two, the RA signalling antagonist *CYP26B1*, a BMP antagonist, *NOG* and a BMP effector (mostly in chondrogenic context) *RUNX2* are present among the differentially expressed genes [267–269]. Furthermore, cluster 6 expresses Follistatin-like 5 (*FSTL5*) which is also a BMP antagonist [269]. This might reflect the active repression of RA and BMP signaling in the motor neurons at this stage of development.

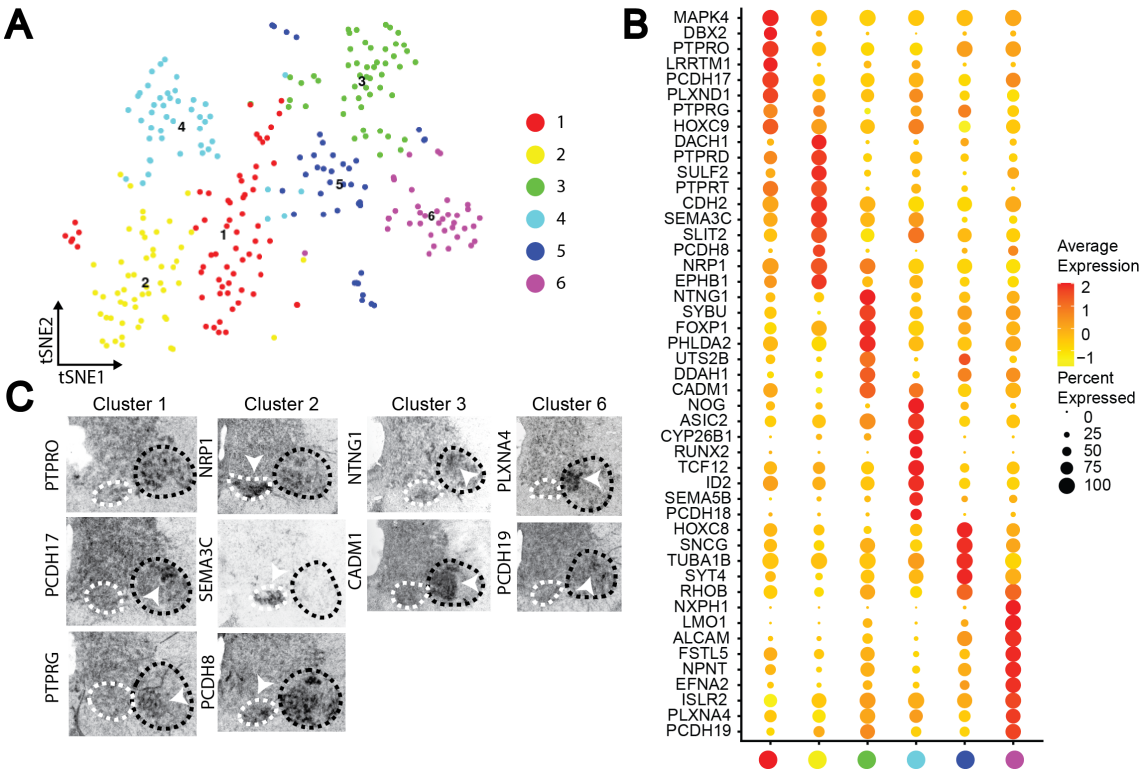

Figure 5: Sub-clustering of motoneurons captured by scRNA-seq (A) tSNE plot and subclustering of *CHAT*+ cells. (B) Differentially expressed genes among the six motor neuron subclusters represented in a dot plot. (C) Visualization of expression pattern by *in situ* hybridization of cluster marker genes in control neural tubes. The white dashed line represents the MMC, the black dashed line shows the LMC, and white arrowheads point to major expression patterns.

Globally, our data explored the cellular diversity of the caudal brachial LMC for the first

time at single-cell resolution in chicken embryos and attempted to uncover differences between control and polydactyl neural tubes. Our findings showed minor differences in the relative proportion of certain cell types, between control and polydactyl. We showed an overrepresentation of a particular mature oligodendrocyte population and CSF-cNs in the polydactyl neural tube. The low number of motor neurons captured by this technique did not allow us to unveil significant differences in motor neuron pool identity between control and polydactyl data sets. However, genes restricted to a subset of motoneuron population identified in this work will provide valuable candidates for future, more targeted studies.

3.4 Conclusion and discussion

All limb locomotor output is the result of the functional interaction of the central nervous system and the peripheral musculature. During development, the establishment of precise connections between the muscles and motor nerves is crucial for proper locomotor control, and perturbations can result in major movement impairments. In this study, we addressed how changes in the periphery, namely polydactyly resulting in supernumerary and duplicated muscle groups, affect the development of the central nervous system.

3.4.1 Motor neuron survival in polydactyl embryos

The peripheral neuromuscular system in the chicken wing displays an astonishing degree of plasticity, when confronted with changes in digit numbers [258]. As motoneuron survival depends on contact with muscle targets, and neurotrophic factors released there, we investigated how the availability of extra muscles in the autopod, and the reorganization of muscles in the more proximal limb [101], affected the programmed cell death known to occur in LMC motor neurons.

First, we evaluated the changes in motor neuron number in experimentally generated polydactyl chicken embryos. Our results showed enhanced motoneuron cell death in the rostral LMC on day 8 and day 10 of development. This is potentially a consequence of changes in the environment/musculature in the proximal limb, as rostral motor neurons normally innervate proximal limb muscles [148]. Although we lack information on the phenotype and molecular identity of stylopod muscles (upper arm), in the zeugopod (lower arm) some anterior muscles are posteriorized, with their identity and cellular composition changing and some muscles completely missing [101]. Accordingly, these major changes might negatively affect the pathfinding of the nerves in that area, the accuracy of connections, and hence the survival of the motoneurons missing their original target muscle.

When comparing ratios instead of the absolute number of motor neuron nuclei (Supplementary Figure1), there is a slight tendency toward having more motor neurons at the caudal LMC, at later time points (Supplementary figure 1B). This correlates with the

presence of extra duplicated muscles in the polydactyl autopod. However, if quantitative matching – namely, the number of extra available muscle fibers is directly proportional to the number of surviving motor neurons - was exclusively driving the innervation of muscles, more motoneurons should have survived in the caudal LMC of polydactyl limbs. Possibly, the innervation by the ectopic branch of the median nerve is suboptimal and inefficient, due to the shift toward fast-type muscle fiber, or the lack of appropriate synaptic sites or neurotrophic factors at the ectopic muscle. These last two possibilities are not addressed in this work, but they are potential directions for future studies, for a better understanding of polydactyly and the ensuing molecular crosstalk between nerves and muscles in this model.

How is muscle fiber-type determined, and how could a switch from slow to fast fibers occur? In mice, TCF4-expressing fibroblasts promote the expression of slow-myosin chains. Moreover, TCF4 expression also serve as spatial blueprint to pre-pattern limb muscle masses [90, 91]. Additionally, SHH was shown to promote slow-twitching muscle fiber development, via Prdm1a, in zebrafish. Duprez and colleagues arrived at a similar conclusion about SHH in their studies of the polydactyl zeugopod [101, 270]. However, our results do not seem to follow the same logic, as the induction of an ectopic ZPA at the anterior side in our case resulted in a shift to fast-twitching muscle fiber of the FDQ' and IOP' (Figure 2C-D).

One possible explanation is that the application of RA-soaked beads instead of *SHH* expressing cells or SHH-soaked beads - as other authors used – in the anterior margin results in delayed anterior expression of *SHH*, compared to SHH bead/cell implantation or the endogenous ZPA [47]. It is possible that the early exposure of muscle progenitors to Shh promotes the slow muscle fiber development, and that in our model system this time window is missed. Furthermore, in our work, we use a concentration of RA of 1 mg/ml, as recommended by classical studies [234]. However more recent work proved a 5 mg/ml RA concentration more efficient in generating polydactyl wings, and also might potentially affect muscle fibers differently [47]. To explore this possibility, and learn more about the effect of Shh dynamics on the distribution of slow/fast muscle fibers, one should compare the cellular composition of muscles in wings treated with cyclopamine (Shh antagonist) with control limbs, while also observing the changes in innervation. Moreover, a thorough examination and comparison of Shh- versus RA-generated polydactyl limb muscles might shed light on how the different methods affect muscle fiber type.

From an evolutionary point of view, this data also demonstrates the hurdles that the appearance of a new complex feature, such as an additional finger, can present. The same mechanism that is involved in the formation and patterning of the digit skeletal elements, in this case, Shh signaling, might not be enough to ensure the correct soft tissue anatomy and corresponding molecular identity of the connected nerves. On the contrary, although ectopic Shh expression can induce extra digits, it also perturbs more proximal

structures and the molecular identity of muscles which in turn disorganises the overall innervation pattern.

3.4.2 Cell diversity in the spinal cord in case of polydactyly

Single-cell RNA-sequencing has transformed the way how we study cell type diversity in whole embryos or organs. Multiple studies have already exploited this technology to describe in detail the variety of neurons in the embryonic and adult spinal cord [271–274]. We used the same tool on the chicken spinal cord, for the first time, in order to uncover differences in the cellular composition between control and polydactyl spinal cord samples. However, certain limitations of the technology have to be taken into account when analyzing such data. Certain cell types are more difficult to dissociate and capture in cell suspension because of their tight cell-cell connections, and fragility due to size. Hence uneven sampling is inevitable. Spinal motor neurons, in particular, are characterized by large cell bodies and over-proportionally long axonal projections - much bigger than in other neurons or progenitor cell types - that make them extremely fragile and difficult to dissociate [271]. Consequently, even trimming of the dorsal neural tube seemed to fail to enrich our samples for motor neurons. One alternative to single-cell RNA-sequencing is single nuclei RNA-sequencing (snRNA-seq) which has been successfully utilized on adult mice cholinergic neurons, although that particular study also benefits from the advantage of transgenic mice (ChAT-GFP). In snRNA-seq, nuclei suspension is prepared instead of living cell suspension and the mRNA content of the nuclei is sequenced. The quantity of mRNA captured is lower, as the cytosolic compartment is lost, but a more diverse cell population can be captured and studied.

Our analysis identified two myelinating oligodendrocyte clusters that were differentially represented in control and polydactyl samples. Cells from cluster 22, (overrepresented in polydactyl samples) are *PMP2+, NFASC+, NCAM1-* and *NKX2.2-* population while cells from cluster 23 are *PMP2-, NFASC-, NCAM1+* and *NKX2.2+*. Previous work showed that *NCAM* plays a role in mediating the interaction between axon and oligodendrocytes at the onset of myelination [275]. Also, *NFASC* regulate myelin sheet growth, and the loss of *NKX2.2* expression is the sign of an advance state of maturation in oligodendrocyte [276, 277]. In light of this information and the gene expression in our results, cluster 22 oligodendrocytes are potentially in a more advanced maturation state, than cluster 23. The expression of Peripheral Myelin Protein 2 (*PMP2*) was largely described in myelinating Schwann cells, however, in our experimental setting, it is unlikely that we captured Schwann cell populations as they are only present in the peripheral nervous system [278]. Moreover, cluster 22 does not express Schwann cell-specific markers (*KROX20, POU3F1, S100, P75NTR*). It is more likely that mature oligodendrocytes are also expressing *PMP2* and according to our data, that mature population is more represented in the polydactyl spinal cords. Further efforts are needed to investigate the expression pattern of *PMP2* and see the distribution in polydactyl embryos.

Interestingly, a higher number of CSF-cNs were captured in polydactyl samples. CSF-cNs are present in the spinal cord as one of the three cell types constituting the so-called spinal ependymal layer, alongside tanycytes and ependymocytes, around the central canal [279]. The presence of these cells in the spinal cord was shown in fish and mammals, but they are not well studied in avian species [280]. These cells immerse a cilium into the cerebrospinal fluid and they have been shown to sense pH changes of the CSF through acid-sensing ion channel 3 (*ASIC3*)-like and polycystic kidney disease (PKD)-protein-2-like 1 (*PKD2L1*) channels [281]. In case of a change in pH, the firing of these GABAergic neurons modifies the motor activity to regain the correct pH. More importantly, these cells show progenitor-like properties in vitro, and are able to proliferate and differentiate into neurons, astrocytes and oligodendrocytes [282]. However, the function of this population of neurons in the present context is unclear.

Despite technical difficulties, valuable information has been gained about the neuron population and oligodendrocyte maturation in polydactyl and control chicken spinal cord. Furthermore, cells from the motor neuron cluster provided potential digit-specific motor neuron pool markers. Together, our scRNA-seq data set provides a valuable resource for future cross-species studies, across tetrapods.

3.5 Contributions

Sectioning, staining, cell counting, plotting, cell dissociation, cluster annotation, and in situ hybridizations were carried out by the author. 10X Genomics chip loading and library preparation were carried out by Maëva Luxey. The scRNA-seq was performed at the Genomics facility of D-BSSE Basel, ETH Zürich. Bioinformatic analysis and plotting (tSNE, dot plots, bar plots) were carried out by Dr. Christian Feregrino and Fabio Sacher.

3.6 Material and Methods

3.6.1 Experimental mirror image digit duplication in chicken

Fertilized chicken eggs (Gallus gallus) were acquired from vendors in Switzerland. Eggs were incubated at 38°C with 60% humidity for 3 days, then windowed and staged according to the Hamburger-Hamilton developmental table [232]. Resin beads (AG1-X2, Biorad) were formatted in formic acid for an hour and washed with clean water until the pH stabilized around 4.5. The beads can be stored in water at 4°C for a month. Before implantation, beads were incubated in 1 mg/ml all-trans retinoic acid (RA) solution for at least 20 minutes, then incubated in DMEM media (Gibco) until they turned red. A small incision was made between the Apical Ectodermal Ridge and the mesenchyme at the anterior margin of the limb bud and RA-soaked beads were implanted. Eggs were closed with tape and reincubated until the desired stage (3,4,5,6 or 7 days after the operation). In this study, only individuals with digit patterns 43234 and 432234 were included.

3.6.2 Cryosectioning and immunohistochemistry

Polydactyl embryos were dissected on day 6, day 8, and day 10, DiI was injected into the right side of the back to recognize the polydactyl side later on sections. Embryos were fixed in 4% PFA overnight, cryoprotected in 30% Sucrose solution, then embedded in (FSC22 Clear Frozen Section Compound, Biosystems) blocks and kept at -80°C until sectioning. 20µm or 50µm thick sections were cut from caudal to rostral in order to capture the full length of the brachial LMC. Sections were air dried for an hour after and frozen at -20°C until immunostaining. Polydactyl limbs were fixed, cryoprotected, and embedded as described above, 20µm thick sections were cut. Slides were thawed for 15 min, washed in PBS to eliminate OCT, and blocked in PBST (0,1% Triton, 0.02% SDS, 0.002% BSA in PBS) solution for an hour. Primary antibodies FoxP1 (Abcam) and Islet 1/2 (DSHB) were diluted 1/500 in PBST and slides were incubated with the mix in a humid chamber overnight at 4°C. After three PBST washes, anti-rabbit AF647 and anti-mouse AF488 secondary antibodies (1/500) are deposited on the slides, incubated for 2h at room temperature, washed three times in PBST, and mounted with fluorescent mounting media (Agilent). For limb sections, MF20 and Na8 (DSHB) were used at 1/500 dilution on adjacent slides, and anti-mouse Cy3 was used at 1/500 as described above. All slides were treated with DAPI for 15 mins in PBS, then washed and mounted. Slides are kept at 4°C until imaging.

3.6.3 Confocal imaging

Slides were imaged with an Olympus Fluoview (FV3000) confocal microscope using 10x/0.4 objective (air, ApoPlan, Olympus). A laser at 488nm/506nm/647nm wavelength was generated (OBIS Coherent). Tiles were stitched together when needed, with Pairwise-stitching plug-in in Fiji [283]. For FoxP1 counting, Z-stack was acquired with 3µm steps between virtual sections.

3.6.4 Manual nuclei counting and plotting

Z-stack images of neural tubes were opened in Fiji and the contrast was adjusted for better visibility of FoxP1 positive cells. Maximum intensity projections were made and the "Multi-point" tool was used to count nuclei manually on the control and polydactyl side. Numbers per sections per side were registered in an Excel sheet, transformed into a .txt file and imported in R for plotting (ggplot2 package [284]).

3.6.5 Neural tube dissociation and single-cell RNA-seq (10X Genomics)

Polydactyl embryos were harvested at day 10 of development (HH36) in ice-cold PBS, decapitated, and transferred into a black-bottomed SYLGARD™ Petri dish. They were pinned facing down, an incision was made in the middle of the back and dorsal laminectomy was performed to get access to the neural tube. The roof plate and the floor plate were cut with a needle, before dissecting the part corresponding to the caudal

LMC. In 2 embryos polydactyl embryos out of 4, the dorsal neural tube was trimmed off to enrich the samples in ventral horn MNs. Control and polydactyl side were separated into different tubes and processed separately. Dissected caudal LMCs were transferred into 3 ml preheated dissociation media (FACSmax™ media, Amsibio with 0,375 mg/ml Papain, Millipore Sigma) and incubated for 5 minutes in a water bath at 37°C. The first and second trituration was performed with a P1000 pipette tip cut 5mm from the tip and quickly burnt with a Bunsen burner to eliminate sharp edges. The last two triturations were carried out with an uncut P1000 pipette tip. Each trituration was followed by 5 mins of incubation at 37°C. Cell suspensions were centrifugated at 300g for 7 min at 4°C. The supernatant was discarded, and cell pellets were resuspended in 1ml HBSS 5% FBS (ThermoFisher), passed through a cell strainer (Flowmi®, Millipore Sigma) into a 1,5 ml Eppendorf tube and centrifuged again at 300g for 7 mins at 4°C. Cell pellets were resuspended in 100µl HBSS 5% FBS and cell number and viability were assessed with an automated cell counter (Cellometer®, AOPI ViaStain™). Only samples above 80% viability were processed for sequencing. Samples were loaded on Chromium Next GEM Chip G following the manufacturer's instructions (Chromium Next GEM Single-cell 3 Reagent Kits v3.1 (Dual Index); available on https://support.10xgenomics.com), aiming for the recovery of 6000 cells for embryo 1 and 2; and 10000 cells for embryo 3 and 4. cDNA and libraries were prepared following the above-mentioned protocol, cDNA and library qualities were assessed with a Bioanalyzer (Agilent). The sequencing was carried out in the D-BSSE (ETH Zürich, Basel) at the Genomics Facility.

3.6.6 Sequence analysis

The raw sequencing data were processed with Cell Ranger software (10X Genomics) version 3.1.0 (samples with IDs 1 and 2) and version 5.0.1 (samples with IDs 3 and 4) to perform base calling, adapter trimming, and mapping to the GRCg6a chicken genome assembly and its extended annotation, published in [285]. Cell filtering steps were applied depending on sample quality and sequencing depth, applying thresholds excluding cells with more than 4 times the mean UMI counts or less than 20% of the mean, as well as removing cells with a mitochondrial UMI fraction bigger than the median + three times the MAD (median absolute derivation). Cells with a gene to UMI ratio smaller than 15% and less expressed genes than 2/3 of the maximum number of detected genes were also not considered for further analysis. With Seurat v 4.0.0, cells passing the thresholds were imported into Seurat objects by sample and then merged into two objects containing the old and the new samples, as well as a combined object containing all samples. With SCTransform() the objects were then normalized and scaled, regressing out mitochondrial percentage (mt.perc) and number of UMI counts. Using cyclone from the SCRAN (10.12688/f1000research.9501.2) package, cell cycle stages G2M and S were scored to calculate their difference (CC.difference), which was then regressed out together with the previous variables and the sample ID in another run of SCTransform prior to principal component analysis (PCA). The chicken cell cycle covariate cell pairs used in cyclone were obtained by selecting orthologous pairs from the provided mouse

and human gene pairs. Principal component dimensions for t-SNE were selected for each sample as those lying outside of a Marchenko-Pastur distribution (histogram of squared standard deviations) (https://doi.org/10.1016/j.cell.2016.07.054) and used in fftRtsne() (Fast Fourier transform accelerated interpolation based t-SNE) to calculate a normal and exaggerated embedding (10.1038/s41592-018-0308-4). Cell clusters are identified with FindNeighbours() and FindClusters(), using the same dimensions identified above. Based on a tree of clusters in PCA space, terminal sister clusters with less than 20 differentially expressed highly variable genes (var > median(var)) between them are merged. Marker genes are obtained using FindAllMarkers() with the parameters: only.pos = TRUE, min.pct = 0.25, logfc.threshold = 0.5, latent.vars = c("CC.difference"), test.use = "MAST", assay = "RNA", and return.thresh = 0.05. The features used are the var.features of the SCT assay after running SCTransform again regressing out mt.perc, UMI counts, and sample ID. The neuronal subset of the combined data set contains the cells belonging to clusters expressing Tubb3 (clusters "9","14","20","26","30", and "32"). After subsetting, the combined object, the same methods for SCTransform, PCA, tSNE, clustering, and marker detection as above are used. Cell cycle scores are not calculated anew, since they are calculated cell-wise. The motor neuron subset consists of clusters 21 from the Seurat objects containing both control (ctrl1 2) and polydactyl (poly1 2) samples respectively. Those objects were created with the same methods as described above. The objects get a subset for cluster 21 and then split according to the sample ID, resulting in 4 seurat objects (motor neurons from all four samples). Each object gets normalized and sctransformed with mt.perc, UMI counts, and CC.difference regression. Then the four objects are integrated with Seurat's SelectIntegrationFeatures(), PrepSCTIntegration(), FindIntegrationAnchors(k.filter = 20, k.anchor = 20, k.score = 20, dims = 1:20), and IntegrateData() functions. On the integrated assay, PCA is performed, and then the same methods for SCTransform, PCA, tSNE, and clustering as above are used. For FindAllMarkers() the highly variable features (HVF() function) of the "RNA" assay with a variability bigger than the median were considered. The motor neuron object and the objects involved were analyzed with Seurat v3.1.4.

3.6.7 Cluster annotation

The following studies were used to identify cell types in the scRNA-sequencing data set : [271–273, 286]

3.6.8 *In situ* hybridization

Primers for DIG-labeled RNA probes were designed with Primer3 [287]. Chicken cDNA from limb and neural tube was used to generate PCR products for cloning into pGEMT-easy (Promega) vectors. Sequence accuracy, the orientation of the insertion, and the RNA polymerase (Sp6, T7) were determined by Sanger-sequencing. In vitro transcription was performed with the accurate polymerase (GoScript™ Reverse

Transcription Kit, Promega) using a DIG-labelling mix (Roche). In situ hybridization was performed using standard protocols [288].

3.7 Supplementary figures

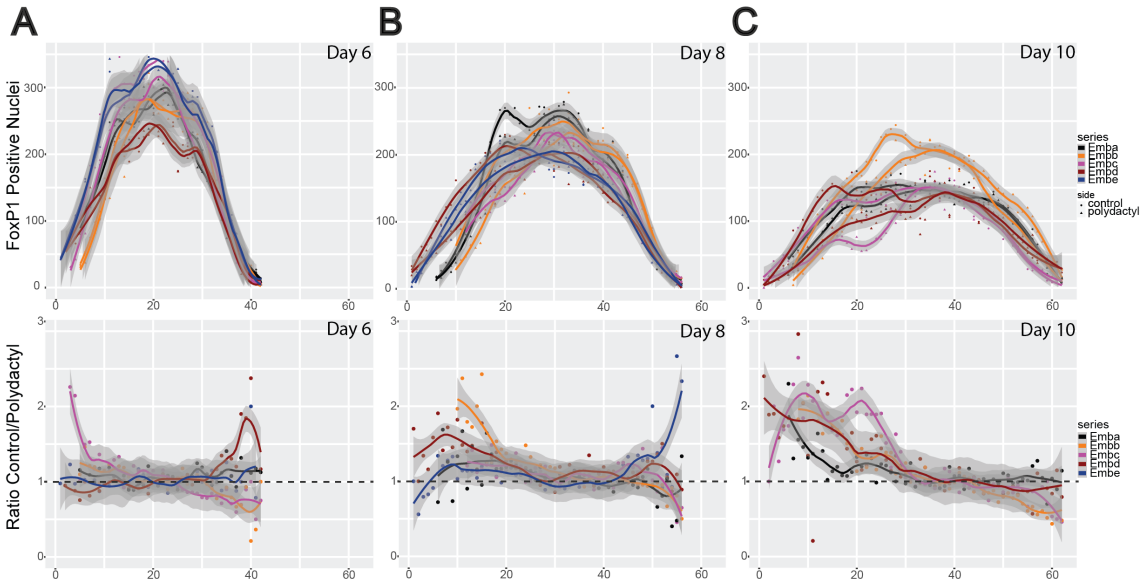

Figure S1: Motor neuron number in control and polydactyl chicken spinal cord
(A-C) The motor neuron number of each biological replica was plotted separately at each time point (top panel) and the ratio of control/polydactyl per replica was plotted (bottom panel).

Chapter 4

A method combining retrograde labelling and single-cell sequencing to study muscle-specific motoneuron transcriptomes

4.1 Abstract

The vertebrate spinal cord has long served as a paradigm to study cell-type specification. The prime example of cellular sub-differentiation is spinal motor neurons which first acquire motor neuron cell fate, then columnar fate, and later sub-divide into small subsets of so-called motor neuron pools. Motor neuron pools are spatially segregated from each other and their transcriptomic state directly dictates the unique gene expression modules needed to innervate one specific muscle. The study of motor neuron pool-specific transcriptomes with emulsion-based single-cell RNA-seq methods is difficult, as motor neurons are larger and fragile hence difficult to capture in the droplets. Also, gene expression differences between motor pools connected to different muscles are expected to be quite subtle, and thus a highly sensitive sequencing method is required to identify such dissimilarities.

In order to study the cell-specific transcriptional signature of a given motor neuron pool, we combined *ex-ovo* retrograde axonal labeling and tissue dissociation with manual cell selection based on fluorescence and single-cell sequencing using Smart-seq2. This sensitive method allows the detection of 8000-10000 genes per cell from the small starting material. We validate the method by injecting the wing EMR muscle and harvesting a total of 32 fluorescent cells. 80% of the cells presented a correct cDNA profile and 40% of them strongly expressed motor neuron markers.

Our method provides a unique approach to studying muscle-specific motor neuron pool differentiation and circuit formation at a single-cell resolution. Comparison of different

motor neuron pool transcriptomes can further our understanding of their molecular footprint according to their connectivity patterns to peripheral muscles.[1]

4.2 Introduction

During metazoan development, a multitude of various cell types needs to be specified to ensure the proper function of the body. As a prime example of their emergent cellular complexity, in most vertebrates, the central nervous system is composed of a high number of cell types, interconnected with each other and also with their target organs [121].

Limb innervating spinal motor neurons are particularly interesting in this context, as they go through a series of sub-specifications and their molecular footprint directly reflects their affinity for one single muscle [139, 187]. Indeed, they not only gain lateral motor column (LMC) identity at limb levels, but they also split into lateral and median LMC, to then subdivide into motor neuron pools. Motor neuron pools are spatially congregated, and transcriptionally unique sets of neurons innervating one particular muscle [147, 262, 289]. A few motor neuron pool-specific genes are known, however, our knowledge about the developmental onset and refinement of motoneuron pools is elusive.

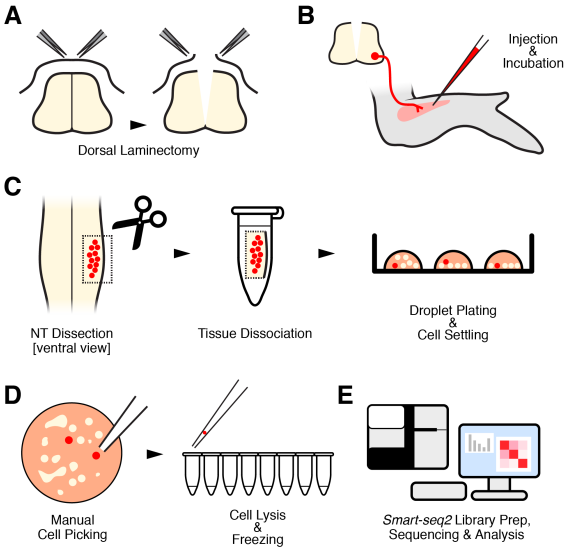

Figure 1: Overview of the workflow (A) First, dorsal laminectomy is performed to ensure the good oxygenation of the spinal neurons. That consists of detaching the dorsal part of the vertebra and cutting the roof plate. (B) Then fluorescent tracer molecule (CTB-555) is injected into the target muscle and embryos are incubated for 5 hours in ex-ovo culture until the fluorescent tracer is transported to the soma of spinal motor neurons. (C) After the culture, the neural tube is dissected, the success of the retrograde tracing is assessed under fluorescent binoculars and the fluorescent neural tissue is dissected and excised. Following Papain dissociation, the cells are resuspended and plated in Neurobasal media before manual purification. (D) After assembling the mouth pipette, healthy fluorescent cells are separated from debris and non-fluorescent cells by aspiration. Once the cells are washed in PBS, they are lysed in 2,3µl lysis buffer in a single well of a PCR strip. Lysed cells are kept at -80°C until further processing. (E) Smart-seq2 libraries are prepared, sequenced and the obtained sequences analyzed for new markers.

Since the commercialization of emulsion-based single-cell RNA-sequencing, many attempted to uncover and describe in detail neuronal subtypes during development and in adult individuals [272–274, 290]. However, the study of motor neuron pools is difficult with emulsion-based single-cell RNA-sequencing, as spatial information is lost during

[1]The final version of this chapter was published in Developmental Dynamics, see also A https://doi.org/10.1002/dvdy.507

dissociation, and capturing motor neurons can prove difficult (see Chapter 3). The need for a method that allows purification of single motor neurons from pools connected to a single muscle becomes paramount to studying this with appropriate resolution.

To study the direct link between target muscle and the position of neurons innervating it, retrograde axonal labelling has long been used [148, 149, 291]. It consists of injecting a tracer molecule into the target muscle and letting it be transported to the soma in the spinal cord. This method has been used to create topological maps of innervation in the chicken embryo. However, the number of labeled cell bodies is low and FACS sorting of those cells is not possible. Alternatively, laser-capture microscopy has been used to excise labeled cells from sections of the spinal cord, but that method is not providing single-cell resolution [157].

Here we present a workflow combining *ex-ovo* fluorescent retrograde axonal labeling with tissue dissociation and manual cell selection to obtain single motor neurons, attached to specific muscles, for sequencing. Our protocol provides details on optimal embryo culture conditions for mid-gestation chicken embryos, muscle injection, spinal cord dissociation, and manual purification of fluorescent cells from plated neurons for the highly sensitive Smart-seq2 method. To validate the method, we attempted to purify the motor neuron pool of the dorsally derived extensor metacarpi radialis (EMR) muscle in the chicken embryo. 80% of purified EMR cells displayed satisfying cDNA profiles and they were sequenced following Smart-seq2 protocols [292]. This sequencing method allows the detection of up to 12000 genes per cell, compared to previous emulsion-based efforts in our lab detecting only 3000 genes. The quality of the cellular transcriptomes was assessed by their level of mitochondrial (MT) genes, and we also inspected the expression of motor neuron markers in the purified cells.

Collectively, we present a method that provides transcriptomic data from specific embryonic motor neuron pools at a single cell resolution. Our technique opens new avenues to study the molecular signature of the forming motor neuron pools in mid-gestation and can help to elucidate the cross-talk between muscles and nerves at the early phases of the connection formed between the two.

4.3 Experimental procedures and results

4.3.1 Culture preparation

Heat DMEM/F-12 media (Thermo Fischer, no phenol red) to 37°C in a water bath. Connect the sandstone to the oxygen bottle and bubble it for 10 mins in autoclaved deionized water to clean it from dust and other residues (Figure 2B). Pour warm media into a silicone (SYLGARD™) coated 15cm Petri dish. This constitutes the culture dish for embryos. Place the Petri dish under a heating lamp, and use a thermometer to monitor and keep the temperature between 33-35°C. Once the sandstone is clean, place it in the media and bubble it thoroughly before the embryos are placed into it.

4.3.2 Embryo dissection and limb muscle injection

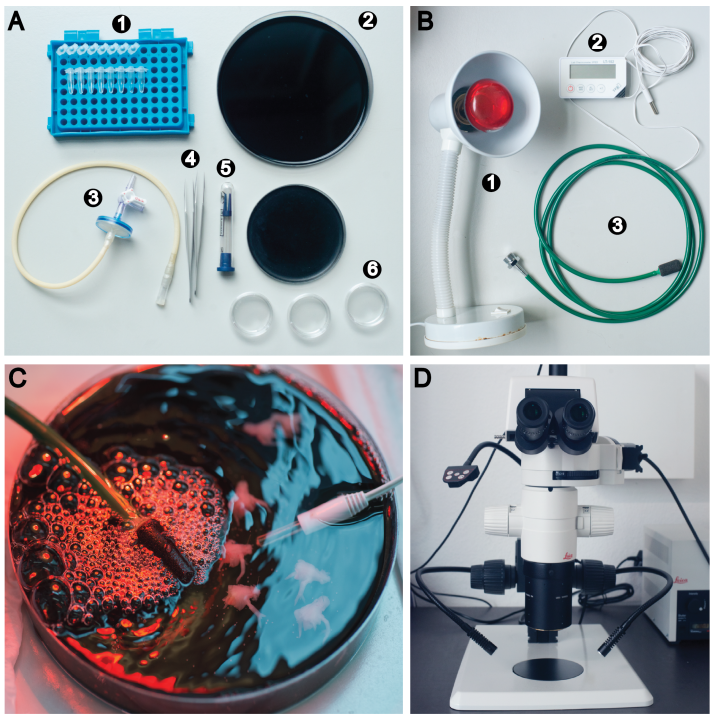

Figure 2: Tools and equipment (A) (1) PCR tubes, if possible, with individual lids (Eppendorf), (2) Two black Sylgard© coated 10cm and 15cm Petri dish, (3) Mouth pipette with a syringe filter and valve to control the airflow, (4) Dissection forceps (FST size 55), (5) Sterile micropipettes (ORIGIO MBB-FP-M-0) (6) Clean 6cm Petri dishes for PBS washes (B) (1) Heating lamp to maintain culture temperature, (2) Thermometer, (3) Sandstone connected to a plastic tube and screwed into the oxygen bottle (C) Image of embryos in culture. The sandstone provides oxygenation and the temperature is monitored during the incubation time. (D) Fluorescent binoculars (Leica, 1.6X ApoPlan objective) used for cell picking

White Leghorn chicken eggs (Gallus gallus) are incubated at 38°C with 60% humidity for 9 days before the experiment. Gently crack the egg and pour the content into a glass dish. Transfer the embryo into a PBS dish in order to wash all the yolk off, decapitate the embryo then put it into a black-silicone coated dish (Figure 2A). Ventral side down, pin the embryos to the dish by the neck and the tail. Make an incision at the middle of the back, approximately where the last ribs are connecting to the spine. Make sure that the entire spinal cord is cut through, then skin the back. In the late embryonic stages, it is important to ensure the oxygenation of the spinal neurons by performing dorsal laminectomy (Figure 1A). Using forceps, detach the dorsal part of the vertebra, starting from the caudal part up to the neck. Make sure that the underlying spinal cord remains intact. With a fire-sharpened Tungsten needle, cut the roof plate for better oxygenation of the ventral spinal neurons during incubation.

In this work, we demonstrate our method on the extensor metacarpi radialis (EMR), a dorsally located wing extensor muscle [238]. Once the dorsal laminectomy is performed, discard the lumbar part with the legs of the embryo. Pin the embryo on its side, for better visibility of the wing muscles. Gently skin the forearm without damaging the muscle bundles. Use a mouth pipette and pulled capillary to inject the fluorescent tracer molecule (CTB-555, 0,1mg/ml in PBS, Invitrogen) into the target muscle. Multiple injections are possible, all along the muscles. However, it is important to keep the muscle structure intact and avoid leakage of the tracer into other muscles (Figure 3B). After injection, place the embryos in the previously prepared culture dish and pin them down (Figure 2C). Monitor the temperature during the 5 hours of incubation and supplement the dish with fresh, heated media if needed.

4.3.3 Retrograde axonal labeling quality check

Once the incubation time is up, close the oxygen bottle and wash the sandstone in autoclaved water until the oxygen stops running. Pin the embryos face down to the dish so the spinal cord is visible. Gently pass closed forceps under the neural tube without damaging the neural tissue especially since the motor neurons are in the ventral horn of the spinal cord. Pin down the neural tube, ventral side up, for inspection.

Place the dish under binoculars equipped with fluorescent lamps and adequate filters (Figure 2D). In case the axonal tracing was successful, a fluorescent signal is visible at this stage in the ventral horn of the spinal cord (Figure 3A). Under the scope, dissect the fluorescent part of the neural tube (Figure 3A-A') and place it in an appropriately labeled tube with PBS. Wash the dissected tissue twice with PBS, to eliminate all residues present in the culture media as it might alter the efficiency of the tissue dissociation. Dissect the injected limb, fix in PFA 4% (Sigma) overnight and preserve in PBS at 4°C until injection quality inspection.

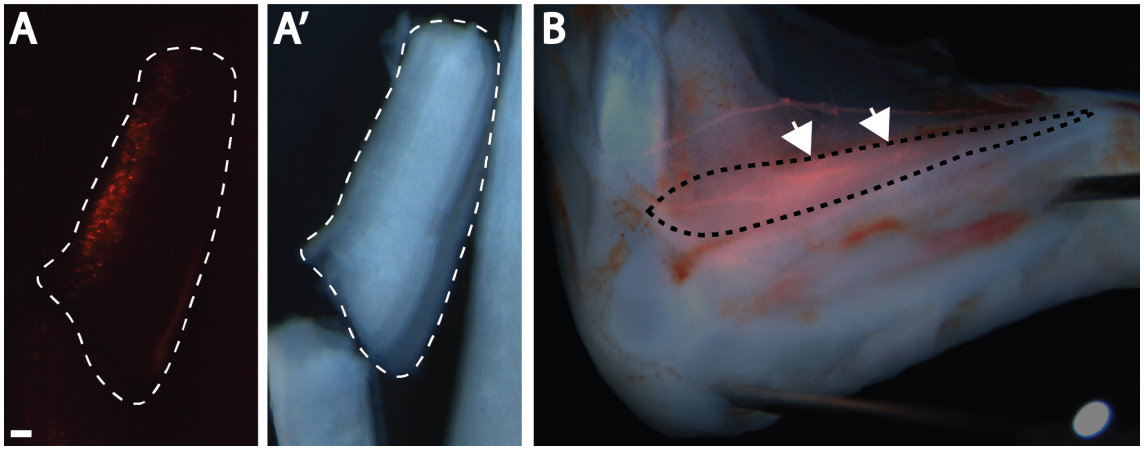

Figure 3: Retrograde labeling and muscle injection quality check (A) Whole mount image of the fluorescent signal in the ventral side of the neural tube after retrograde axonal tracing in the neural tube. A white dotted line represents the limits of the neural tube (A') Brightfield image of the dissected fluorescent region (B) Injection site in the EMR muscle. Black dotted lines show the extent of the muscle and white arrows show the injection sites. Scale bar represents 100µm.

4.3.4 Dissociation and cell plating

Neurons and neural tissue are sensitive to dissociation, especially after a long ex-ovo incubation period. Therefore, a mild Papain dissociation method is more suitable and cells should be plated in a neuron-specific media (Plating media: Neurobasal™ Gibco, 5% FBS and 1% GlutaMAX™ Gibco [293]). Put the Plating Media in a Petri dish in a cell culture incubator for CO2 equilibration for an hour and a half, before the end of the axonal tracing.

Half an hour before the end of the incubation, mix FACSmax (Amsbio) dissociation media with Papain (Roche) to get a 0,25 mg/ml concentration of the enzyme. Heat the mix to 37°C in a water bath until the neural tube is dissected. For tissue trituration, use a p1000

pipette and prepare for each sample the following tips: 1) Cut one tip close to the 250 µl line, 2) cut a second one halfway between the 250 µl line, and the pipette tip and burn both to eliminate sharp edges. Prepare two additional uncut tips for further trituration, spray them with ethanol and place them under the cell culture hood. Once the desired neural tissue is dissected, discard the PBS, add 1ml of dissociation media to each sample, and put it in a water bath at 37°C for 10 min. Flick the tubes gently after 5 minutes. Triturate with the first cut pipet tips 20 times, then place back the sample at 37°C for an additional 5 minutes. Repeat the last step, with the second cut and uncut pipette tips until no visible tissue clumps are present.

Centrifuge the samples at 300g for 7 minutes at room temperature, discard the supernatant and resuspend the cells in 700µL of Plating Media. The dissociation only gives a small number of cells (around 310000 cells/ml with 90% viability) hence plating drops of cell suspensions in a bigger Petri dish provide a higher concentration of cells at a smaller surface. This facilitates the detection and manual purification of fluorescent cells. In a 10 cm Petri dish, deposit the cell suspension forming drops of approximately 150µL, then place it in a cell culture incubator for at least 30 minutes, so cells have time to settle in the bottom of the drops (Figure 4A).

4.3.5 Manual cell purification

First, prepare the workspace for cell selection by spraying RNAseZap (Invitrogen) on the surfaces, pipettes, and binoculars, then wipe them clean. As the Plating Media contains FBS, picked cells must be washed at least twice in clean cold PBS before being deposited into the lysis buffer as FBS might alter the results of sequencing. Prepare three, three-centimeter Petri dishes right before proceeding with the cell picking. Fill the dishes and the lids with ice-cold PBS. Use one Petri dish to fill the capillary with clean PBS, the second one to eject any liquid between picked cells, and the third one to quickly wash the needle (Figure 2A). Wash the cells in the PBS-filled lids as it is shallower and easier to pass from one to the other.

In this method demonstration, we are preparing cells for Smart-seq2 single cells sequencing, hence we are using a cell lysis buffer compatible with the workflow (0.2% (vol/vol) Triton X-100 and 2 U µl–1 RNase inhibitor, [292]). Label PCR strips, deposit 2.3µL of lysis buffer in each well, and keep the buffer cooled before and during the experiment, if possible, in a metal cooling rack on ice. Assemble the specific cell aspirator (3-way stopcock, 0,3µm syringe filter, cell aspirator tube, sterile micropipette (Origio, MBB-FP-M-0), and make sure that all the seals are tight. If leakage of air is observed, use paraffin sheets and change the filter if needed (Figure 2A). Put the sterile capillary at the end of the cell aspirator and quickly check with PBS if there are no leaks of air and the liquid is properly entering the capillary.

Observe the drops of cell suspension under the fluorescent microscope and estimate the total number of fluorescent cells. Take up clean PBS into the needle to avoid capillary

action and have total control over the suction. Aspire the target cell. At this stage, it is probably not possible to aspire the cell alone. Take a PBS-filled Petri dish lid, adjust the focus of the binoculars and gently eject the content of the needle. Make sure that the process is slow otherwise the cells might start floating out of the field of vision. Turn off the light and check if the fluorescent cell is present. Wash the capillary needle, then re-aspire the neuron with as few other cells as possible. Repeat the previous step and blow clean PBS around the CTB positive cell, to wash away all other cells and debris from its surrounding. Wash the capillary with PBS again, aspire the target cell and deposit it into the lysis buffer. Note down any observations about the cell, its shape, relative size to other cells, and fluorescence intensity. Repeat the process until there are no fluorescent cells left in the drops. Deposit the PCR strips at -80°C until library preparation and sequencing.

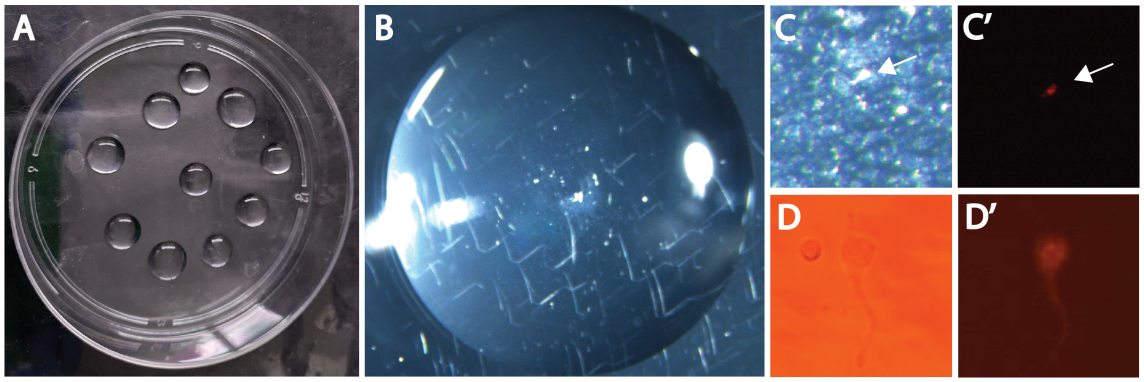

Figure 4: Manual isolation of single neurons (A) Post-dissociation cell suspension is plated in drops to maximize cell concentration in the middle of the drop. It facilitates the screening of the plate and the cell picking process, as most of the cells are in the middle of the drops. (B) Close-up image of a 150µl drop of cell suspension. (C and C') Brightfield and fluorescent image of a red fluorescent plated cell. Note the concentration of cells and debris at this first stage of cell picking. (D and D') Image of one isolated cell (after multiple PBS wash) taken with a fluorescent microscope for better visualization (30X).

4.3.6 Library preparation, sequencing and representative results

After reverse transcription (Superscript II) and amplification, cDNA samples are processed in a Fragment Analyser for quality check. We analyzed each cDNA profile to evaluate possible sampling errors and RNA degradation. The signs of good quality cDNA profiles for full-length RNA-seq cDNA are a high peak between 1,5-2kb (full-length transcripts) and a small number of fragments below 500bp, as well as a small peak of primer dimers (100bp) (Figure 5A). We fitted each cDNA profile into one of three quality categories: 1) good (Figure 5A top panel); 2) medium, where the highest peak is at the correct size, but lower and the peak is broader at the base, a sign of possible partial RNA degradation (Figure 5A middle panel); 3) low, as no peak of transcripts is visible at the 1.5-2kb size (Figure 5A bottom panel). From a total of 32 harvested cells (from 3 independent embryos) 26 had a satisfying cDNA profile (81%). Sequencing libraries were prepared with Illumina Nextera XT kit and all samples were sequenced on an SP flowcell (50 bp, pair-end) on a NovaSeq 6000 machine (Illumina).

The raw reads were then trimmed with Trimmomatic (v.0.39), using the Illuminaclip parameter with the distributed Nextera adapter file, aligned with STAR (v.2.5.2) to the GRCg6a chicken genome, and count tables were created with HTSeq (v.0.6.1).

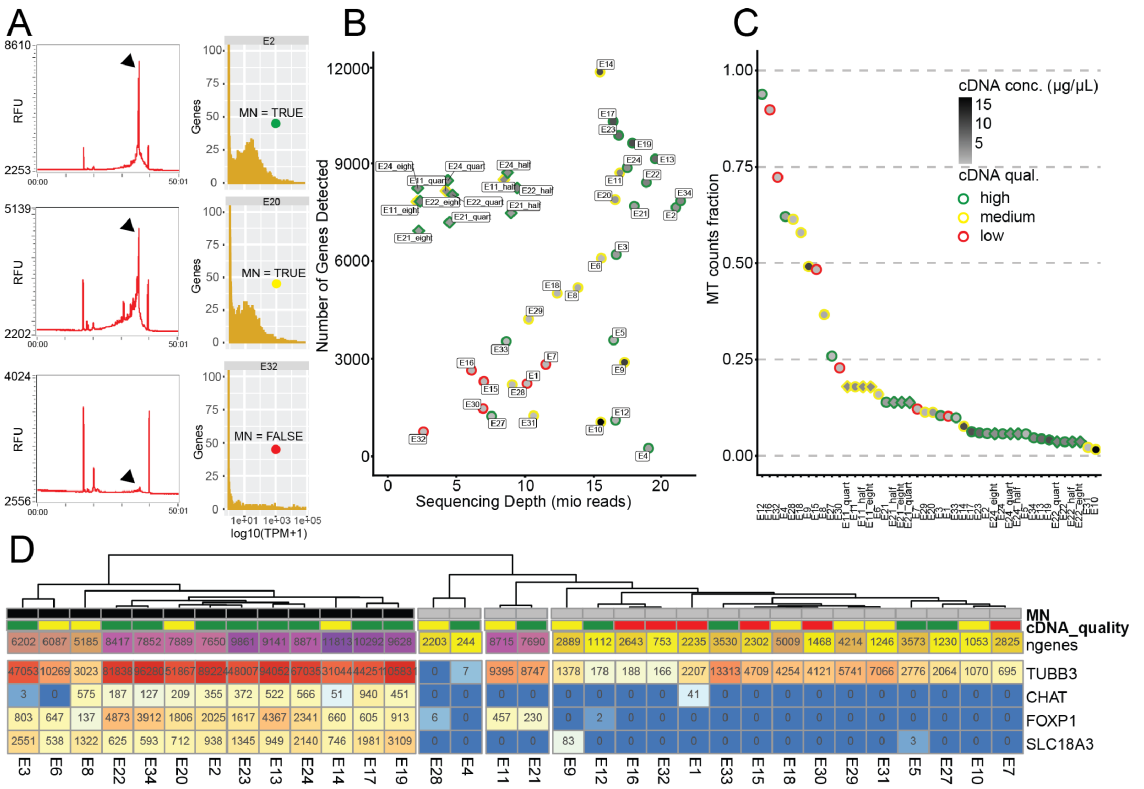

Figure 5: Representative results of single neuron sequencing (A) cDNA profiles of three samples with different library qualities good, medium, low) and histograms of their log10(TPM+1) expression. (B) Dot plot of sequencing depth (number of raw reads) vs number of genes detected per cell. The color gradient represents cDNA concentration. Colored circles highlight the quality of cDNA. Diamonds indicate the 4 downsampled cells (half, quarter, and eighth of the total reads). (C) Cells are ordered by the mitochondrial fraction of expression. Colored circles indicate cDNA quality (green: high, yellow: medium, red: low). (D) Heatmap of transcript number of *TUBB3, CHAT, SLC18A3* (vacuolar *CHAT*), and *FOXP1* genes. Cells are grouped by hierarchical clustering.

We inspected the number of detected genes in the function of the sequencing depth and the mitochondrial fraction of all detected transcripts per cell (Figures 5B and C). The Smart-seq method can detect up to 10000 different genes, in contrast to the emulsion-based methods where this number is around 2-3000 genes [294]. Most cells with a good cDNA profile and a high cDNA concentration contained a high number of genes as shown in Figure 5B. Cells with a good profile, but with low cDNA concentration (0.8 µg/µl) show lower gene count (such as E5, E27, and E33). A group of cells (E9, E12, E4) showed low gene count despite a good/medium cDNA profile and very deep sequencing (between 15-20 million reads per cell). This can be explained by their high mitochondrial gene expression (Figure 5C) as the mitochondrial transcriptome is less complex hence the low gene number. A high mitochondrial fraction in the transcriptome reflects the fitness of the cells and it is fair to assume that these cells were dying when picked from the plate. Lastly, in the case of cell E10, only 2% of the reads mapped to the

genome due to a short read length reflects a technical issue during library preparation or sequencing.

To test for sequencing saturation, we downsampled 4 cells with high sequencing depth and a high number of genes detected (Figure 5B, E11, E21, E22, and E24). For the down-sampled cells, Seqtk (v.1.2) was used to randomly sample half, a quarter, and an eighth of the reads from the respective .fastq files. Then those subsets were processed with the same pipeline as described above. Gene abundance and count tables were imported into R (v.4.0.3) for further analysis (Figure 5B, diamond shapes). The result showed that even in the most drastic case of downsampling (from 17 mio to 2 mio reads), the number of genes detected did not decrease substantially. This insinuates that a two million reads sequencing depth is sufficient for cells with a good cDNA profile and high cDNA concentration to saturate gene detection and cut sequencing costs.

In order to validate the identity of cells as motor neurons, a number of marker gene expression profiles were examined (Figure 5D). Almost all cells (except 2) expressed the general neuron marker *TUBB3* (*TUJ*1). However, cells of the first cluster have a higher transcript count for *TUBB3* and an overall higher number of a gene detected than the other three clusters. 13 cells out of 32 expressed Choline Acetyltransferase (*CHAT*) and Vesicular Acetylcholine Transporter (*SLC18A3*), two members of the biosynthesis and transport of Acetylcholine neurotransmitter, only found in motor neurons. Furthermore, those cells expressed *FOXP1*, the embryonic motor neuron marker gene [140] (first cluster Figure 5D).

To summarize, the following criteria have to be taken into account when deciding which cells to include cells for further analysis, such as a comparison between motor neuron pools: 1) high cDNA concentration (>5 µg/µl) with a cDNA profile peak at size 1.5-2kb; 2) less than 50% of mitochondrial gene transcripts per cells; 3) more than 4000 genes detected in the cell; 4) positive for expression of motor neuron markers. Samples meeting all of these criteria can provide robust and reliable information. Samples meeting some of the criteria have to be considered on a case-by-case basis, to determine whether their inclusion in further work is reasonable.

4.3.7 Discussion and conclusion

Our hereby presented method successfully combined together the classical embryonic technique of retrograde axonal tracing with modern single-cell RNA-sequencing in order to study motor neuron pool-specific transcriptomes at a single-cell resolution. This procedure proved itself efficient in detecting marker genes and could be used to compare different motoneuron pools innervating various muscles.

Ex-ovo manipulation and culture of chicken embryos require the optimization of various conditions. The retrograde axonal labeling is influenced by multiple factors, such as the age of the embryo, the size of the muscle, and its position in the proximo-distal axis. Later stage embryos (after HH35, day 9) are more difficult to culture due to their size and the

formation of thick skin and cartilage. Previously described ex-ovo retrograde labeling methods are using the more difficult ventral laminectomy that involves the evisceration of the embryo and the detachment of the ventral part of the vertebra [149].

As this procedure ensures better oxygenation of the ventral horn, motor neuron survival and successful axonal tracing are more likely, yet the manipulation is more delicate. Smaller and more distal muscles (such as autopod/hand muscles) are not only difficult to properly inject because of their size, but also the retrograde transport becomes less reliable and fails more often. The number of fluorescently labeled cells is also decreasing with the size of the muscle and more experiments are needed in order to harvest enough cells for a robust dataset. In our dataset, 40% of all cells were identified as motor neurons based on the cholinergic pathway-related gene expression. The other 60% of samples did not meet one (4 cells do not express motor neuron markers) or multiple of our quality criteria (15 cells) listed above. These percentages have to be taken into account in the experimental design when determining the number of cells to be purified using this protocol.

This tool, combined with simultaneous sequencing of the target muscle, has the potential to shed light on the motor neuron-muscle connectivity by unveiling ligand-receptor interactions, and neurotrophic factors specific to them and lead to a better understanding of the communication between the motor neuron pool and target muscle during the onset and development of their connection.

4.4 Contribution

All steps of the technique were established and optimized by the author. Sequencing was carried out in the D-BSSE Genomics Facility Basel, ETH Zürich. Bioinformatic analysis and plots were realized by Fabio Sacher. The artwork in Figure 1 was made by Patrick Tschopp.

Chapter 5

Future direction of the project

In Chapter 2, we documented the patterning changes of muscle and nerve projections in the periphery of polydactyl embryos. In Chapter 3, we inspected how the motor neuron numbers are affected by polydactyly, and how different molecular aspects of duplicated muscles might affect the efficiency of innervation and motor neuron survival. Our effort to compare spinal motor neuron pools between control and polydactyl individuals by scRNA-seq was only partially fruitful, due to the difficulty to capture a high number of motor neurons with emulsion-based methods. Therefore, a different, more direct approach was needed in order to gain insight into the transcriptional state of motor neurons at a single-cell resolution. To this end, the method described in Chapter 4 was developed and optimized.

The idea behind developing such a technique was specifically to trace back motor neuron pools innervating 'normal' and duplicated muscles in the autopod of polydactyl chicken limbs (Figure 1). Our attention was particularly focused on the ventral muscles FDQ and FDQ', as the nerve innervating the FDQ' is an ectopic projection of the median nerve, instead of the usual ulnar nerve, as the median nerve gets split upon induction of a polydactyl wing. These pattern changes imply a change in motor circuit formation and potentially a motor neuron subtype identity modification in the context of the polydactyl wing. Hence, we decided to use fluorescent retrograde axonal labeling to trace the motor neuron pools connecting to 'native' muscles, such as FDQ, and their duplicated counterpart, such as FDQ', and isolate fluorescent cells and sequence their transcriptomes. We plan to compare the motoneuron transcriptomes of FDQ and FDQ' to motor neurons connected

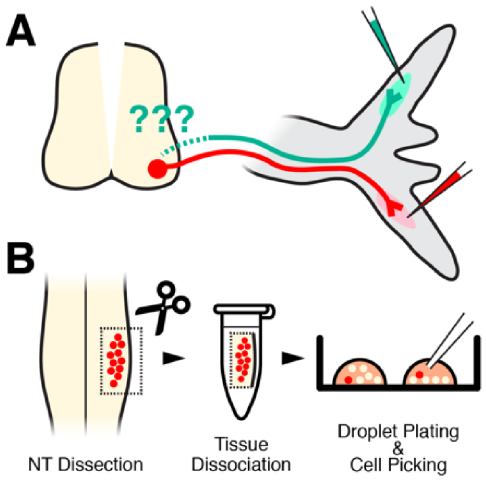

Figure 1: Workflow in polydactyl chicken embryos (A) Retrograde axonal labeling of 'native' and polydactyl muscles followed at embryonic day 9. (B) Manual cell purification of motor neurons, see 4

to the AM and duplicated AM' muscles. There, both control and polydactyl muscles are connected to the median nerve (Chapter 2, Figure 5). Therefore, we hypothesized that probing these motor neuron pools alongside FDQ and FDQ' pools would allow us to discriminate between changes induced by muscle duplication, versus changes induced by connecting to an ectopic muscle.

Maturation of motor neuron pools is known to be dependent on a muscle-nerve cross-talk at the synaptic sites. For example, neurotrophic factors play a key role in the consolidation and survival of individual neurons upon connection and induce transcriptional changes in their somas located in the spinal cord [185–187, 295–297]. To get insight into the panel of genes expressed by the target muscles in polydactyl limbs, we also sequenced dissected muscles, in an attempt to find putative ligand-receptor couples and new candidates potentially playing a role in the nerve-muscle connection.

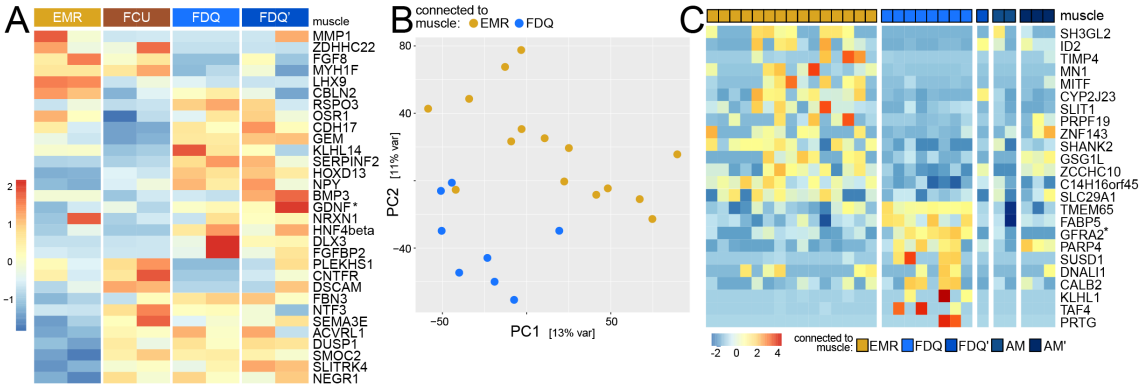

Figure 2: Communication between muscles and the corresponding motor neuron pools in polydactyl limb 1(A) Heatmap of highly expressed genes in bulk RNA-seq data of different muscles in the chicken wing. The EMR and FCU are dorsal anterior and posterior zeugopod muscles respectively, FDQ' is the duplicated form of FDQ in the ventral autopod of polydactyl embryos. (B) PCA analysis of motor neurons innervating EMR or FDQ muscles. The cells coming from two different motor neuron pools do not intermingle, reinforcing that motor neuron pools are transcriptionally distinct. (C) Genes expressed in individual neurons.

Preliminary sequencing data were obtained for both muscle-specific, retrogradely labeled motor neurons, as well as control and duplicated whole muscles (Figure 2A). However, several technical difficulties hindered the smooth advancement of this task: the retrograde axonal labeling was optimized on the zeugopod EMR muscle, which is bigger and dorsally positioned, and hence easier to access, manipulate and inject. The injection of the small ventrally positioned FDQ and FDQ' proved itself to be much more challenging. Moreover, the tracer molecule has a long trajectory from the autopod to the central nervous system and the process becomes less robust, with fewer motor neurons being stained. Similar tendencies were observed for AM and AM' muscle tracing, which are ventrally positioned as well.

Despite these difficulties, we managed to obtain eight neurons from the FDQ pool, one from the FDQ' pool, two from the AM pool, three from the AM' pool, and 15 from EMR pool (see results of Chapter 4). Notably, in the PCA analysis performed with

EMR and FDQ motor neurons, cells from one or the other did cluster apart, indicating clear differences in the transcriptomic state between the two (Figure 2B). Differentially expressed gene analysis performed between motor neuron pools innervating EMR or FDQ provided us with potential genes to study and consider for future functional analysis, to elucidate the molecular determinants of muscle-specificity in motor neuron pools (Figure 3C).

As for the muscles, duplicates of FDQ, FDQ', and EMR muscles were sequenced (bulk-RNA) as well as the FCU – a posterior dorsal muscle in the zeugopod – although we do not yet have motor neuron pool data for it. At the time of writing this manuscript, we have no sequencing data from the AM and AM' muscles, but efforts to do so are ongoing.

Differentially expressed gene analysis was performed among the different muscle transcriptomes (Figure 2A). As a first observation, muscles seem to have a specific molecular footprint according to their antero-posterior, dorso-ventral, and proximo-distal positions. FDQ and its duplicated counterpart show very similar gene expression patterns. This suggests the mirror-image duplication in also a molecular identity sense, even though we demonstrated that FDQ and FDQ' muscles can differ in muscle-fiber composition (Chapter 3, Figure2). Both also express *HOXD13*, a hallmark of autopod identity [298]. Both FDQ and FDQ' express Glial Cell Derived Neurotrophic Factor (*GDNF*) and the FDQ motor neuron pool expresses its co-receptor *GFRA2* (Figure 2C). Also, both muscles express Neurotrophin 3 (*NTF3*), another neurotrophic factor shown to be implicated in motor neuron survival. Combinatorial effect of neurotrophic factors in order to selectively promote certain motor neuron pool survival has been shown in cultured spinal neurons, and it is, therefore, possible that *NTF3* and *GDNF* act simultaneously to 'attract' appropriate motor nerves [299]. FCU muscle also expresses *NTF3*, however, no neurotrophic factor expression was found specifically in the differentially expressed genes of the EMR muscle. Moreover, the differentially expressed genes of the EMR innervating motor neuron pool did not present any known receptors for neurotrophic factors.

To elucidate the molecular cross-talk between muscles and nerves during development, and understand how this sensitive system changes in response to polydactyly, it is important to include more muscles (such as AM and AM') and more replicates of already sequenced muscles. Even more importantly, obtaining a higher number of motor neurons from the various motor neuron pool is key to building a robust dataset to match the information gained from muscle sequences. Although gene expression patterns and functions remain to be validated in vivo, our investigation brings us closer to understanding how neurons and muscles develop together and form functional units during development. Importantly, we already present preliminary data suggesting muscle-neuron pair-specific expression patterns of neurotrophic factors and their receptors.

Chapter 6

General discussion and conclusion

Coordinated muscle movement orchestrated by motor neuron activity is key for all movement [300]. Terrestrial locomotion of tetrapods, and the changes in the distal limb structure that paved the way for it, demanded a more elaborate and complex neuromuscular system in the limb [9, 301]. Along the proximo-distal axis, the limb can be divided into three segments: stylopod (humerus/femur), zeugopod (radius-ulna/tibia-fibula) and autopod (carpals, metacarpals and digits) [302]. The stylopod and zeugopod ensure rotation and mobility, the autopod is important for better distribution of the body weight on solid support, and the fingers - first used for better traction - can eventually become tool for fine motor tasks such as grabbing. The proximal stylopod and zeugopod only went through minor morphological changes, while the distal autopod shows incredible diversification in extinct and extant tetrapods [303, 304]. Number of phalanges and number of digits varied largely throughout evolution [212–214]. In extant tetrapods, five digits seems to be the upper limit of fingers, except in pathological conditions, called polydactylys, where this limit is surpassed [30, 305]. On the other hand, fossil data show multiple polydactylous ancestors in the stem-tetrapod group and the five-digit or less formula was established in the crown-group of tetrapods (Introduction, Figure 1) [26, 30].

When an anatomical structure is modified, often it is through changes in the regulation of the underlying developmental mechanisms of the trait [34]. A functional limb requires a support system in the form of the skeleton. However, the musculature that generates force by contraction, and a control system in the form of the nervous system are equally important [306]. While previous studies mainly focused on the skeletal patterning in polydactyly during development, the work presented in this thesis emphasized how the neuromuscular system responds to changes in digit numbers [71, 73, 307].

6.1 Special neuroanatomical features of the chicken limbs

As a first step in exploring the development of the neuromuscular system in chicken limbs, we established a 3D time series of nerves and muscle patterning in wings and legs (Chapter 2). While analyzing the nerve branch behavior we realized that the median and the ulnar nerve, as well as the lateral and median fibular nerves, form an arch-like

structure in the wing and leg, respectively. These nerve branches start their growth as individual nerves, but join together at the border of the forming autopod and project further nerve branches to the muscles of the hand and feet.

A comparative study of the available published data and work conducted in our lab showed that this arch formation seems to be specific to sauropsid models and absent in other investigated species such as humans, mice, or Axolotl [**Luxey et al., unpublished data**, 217, 308]. The function of such a neuroanatomical structure is unknown. One possibility is that the arch serves as a scaffold, to stabilize the nerve branches before the invasion of the autopod region. Interestingly, in the polydactyl leg, an ectopic anterior nerve branch appears and joins the plantar nerve to form an arch (Chapter 1, Figure 3). Our staining method (neurofilament) doesn't allow us to discriminate if the newly emerging nerve is indeed a motor nerve or sensory, but this arch formation seems to be a recurring phenotype in the chicken model. Further studies are needed to find molecular actors involved in the arch formation. Also, it is unclear whether axons from one nerve branch might be able to pass to the other side of the limb, through the arch structure. Theoretically, if we were able to label neurons in the spinal cord and follow their projections one-by-one in the nerve branches, we could observe axons passing or not from anterior to posterior. For such, single axon labeling, the Brainbow method proved itself a powerful tool. Briefly, Brainbow is a method based on the Cre-lox recombination system that creates the expression of a different combination of fluorescent proteins in each cell, hence most cells can be distinguished from their neighbors by color [309–312]. In the chicken model, co-electroporation of plasmids containing the fluorescent proteins and a plasmid containing the Cre enzyme proved itself a powerful tool [311].

Electroporation into the brachial and lumbar LMC, together with tracking of individual axons through the limb until the arch, might unveil the axonal structure of the arching nerve branches.

6.2 Axon guidance and vasculature modification in polydactyly

With our 3D reconstruction of control and polydactyl chicken wings, we also showed a differential response of the musculature and nerve projections to polydactyly [258]. Briefly, muscles in the autopod follow the mirror-image duplication, but the nerve branches exhibit a different response. Namely, the posteriorly positioned dorsal and ventral nerves, the median and the radial respectively, split into two branches and project into the extra-digit territory (Chapter 2, Figure.3, Figure S5). The nerves are redirected toward the polydactyl compartment by the limb mesenchyme.

Axons and nerves as a whole are often confronted with so-called "choice points" where they have to make decisions about their future trajectory, based on axon guidance molecules available in their environment, and the receptors present on their growth cones. Two well-studied models of such "choice-points" are the midline crossing of

commissural neurons in the spinal cord and the dorso-ventral split of limb innervating nerves [174, 208, 313, 314]. However, little is known about how nerves split in the anterior-posterior axis more distally in the limb, and which molecules drive digit-specific innervation patterns.

Efforts in our laboratory attempt to unveil the axon guidance cues present or absent in the 'native' or extra-digit territory, and at the border of the two in the autopod mesenchyme. To this aim, polydactyl autopods were dissected into 4 territories on day 6 of development, native and polydactyl sides were divided into two (anterior and posterior territory) and then sequenced [**Pumo**, **Luxey et al.**, **unpublished data**]. Candidate genes were selected by the Gene Ontology term 'Axon guidance', and genes present specifically in one compartment, but not in the other three were retained. The expression pattern of these genes was inspected by in situ hybridization on control and polydactyl limbs on day 6 and day 7 of development. Surprisingly, molecules such as *SEMA3A* and *EFNA5* were expressed only in the posterior part of the 'native' digits while the molecule *SEMA3E* at the border between 'native' and polydactyl compartment [**Pumo**, **Luxey et al.**, **unpublished data**]. All three molecules are known to be mainly repulsive for axon growth cones competent to respond to these signals [168, 169, 315–318]. These results further underline that the mirror image duplication of the skeleton does not automatically reflect a mirror-image duplication of gene expression in the mesenchyme, or factors influencing the cellular composition of the muscles see (Chapter 3, Figure 2). Although potentially many other molecules play a role in the complex pathfinding in polydactyly, *SEMA3A* and *EFNA5* could repel the median nerve in a control condition, while creating a permissive environment for the ulnar nerve to grow. The repulsive signals are not present in the polydactyl compartment and there might be other molecules present that attract the median nerve to that area. Also, the spot of SEMA3E at the border might represent the 'choice-point' for the median to split.

In order to prove that those molecules expressed in the mesenchyme play a pivotal role in the onset of the nerve branch pathfinding, the method described in Chapter 4 could be used on earlier stage polydactyl embryos, when the axon guidance and pathfinding of the nerves are ongoing (day 5 to day 7). As the molecular actors of axon guidance in the mesenchyme have been described in the work above, our method of axonal tracing coupled to single neuron RNA-sequencing could provide the neuronal component to it and establish ligand-receptor pairs crucial for the proper axon guidance of each main nerve branch.

Interestingly, similar modifications of nerve-branch patterning presented in chickens were observed in human patients with mirror-image duplication of digits (referred to as mirror hand) [230]. Furthermore, medical reports of patients with severe complex polydactyly describe accompanying defects in the vascular system, such as duplication of the ulnar artery and abnormal arterial arches in the hands of the affected limbs [319]. The link between nerve projections and vasculature formation has been shown in the skin of mouse limbs [320–322]. Indeed, peripheral nerve-derived CXCL12 and

VEGF seem to play an important role in vasculature patterning in the limb [320, 321]. Although we mainly focused on nerves connecting to muscles in our study, the polydactyl compartment of the wing and leg was rich in sensory innervation. Studying the vasculature could be a valuable addition, in order to deciphering how the major modifications in nerve patterning affect blood vessel formation.

Together, a better understanding of the molecular mechanism of axon guidance, nerve branching, and vasculature formation in the chicken polydactyl model provides us with valuable information about the onset of complex human limb pathologies.

6.3 Effect of polydactyly on the proximal limb

Polydactyly is often thought about as an exclusive anomaly exclusively affecting the hands and feet. Likewise, our work also heavily focused on the development of the neuromuscular system of the distal parts of the wing and leg. Medical classification of polydactyly is based on the modification of the skeleton of the wrist, metacarpals, digit, and phalange number [305]. However, previous studies on polydactyl models and human patients showed that bone morphology and musculature of the zeugopod can also be heavily affected. Polydactyly is often accompanied by deficiencies in the zeugopod called radial ray deficiencies, such as radial aplasia (absence of the radius bone), radial hypoplasia (decrease in size of the radius) or ulnar dimelia (duplication of the ulnar bone and absence of the radial bone) [230, 319, 323–326]. As for the musculature, while the antero-posterior patterning is impaired, certain muscles are missing due to the perturbed signaling in the limb while other muscles are duplicated [101, 230]. Our work provided evidence that those changes in muscle patterning were also accompanied by changes in muscle fiber type. More strikingly, however, the innervation is heavily affected and the spinal motor neuron numbers are seriously reduced (Chapter 3, Figures 1 and 2).

Hand surgeons are also considering unifying polydactyly and radial ray deficiencies into a common classification, especially since experimental data show that the two types of pathologies share common developmental origins [327–330]. Our results support these views and a wider classification is needed to encompass the bone structure of polydactyl individuals, the potential radial ray deficiencies and the soft tissue modifications going along with those bone structure variations.

In order to achieve this goal, we need more information about the neuromuscular system in patients and in further animal models, such as polydactyl mice and chicken, like the 'extra-toes' and Silkie breed respectively, and incorporate clinical and developmental data to obtain an integrated view on the pathology of the extremities.

6.4 Concluding remarks

Altogether in this thesis, I present a detailed description of the development of the neuromuscular system in a normal and polydactylous chicken wing and legs at a high resolution in 3D. I described unusual, sauropsid-specific neuroanatomical structures, such as nerve-arch formation and 180° rotation of the nerve branch patterns between the wing and the leg. This descriptive work should prove a highly valuable resource for comparative anatomy studies between different taxa, and formed the basis for the ensuing chapters of my thesis. Then, I showed how polydactyly can alter nerve branching, muscle patterning, and muscle fiber composition in the limb. Also, I observed how motor neuron survival is affected by polydactyly, and used single-cell RNA-sequencing to describe the cellular composition of the spinal cord in polydactyly.

In the last chapter, in an effort to understand how polydactyly affects muscle-specific motor neuron pool identity, I developed a method that combines the classic retrograde axonal labeling with modern single-cell RNA-sequencing. By learning about the transcriptomes of muscle-specific motor neurons, we can gain insight into how the presence of ectopic muscles is assimilated by the motor neuron pools.

During limb development, multiple tissues, namely the skeleton, the muscles, and nerves, have to be patterned simultaneously and they have to interact and communicate with each other in order to form a functional appendage. When the skeletal pattern is changed, the neuromuscular system has to change accordingly, assimilating the alterations in the bone structure. My work shows the importance of adopting an integrative approach when studying the formation of a complex structure, such as the limb, especially in the context of a complex condition such as polydactyly in order to fully understand the onset of such pathologies.

Appendix A

Published Content

Developmental Biology 458 (2020) 133–140

Contents lists available at ScienceDirect

Developmental Biology

journal homepage: www.elsevier.com/locate/developmentalbiology

Development of the chick wing and leg neuromuscular systems and their plasticity in response to changes in digit numbers

Maëva Luxey [a,1], Bianka Berki [a,1], Wolf Heusermann [b], Sabrina Fischer [a], Patrick Tschopp [a,*]

[a] DUW Zoology, University of Basel, Vesalgasse 1, CH-4051, Basel, Switzerland
[b] IMCF Biozentrum, University of Basel, Basel, Switzerland

ARTICLE INFO

Keywords:
Limb musculoskeletal apparatus
Autopod evolution
Limb neuromuscular 3D-atlas
Light-sheet microscopy
Polydactyly
Forelimb/hindlimb differences

ABSTRACT

The tetrapod limb has long served as a paradigm to study vertebrate pattern formation. During limb morphogenesis, a number of distinct tissue types are patterned and subsequently must be integrated to form coherent functional units. For example, the musculoskeletal apparatus of the limb requires the coordinated development of the skeletal elements, connective tissues, muscles and nerves. Here, using light-sheet microscopy and 3D-reconstructions, we concomitantly follow the developmental emergence of nerve and muscle patterns in chicken wings and legs, two appendages with highly specialized locomotor outputs. Despite a comparable flexor/extensor-arrangement of their embryonic muscles, wings and legs show a rotated innervation pattern for their three main motor nerve branches. To test the functional implications of these distinct neuromuscular topologies, we challenge their ability to adapt and connect to an experimentally altered skeletal pattern in the distal limb, the autopod. Our results show that, unlike autopod muscle groups, motor nerves are unable to fully adjust to a changed peripheral organisation, potentially constrained by their original projection routes. As the autopod has undergone substantial morphological diversifications over the course of tetrapod evolution, our results have implications for the coordinated modification of the distal limb musculoskeletal apparatus, as well as for our understanding of the varying degrees of motor functionality associated with human hand and foot malformations.

1. Introduction

During vertebrate limb development, growth and patterning need to be precisely orchestrated in both space and time. Genetic analyses and experimental embryology studies have revealed the existence of multiple cross-regulatory signalling systems that confer developmental stability, while at the same time leave room for evolutionary modifications to occur therein (Zeller et al., 2009; Suzuki, 2013; Petit et al., 2017). This task, however, is complicated by functional units inside the limb that consist of multiple tissue types, some of which originate from different embryonic precursor pools. For example, skeletal cells of the limb musculoskeletal apparatus originate from lateral plate mesoderm precursors (Gilbert, 2010). Somite-derived muscle cells migrate into the limb bud, form distinct muscle groups and attach to the developing skeletal elements *via* tendons (Chevallier et al., 1977; Kardon, 1998; Schweitzer et al., 2010; Sharir et al., 2011; Francisco Botelho et al., 2015). Motor neurons residing in the spinal cord, and sensory neurons in the dorsal root ganglia, project their axons into the limb periphery to connect to these muscles in a highly stereotypical manner (Landmesser, 1978, 2001; Bonanomi, 2019). Hence, embryonic patterning of these three tissues needs to be tightly coordinated, to successfully integrate skeletal, muscular and neural anatomy, and produce a fully operational limb. Likewise, evolutionary modifications in the pattern of any one of these tissues necessitate parallel alterations in the morphology of the others.

Over the course of vertebrate evolution, the skeleton of tetrapod limbs has greatly diversified, reflecting adaptations to a variety of different styles of locomotion. In the proximal parts of the limb the number of skeletal elements is largely conserved, with evolutionary modifications occurring predominantly through changes in length and girth of the respective bones (Kronenberg, 2003; Hall, 2015). Such alterations can be apparent even within a single species, due to different locomotor behaviours associated with the respective fore- and hindlimbs (Cooper, 2011; Wimsatt, 2012; de Bakker et al., 2013). The most striking differences, however, have appeared in the skeleton of the autopod, with changes occurring in both digit patterns and numbers (Wagner and Chiu, 2001; Richardson and Chipman, 2003). Based on seminal work in

* Corresponding author.
E-mail address: patrick.tschopp@unibas.ch (P. Tschopp).
[1] Equally contributing.

https://doi.org/10.1016/j.ydbio.2019.10.035
Received 17 July 2019; Received in revised form 30 October 2019; Accepted 30 October 2019
Available online 4 November 2019

traditional model organisms, we now have the ability to elucidate these evolutionary autopod diversifications at the molecular level (Zuniga, 2015; Petit et al., 2017). For example, variations in Sonic Hedgehog signalling pathway activity have been demonstrated to affect digit numbers in a wide range of tetrapod species (Shapiro et al., 2003; Lettice et al., 2008; Cooper et al., 2014; Lopez-Rios et al., 2014). The resulting morphological changes in the autopod, however, have so far mainly been studied at the skeletal level, while muscle and nerve modifications in experimentally altered limbs have only been described at more proximal levels (Stirling and Summerbell, 1988; Duprez et al., 1999).

Here, capitalizing on the power of whole-mount immunohistochemistry and light-sheet fluorescent microscopy (LSFM), we present a 3D-atlas of the developing neuromuscular system in distal chicken limbs. While early muscle patterning occurs in a largely uniform dorso-ventral manner, we find a relative rotation of the main motor nerves between wings and legs. By experimentally altering the skeletal formula of the autopod, we challenge the developmental plasticity of these two distinct neuromuscular architectures to adapt to changes in dactyly. Intriguingly, we find that while the musculature closely follows changes in skeletal topology, wing and leg innervation patterns are only partially responsive. This apparent discrepancy in patterning flexibility, between the muscular and nervous systems, has implications for the evolutionary diversification of the vertebrate autopod, as well as for the different congenital malformations affecting human hands and feet.

2. Results and discussion

2.1. 3D-analysis of neuromuscular development in chicken limbs

In order to monitor the coordinated patterning of nerves and muscle groups, we first produced a 3D-atlas of the developing neuromuscular system in chicken fore- and hindlimbs. Through whole-mount double-immunohistochemistry against neuron-specific intermediate filament protein (neurofilament, '*NF200*') and muscle-specific myosin heavy chain (MHC, '*MF20*'), we visualized the appearance of limb nerves and muscle groups, respectively. Following CUBIC clearing, LSFM image acquisition and 3D-reconstruction (Susaki et al., 2014; Belle et al., 2017), segmentation-based tracing was used to delineate and pseudo-colour major nerves and muscle bundles (Fig. 1A and B; Figs. S1A and B; Figs. S2A and B). Using this experimental workflow, we produced a developmental time-series for both wing and leg, spanning stages Hamburger-Hamilton (HH) HH26 to HH36 (day 5 to day 10 of development; Hamburger and Hamilton, 1951) (Fig. 1C and D; Figs. S1C–F; Figs. S2C–F; Movie 1 and 2).

Supplementary video related to this article can be found at https://doi.org/10.1016/j.ydbio.2019.10.035.

At day 5 of development in the wing, growing axons are invading the bud and form two main fascicles, one dorsal (n. brachialis superior) and one ventral (n. brachialis inferior) (data not shown). Around day 6, further subdivisions become evident, giving rise to the three major nerve branches of the limb that contain the projecting axons of motor and sensory neurons: the radial nerve (cyan) on the dorsal side; the median (yellow) and ulnar nerve (magenta) on the ventral side. From there, the branches split further to innervate in a stereotypical and non-overlapping manner the musculature of the forming digit territories, which become visible at later time-points (day 7 to day 10) (Fig. 1C, Figs. S1C and E). Three main nerve branches also connect to the leg musculature. Dorsally, two arched nerves, the median (green) and lateral (orange) fibulars, share a common peroneal origin (Fig. S2C). On the ventral side, innervation of the foot is provided by the plantar nerve (Fig. S2E, purple).

In parallel to limb innervation, muscle precursors aggregate and differentiate into dorsal and ventral muscles masses, soon after their

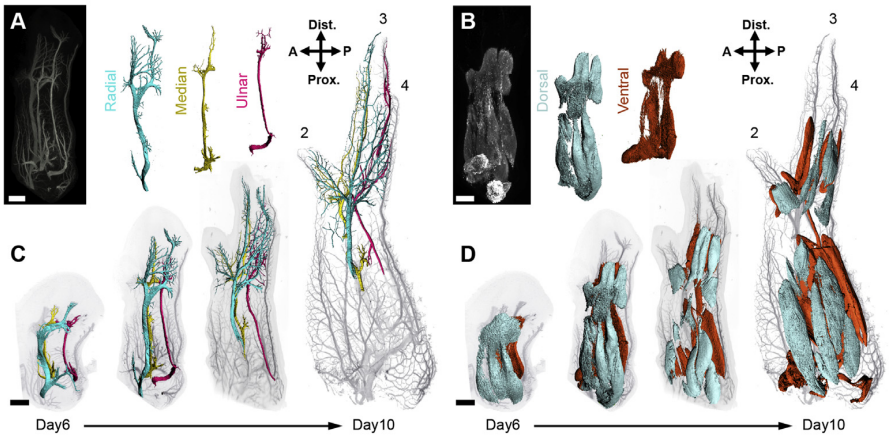

Fig. 1. 3D-analysis of the developing neuromuscular system in the chicken forelimb. (A, B) Image acquisition and analysis workflow used to identify nerves innervating the autopod and its corresponding muscle masses. Nerves and muscles were visualized with antibodies against neurofilament (*NF200*) and myosin heavy chains (*MF20*) and imaged with a light sheet microscope. After 3D reconstruction of the embryonic wings, surfaces were rendered using segmentation-based tracing to highlight structures of interest. The radial nerve (cyan) innervates the dorsal muscle mass (light blue), while the median nerve (yellow) anteriorly and the ulnar nerve (magenta) posteriorly connect to the ventral muscle mass (red). (C,D) Dorsal view of the neuromuscular development in the wing between day 6 and day 10 of development. In this time window, motor and sensory axons invade the developing wing and simultaneously muscle bellies segregate from dorsal and ventral muscle masses. The radial nerve innervates all three digits in the dorsal part whereas ventrally, the median arborizes into digit 1 and digit 2 and the ulnar in digit 2 and 3. A/P, anterior/posterior, Prox./Dist., proximal/distal. After day 7, limbs were cropped at zeugopod levels, to allow visualization of the intermediate tendon primordia location (forearm-hand junction). Scale bars represent approx. 500 μm.

migration from the dermomyotome (Schramm and Solursh, 1990; Hayashi and Ozawa, 1995) (data not shown). These two masses then split along the antero-posterior (A/P) and proximo-distal (Prox./Dist.) axes to form the individual muscles of the wing and the leg (Fig. 1D; Figs. S1D and F; Figs. S2D and F). At day 6, the hand/foot muscles masses are still continuous with the forearm/shank that has started to cleave along its A/P axis. From day 7 onwards this connection is progressively lost, with a spatial detachment of the forearm/shank and hand/foot muscles masses at the intermediate tendon primordia levels (Kardon, 1998). Starting around the same stage, discrete hand and foot muscles separate anteriorly-posteriorly from their primary muscle masses. Those muscles become increasingly individualized, elongate and adopt their eventual fusiform shape from day 8 to day 10. As such, they give rise to a precise muscular topology, with eleven main muscles in the wing autopod and seven in the foot (Figs. S3A–D). At similar developmental stages both muscle individualization and peripheral nerve branching appear more advanced in the hindlimb than in the forelimb. These observations support the notion that a developmental heterochrony may exist between embryonic chicken limbs, with the development of legs being slightly more advanced than in wings (Bininda-Emonds et al., 2007). Collectively, we present a comprehensive 3D-atlas of the developing neuromuscular system in chicken wings and legs at high spatial and temporal resolution.

2.2. Differential innervation patterns between the wing and the leg

Although both fore- and hindlimbs display three major motor axon-containing nerve branches, their A/P and D/V (dorso-ventral) layouts show striking differences. Namely, while a single nerve (radial, cyan) occupies the anterior-dorsal quadrant of the wing cross-section, this arrangement is inverted for the plantar nerve (purple) in the posterior-ventral sector of the leg (Fig. 2A and B). The median-ulnar (yellow, magenta) and median fibular-lateral fibular (green, orange) nerve pairs reside in the ventral and dorsal halves of the wing and leg, respectively. These distinct nerve arrangements are unlikely to result from the different rotations of the adult limbs, relative to the main body axis, as at the time of nerve invasion the orientations of fore- and hindlimbs are identical. Accordingly, dorsal wing and leg extensor muscles are predominantly innervated by either single (wing) or double (leg) nerve branches, with the ventrally located flexors displaying the opposite configuration (Fig. 2C). In addition to differences in nerve branch arrangements along the A/P and D/V axes, the single nerves in the wing and the leg also display distinct A/P projection routes. While the radial nerve follows a distal curvature reaching from the anterior to the posterior side of the dorsal wing, the ventral plantar nerve takes an opposite trajectory, posterior to anterior in the foot (Fig. 2D and E). Moreover, both paired nerves, median-ulnar ventrally in the wing and median fibular-lateral fibular dorsally in the leg, fuse and produce an arched structure whose location coincides with the proximal onset of the respective autopod muscle groups (Fig. 2D and E; arrows). Hence, these results illustrate an inverted configuration for the basic innervation patterns of the chicken wing and the leg (Fig. 2B, Movie 3). Such an inverted arrangement of the major nerve branches in wings and legs also suggest a differential pre-disposition in their ability to respond and adapt to changes in skeleton and/or muscle anatomy.

Supplementary video related to this article can be found at https://doi.org/10.1016/j.ydbio.2019.10.035.

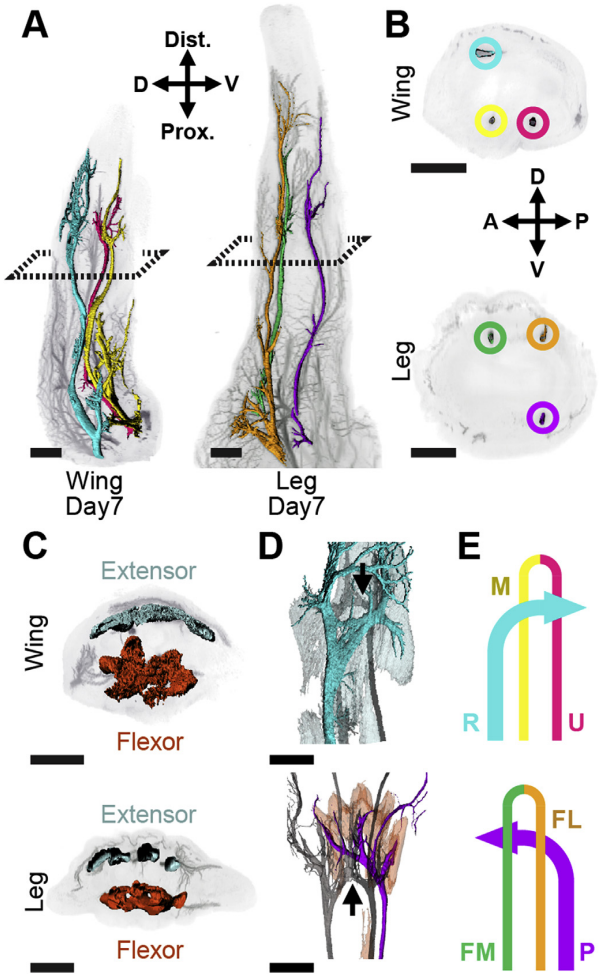

Fig. 2. Differential innervation patterns in chicken wings and legs. (A,B) Side views (A) and virtual cross sections (B) of the nervous systems at the indicated levels (A, dashed lines) of a 3D-reconstructed wing and leg at day 7 of development. Three main motor axon-containing nerves project into both wing and leg. In the wing, we find one dorsal-anterior (Radial, cyan) and two ventral nerves (Median and Ulnar, yellow and magenta). In the leg, one nerve (Plantar, purple) can be found posterior-ventrally, while two nerves (Median fibular and Lateral fibular, green and orange) innervate the dorsal musculature. (C) Virtual cross sections of the muscle masses at the autopod level at day 7 of development. In both wing and leg, dorsal and ventral masses give rise to extensor and flexor muscles, respectively. (D,E) Dorsal views (D) and schematics (E) of wing and leg innervation patterns. In the wing, the dorsal radial nerve reaches all extensor muscles by projecting from anterior to posterior, while the ventral plantar nerve innervates flexor muscles by turning from posterior to anterior in the leg. The paired nerve branches, ventral in the wing and dorsal in the leg, fuse distally to from an arched structure (D, arrows). D/V, dorsal/ventral, Prox./Dist., proximal/distal; A/P, anterior/posterior. R, radial nerve; M, median nerve; U, ulnar nerve; FM, medial fibular; FL, lateral fibular; P, plantar. Scale bars represent approx. 500 μm.

2.3. Innervation plasticity in polydactyl wings and legs

Limb innervation patterns develop in highly stereotypical fashion. Their ability to adapt to skeletal changes has been previously evaluated at proximal limb levels (Lance-Jones and Landmesser, 1981; Stirling and Summerbell, 1988). Based on these pioneering studies, we decided to re-visit this apparent plasticity of limb nervous system. We capitalized on the superior resolution offered by LSFM, and decided to focus on the distal limb, the autopod, i.e. the site of major evolutionary alterations and fine motor skills control. In order to challenge the system with extra digits, we took advantage of the chick limb model (Davey et al., 2018) using a well-established model of vertebrate polydactyly. At day 3 of development, we implanted retinoic acid-soaked beads at the anterior margin of the developing limb. This experimental manipulation is known to lead to mirror-image duplications in limb skeletal patterns, *via* the

ectopic induction of *Shh* expression anteriorly (Tickle et al., 1982; Pickering et al., 2017) (Fig. S4). For autopods showing complete (wing) or partial (leg) mirror duplication, the effects on axonal pathfinding and muscle patterning were evaluated using the same staining and imaging procedures as described above.

Three days after bead implantation in the wing (day 6), both radial and median nerves seem affected and show important defasciculations at anterior-distal levels (Fig. 3A and B, arrow). The ulnar nerve, however, remains unchanged (Fig. 3B). At later stages (day 7 to day 9), we observe a complete bifurcation of the radial and median nerves, which now have invaded the polydactyl territory (Fig. 3B and C asterisks; Figs. S5A and B). At hindlimb levels, the first signs of nerves branching toward the extra digit territory also appear three days after bead implantation. The posteriorly located lateral fibular nerve is not affected, reminiscent of the fate of the ulnar nerve in the polydactyl wing (Fig. 3D–F). The anterior median fibular nerve branch, however, defasciculates and invades the anterior duplicated side, similar to the wing median nerve. Additionally, it forms an arched structure onto itself (Fig. 3E and F, arrowheads; Figs. S5C and D). In the ventral side of the polydactyl foot, the plantar nerve extends slightly further into the anterior part, with a more pronounced distal-to-proximal curvature than in controls (Figs. S5C and D), yet it does not split in response to the anterior addition of an extra digit. Surprisingly, however, an ectopic projection from the lumbosacral plexus invades the anterior margin of the hindlimb field. At later stages, the plantar nerve and the ectopic projection meet distally and form an arch from which additional branches project to the duplicated digits, in a pattern similar to control limbs (Fig. 3E and F, arrow; Figs. S5C and D).

To assess the neuronal nature of these ectopic projections in polydactyl wings and legs, we performed immunohistochemistry to discriminate motor from sensory nerves. We employed a triple labeling approach, using a pan-neuronal (beta-tubulin, '*Tuj1*' (Belle et al., 2017; Friocourt et al., 2017); and a sensory neuron marker (transient adhesion glycoprotein-1, '*Tag-1*' (Ruegg et al., 1989; Karagogeos et al., 1997; Belle et al., 2017);, together with a muscle-specific staining (fast Myosin Heavy-Chain, '*MyHC*'). This combination allowed us to distinguish motor from sensory neurons, as the projections of the former stained strongly for *Tuj1*, but were largely devoid of *Tag-1*, when exiting the lateral motor column (LMC) of the spinal cord (Fig. S6A). At proximal levels, in both native and duplicated autopod sides, we found evidence of innervation by motor as well as sensory axons (Fig. 3G–J). Importantly, nerves inside of muscles bundles stained predominantly with *Tuj1* only, indicating that they were made of motor axons coming from the LMC (Fig. 3G–J, arrowheads). At more distal levels, i.e. beyond the autopod musculature, as well as inside the skin, only *Tuj1/Tag-1* double-positive sensory nerves were detected (Figs. S6A and B).

Hence, in polydactyl fore- and hindlimbs, supernumerary digits are innervated by both motor and sensory neurons, along ventral and dorsal routes, through defasciculation and eventual nerve bifurcations at the level of the developing mesopod. This suggests the presence of an additional A/P "choice point" in the limb periphery, to ensure digit-specific innervation patterns (Bonanomi, 2019). Moreover, the response to such putative guidance signals seems plastic and can be modulated by the

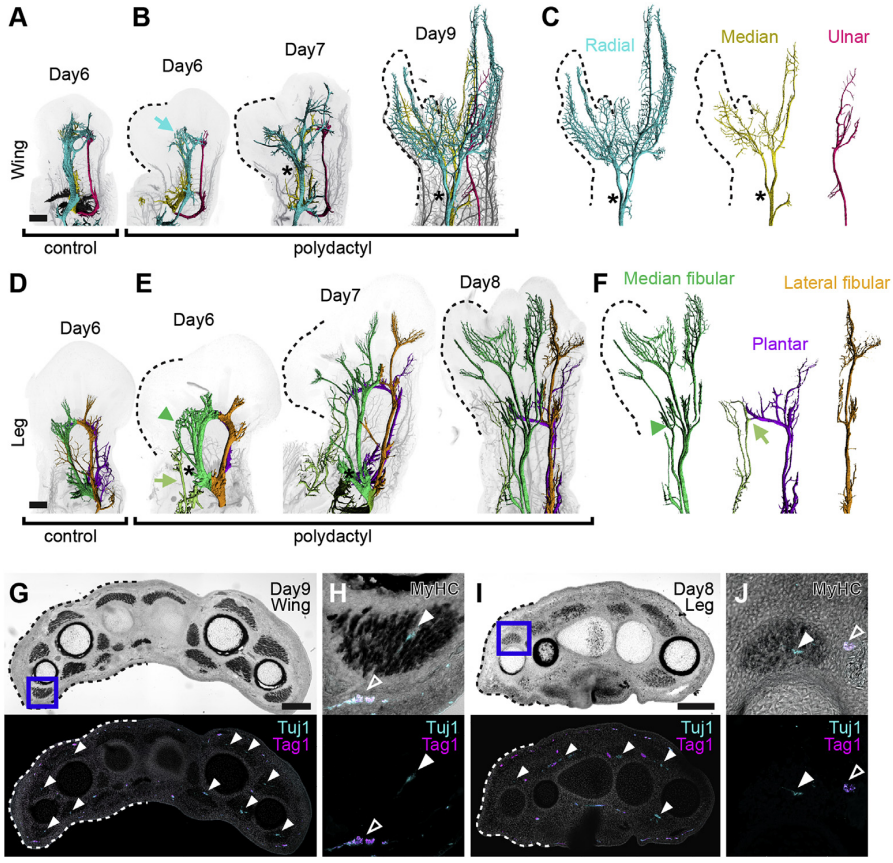

Fig. 3. Modified motor and sensory innervation patterns in polydactyl wings and legs. (A–C) Dorsal view of developmental progression of innervation patterns in control (A) and polydactyl wings (B). An arrow highlights the early defasciculation of the radial nerve (B), with the median following approximately one day later. Asterisks mark the ectopic bifurcation points of the respective nerves. The overall pattern of the ulnar nerve does not seem to be affected by the polydactyly (B,C). Both radial and median nerves bifurcate and innervate the duplicated digit territories (C, dotted lines). (D–F) Dorsal view of developmental progression of innervation patterns in control (D) and polydactyl legs (E). The median fibular nerve defasciculates to innervate the dorsal half of the extra digit, and forms a persistent arched structured with itself (E,F; arrows). In the ventral portion of the leg, an ectopic projection (E,F, olive green) emerges and fuses with the plantar nerve into an additional arch (F, arrowhead). The lateral fibular nerve does not respond to the presence of an extra digit. (G–J) Innervation of extra digit territories by both motor and sensory neurons in polydactyl wings (G,H) and legs (I,J). Motor axon projections inside muscle bundles stain for *Tuj1* only (G-J, arrowheads), whereas as sensory nerves are *Tuj1/Tag-1* double-positive (H,J, empty arrowheads). Blue boxes in (G,I) corresponds to magnified views of the FDQ′ and d_a muscles in (H,I), respectively (see Fig. 5B,D for muscles nomenclature). All images anterior to the left, dotted lines demarcate polydactyl sides. Scale bars represent approx. 500 μm in A-F, 250 μm in G,I.

presence of additional digit territories. However, only two of the three major nerves seem responsive to project to the extra digits. Therefore, and in contrast to the symmetric addition of skeletal elements in polydactyl wings (Tickle and Towers, 2017), the corresponding innervation patterns do not represent a full mirror-image duplication.

2.4. Differential response of muscle and nerve patterns to a polydactyl autopod environment

We next analysed the resulting changes in muscle patterns in polydactyl fore- and hindlimbs. Since alterations in the forearm musculature have been previously reported (Duprez et al., 1999), we again focused our attention on the impact of wing and leg digit duplications on the respective autopod muscle groups. In both situations, three days after bead implantation, the extensor and flexor masses appear expanded and the muscles fibers re-orient themselves towards the native and duplicated digit territories. At later stages (day 7 to day 8–9), we first observed the appearance of partial, supernumerary splits in the expanded muscles masses. These splits eventually resolve into completely individualized extra muscle bundles, regardless of whether a true mirror-duplication of the skeletal structure (wing) or the addition of a single anterior digit (leg) occur (Fig. 4A–F).

In case of the duplicated wing, the morphology of these additional muscles allows for the identification of their homeotic identities, which closely follow the underlying skeletal topology (Fig. 5A and B). As a result, duplicated posterior-ventral muscles are now ectopically contacted by the anterior split branch of the median nerve, instead of the ulnar. Thereby, they have altered their connectivity to the spinal cord compared to the native, control-side counterparts (e.g. FDQ', Fig. 5B; Fig. 3C,H). For the leg, the partial duplication of the autopod skeleton complicates a clear muscle identity assignment. As for the wing, however, a pair of ectopic muscles appears – one dorsal, one ventral to the anterior extra digit (Fig. 5C and D). Hence, unlike for the nervous system, all extra digits in wings and legs are matched with corresponding, additional muscle bundles, thereby perfectly complementing the skeletal alterations at the level of the musculature.

To follow the temporal dynamics of these extensive reorganizations, and estimate the potential variability associated with, we assessed muscle and nerve alterations along our experimental time lines. We followed muscle changes at the level of splitting and individualization, whereas nerves were scored for defasciculations, bifurcations and potential ectopic fusions. Plotting these results along spatiotemporal axes revealed a posterior-to-anterior sequence of muscle maturation in the wing, which is recapitulated on the mirror-duplicated side (Fig. 5E). A similar trend can be observed for the leg musculature, and both duplicated sides in wings and legs show a slight developmental delay compared to their native counterparts (Fig. 5E and F). At the innervation level, the first visible signs of nerve re-arrangements appear roughly a day earlier than for the musculature, and the two most posterior branches, the ulnar (wing) and the lateral fibular (leg), remain unaffected throughout development (Fig. 5G and H). Thus, as for the final pattern alterations, the underlying spatiotemporal dynamics are different between nerves and muscles, indicating that they are subject to distinct patterning mechanisms.

Collectively, we report differences in the developmental plasticity of the autopod neuromuscular system in response to additional digits. On the one hand, muscle groups seem perfectly able to adapt their patterning to ectopic cues in the polydactyl autopod (e.g. muscle connective tissue and tendon attachment sites), refine their shapes accordingly and connect to the underlying skeletal elements (Fig. 5I,K) (Schweitzer et al., 2010; Diogo et al., 2015; Huang et al., 2015; Vallecillo-García et al., 2017). Invading nerves, on the other hand, show less flexibility in their response to autopod alterations (Fig. 5J,L). They seem constrained by their projection routes, i.e. from where they send axons into the limb periphery, and remain attached to their cell bodies in the developing spinal cord (Bonanomi, 2019). Importantly, not only does this physical connection to the spinal cord restrict these nerves sterically, but it also shapes the molecular make-up of their growth cones *via* spinal cord-intrinsic patterning systems (di Sanguinetto et al., 2008; Gouti et al., 2015; Bonanomi, 2019). As such, it modulates the extent to which growing nerves can respond to alterations in peripheral axon guidance molecules. From an evolutionary perspective, our results thereby imply the presence of distinct developmental constraints, due to the need for coordinated patterning alterations in all components of the limb musculoskeletal apparatus. Namely, the fact that nerve projection routes are not entirely dependent on peripheral cues will impose functional

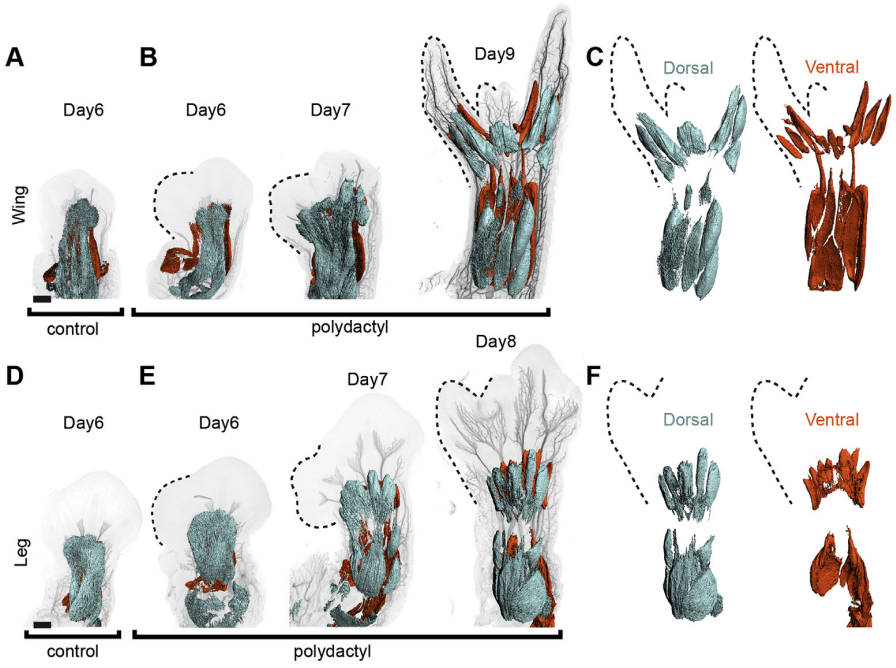

Fig. 4. Modified muscle development in wing and leg polydactylies. (A–F) Dorsal view of muscle development in control and polydactyl wings (A–C) and legs (D–F). At day 6, distal muscle masses are expanded along the anterior-posterior axis, and start to split at around day 7 (B). At day 9, wing dorsal (extensor, blue) and ventral (flexor, red) muscles are completely split and individualized into a complete mirror-duplicate pattern and connect to all digits in both native and duplicated halves of the autopod (dotted lines, C). Likewise, similar dynamics lead to all native and extra digits in the foot being matched by dorsal (extensor, blue) and ventral (flexor, red) muscle groups (dotted lines, F). All images anterior to the left, distal on top. Scale bars represent approx. 500 µm.

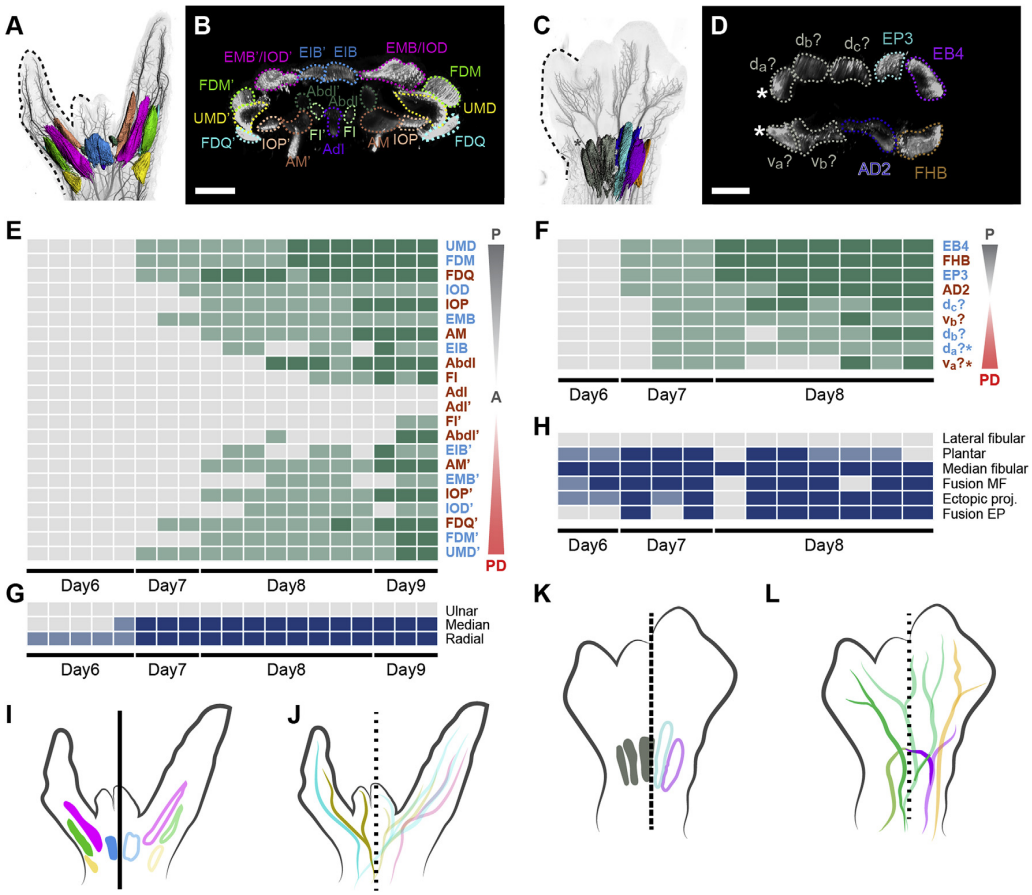

Fig. 5. Differential response of muscle and nerve patterning to wing and leg polydactylies. (A–D) Full mirror-duplication of the wing musculature (A,B), and extra dorsal and ventral muscle bundles matching the single supernumerary digit in the foot (C,D). (A,B) Dorsal view (A) and virtual cross section (B) of the musculature in a polydactyl wing at day 9 of development. Muscle identity is indicated by pseudo-coloration of muscles groups. (C,D) Dorsal view (C) and virtual cross section (D) of the musculature in a polydactyl leg at day 8 of development. Identifiable muscles are indicated by pseudo-coloration, supernumerary muscles marked with an asterisk. (E–H) Temporal and spatial appearance of muscle (E,F) and nerve (G,H) pattern alterations. Dorsal (light blue) and ventral (maroon) muscles are arranged top to bottom, from posterior-native, to anterior, to polydactyl side. Muscle masses are scored as partially split (light green) or completely individualized (dark green), nerve alterations (e.g. bifurcations) as partial (light blue) or complete (dark blue, see Material and Methods for details). (I–L) Schematics of muscle and innervation patterns in polydactyl wings (I,J) and legs (K,L). While muscle patterns are completely mirror-duplicated (I, continuous line), or follow the underlying skeletal topology (K, broken line), nerves are only partially responsive (J,L, dotted lines). Only two wing nerves, median (yellow) and radial (cyan), out of three show alterations (J, solid colors). Likewise, only the median fibular (green) and plantar (purple) show changes in morphology (L, solid colors). Moreover, we observe the emergence of an ectopic projection (olive green) joining the plantar nerve. A/P, anterior/posterior, PD, polydactyl. For muscle abbreviations, refer to Fig. S3. Scale bars represent approx. 500 μm.

patterning barriers that may prevent certain autopod morphologies from being realized. Moreover, the rotated configuration we describe for fore- and hindlimb innervation patterns highlights that any discussion of serial homology and individualization of tetrapod limbs should not focus exclusively on skeletal elements, but consider the entire musculoskeletal apparatus as a functional unit (Shubin et al., 1997; Young and Hallgrímsson, 2005; Wagner, 2014). From a medical point of view, our findings offer a conceptual framework to understand the varying degrees of motor abilities observed in different forms of human hand and foot polydactylies (Askari et al., 2016; Mehring et al., 2019).

3. Material and methods

3.1. Experimental polydactyly

Fertilized chicken eggs (Gallus gallus domesticus) were purchased from local vendors in Switzerland. Eggs were incubated, opened and staged according to standard protocols (Hamburger and Hamilton, 1951; Ros et al., 2000). AG1-X2 resin (BioRad laboratories) were derivatised with formic acid and washed in water to adjust the pH around 4.5–5. They were then soaked in all-*trans*-retinoic acid (1 mg/ml dissolved in DMSO, Sigma) for at least 20 min at room temperature and washed in DMEM with phenol red (GIBCO™ GlutaMax), before being grafted into the anterior-distal margin of chick wing or leg buds at day 3 of development (HH19) (see Tickle et al., 1985; Ros et al., 2000). Polydactyl embryos were dissected after 3–6 days post implantation. In total, we analysed 19 polydactyl wings with mirror digit duplication and 12 legs with an extra digit.

3.2. Whole-mount immunostaining and tissue clearing

Embryos were dissected and immediately fixed in Dent's fix (4:1 Methanol:DMSO) for at least one week and stored at −20 °C until immunostaining. To remove pigmentation and increase signal-to-noise

ratio, we bleached the dissected embryos overnight at 4 °C in Dent's bleach solution (4:1:1; Methanol:DMSO:hydrogen peroxide) (Kardon, 1998). The following day, samples were re-rehydrated in decreasing MeOH/PBT (1x PBS-1%, Triton X-100) series, washed 2 times in PBT and then blocked for 1 h in PBT-5% DMSO-5% sheep serum (blocking solution) at room temperature on a shaker. For double-immunostaining, samples were incubated in blocking solution with primary antibodies against neurofilament (*NF200*, Sigma, dilution 1:500) and muscle specific myosin heavy chain (*MF20*, DSHB, dilution 1:100) and placed at 4 °C, with rotation for 2 nights. This was followed by 1h washes in PBT along the day. Next, samples were incubated in secondary antibodies (α-mouse AF488 and α-rabbit Cy3; Jackson ImmuResearch, dilution 1:500) diluted in blocking solution for 2 nights at 4 °C. After 6 washes of 1 h in PBT at room temperature, samples were quickly washed 2 times in 1x PBS before clearing. Tissue clearing was carried out with CUBIC method as described previously (Susaki et al., 2015). Briefly, samples went through delipidation in CUBIC 1 solution followed by 2% agarose embedding and 48 h incubation in CUBIC 2 solution before imaging.

3.3. Light-sheet microscopy

Images were acquired on a ZEISS lightsheet Z1 microscope using the Zen 2014 software (ZEISS). The lightsheet was generated by lasers (wavelength 488 nm and 561 nm) and dual side illumination was applied (Illumination optics Lightsheet Z.1 5 × /0.1 ZEISS). Fluorescent signals were detected with 5X air detection objectives for clearing chambers (Lightsheet Z.1 detection optics 5 × /0.16 clearing, n = 1.45, ZEISS) and acquired with PCO.Edge sCMOS cameras (liquid cooled, 1920 × 1920 pixels, 16-bit readout). Stained and cleared samples were submerged in a chamber filled with CUBIC 2 solution. Tiles were defined with TileScan (ZEISS) for big samples, step size was optimized by Zen. All images were acquired in 16-bit.

3.4. 3D imaging and image processing

After acquisition, Zeiss.czi light-sheet microscopy files for all tiles, were loaded in ArivisVision4D (Arivis) and stitched together. All planes were exported (.tiff) and loaded in Imaris 9.1.2 (Bitplane) to create an Imaris file (.ims) and to carry out further analyses. 3D volumes were created, nerves and muscles were segmented by thresholding and surfaces were created with the Imaris "surface" plug-in. Main nerves were identified and pseudo colored (Labels) for visualization purposes. At later stages, surface rendered nerves innervating the skin were removed manually. Optical slices were obtained with the Imaris "Ortho Slicer" and "Oblique Slicer" plug-ins. To visualize the shape of the limbs after surface rendering, the gamma was set to 2 and the maximum value was set high. Images (.tiff) and videos were created with Imaris "snapshot" and "animation" plug-ins. For figures, separate images of the surface rendered data and the shape of the limbs were taken and superposed in Fiji (Schindelin et al., 2012). Movies, created in Imaris, were put side-by-side and captions were added in Adobe Premier Pro 2017 (Adobe® Creative Cloud®).

3.5. Phenotypic scoring of polydactyl limbs

For phenotypic scoring of polydactyl limbs, we selected only wings showing mirror-image duplications with 43234 or 432234 digit formulas, and legs with five digits. Changes in muscle patterning were scored as 'partial', i.e. differential fiber orientation and elongation at the tip of the bundle (color code = light green, Fig. 5E and F; see e.g. 'Day 7' in Fig. 4B) or 'complete', i.e. individualization of muscle bundles into their characteristic shapes (color code = dark green, Fig. 5E and F; see e.g. 'Day 9' in Fig. 4B) Likewise, we classified alterations in nerve projection routes into two categories: 'defasciculation' (color code = light blue, Fig. 5G and H; see e.g. arrow in Fig. 3B) or 'complete split' (color code = dark blue, Fig. 5G and H; see e.g. asterisks in Fig. 3B). Moreover, we assessed the emergence of the ectopic projection in the leg (light blue = proximally restricted, dark blue = distally extended), its potential fusion with the plantar nerve (dark blue), as well as the fusion of the median fibular with itself, (light blue = partial, dark blue = complete).

3.6. Immunostaining on cryosections

Embryonic tissues were fixed in 4% PFA, cryoprotected in sucrose and sectioned at 20 μm thickness. Immunohistochemistry was performed using standard protocols (Tschopp et al., 2014). Samples were stained with primary antibodies against *Tuj-1* (mouse, MMS-435P, 3 μg/ml concentration, Covance), *Tag1* (rabbit, kind gift of E. Stoeckli, dilution 1:1000 (Ruegg et al., 1989),) and fast Myosin Heavy-Chain (MyHC) conjugated to Alkaline Phosphatase (mouse, A4335; MY32-AP; dilution 1:100; Sigma) in order to visualize all neuron fibers, sensory nerves and skeletal muscles, respectively. Stainings were revealed using fluorescent secondary antibodies (1:500, Jackson ImmunoResearch) or NBT/BCIP reactions.

3.7. Confocal microscopy

Confocal images were acquired on an Olympus FLUOVIEW FV3000, using either 10x/0.4 (air, ApoPlan, Olympus) or 60x/1.3 (silicon oil immersion ApoPlan, Olympus) objectives. Continuous laser beams were generated at 488 nm and 647 nm wavelength (OBIS, Coherent). For 10x overviews, tiled images were stitched in Fiji (Preibisch et al., 2009). All images were globally adjusted for contrast and brightness using ImageJ.

Funding

This work was supported by the Swiss National Science Foundation (SNSF project grant 31003A_170022 to PT) and the University of Basel. ML is supported by the *Forschungsfonds* of the University of Basel.

Declaration of competing interest

The authors declare that they have no competing interests.

Acknowledgements

The authors would like to thank Marian Ros for the warm welcome in her lab to train in the beads implantation technique; the Biozentrum Imaging Core Facility for assistance with light-sheet microscopy and image analysis; Esther Stöeckli for the generous gift of the *Tag1* antibody; all lab members for insightful discussions; and Alice Davy, Marian Ros and Cliff Tabin for helpful comments on the manuscript. PT would also like to acknowledge the generous support of Cliff Tabin, in whose lab this project was initiated (with help of NIH grant HD03443 to Cliff Tabin).

Appendix A. Supplementary data

Supplementary data to this article can be found online at https://doi.org/10.1016/j.ydbio.2019.10.035.

References

Askari, M., Christensen, K.N., Heath, S., Moran, S.L., Lachman, N., 2016. Presentation of soft tissue anatomy of mirror hand: an anatomical case report with implications for surgical planning. Surg. Radiol. Anat. 38, 855–862.

Belle, M., Godefroy, D., Couly, G., Malone, S.A., Collier, F., Giacobini, P., Chédotal, A., 2017. Tridimensional visualization and analysis of early human development. Cell 169, 161–173 e12.

Bininda-Emonds, O.R., Jeffery, J.E., Sánchez-Villagra, M.R., Hanken, J., Colbert, M., Pieau, C., Selwood, L., ten Cate, C., Raynaud, A., Osabutey, C.K., et al., 2007. Forelimb-hindlimb developmental timing changes across tetrapod phylogeny. BMC Evol. Biol. 7, 182.

Bonanomi, D., 2019. Axon pathfinding for locomotion. Semin. Cell Dev. Biol. 85, 26–35.

Chevallier, A., Kieny, M., Mauger, A., 1977. Limb-somite relationship: origin of the limb musculature. Development 41, 245–258.

Cooper, K.L., 2011. The lesser Egyptian jerboa, *Jaculus jaculus* : a unique rodent model for evolution and development: figure 1. Cold Spring Harb. Protoc. 2011 pdb.emo066704.
Cooper, K.L., Sears, K.E., Uygur, A., Maier, J., Baczkowski, K.-S., Brosnahan, M., Antczak, D., Skidmore, J.A., Tabin, C.J., 2014. Patterning and post-patterning modes of evolutionary digit loss in mammals. Nature 511, 41–45.
Davey, M.G., Towers, M., Vargesson, N., Tickle, C., 2018. The chick limb: embryology, genetics and teratology. Int. J. Dev. Biol. 62, 85–95.
de Bakker, M.A.G., Fowler, D.A., Oude, K. den, Dondorp, E.M., Navas, M.C.G., Horbanczuk, J.O., Sire, J.-Y., Szczerbińska, D., Richardson, M.K., 2013. Digit loss in archosaur evolution and the interplay between selection and constraints. Nature 500, 445–448.
di Sanguinetto, S.A.D.T., Dasen, J.S., Arber, S., 2008. Transcriptional mechanisms controlling motor neuron diversity and connectivity. Curr. Opin. Neurobiol. 18, 36–43.
Diogo, R., Walsh, S., Smith, C., Ziermann, J.M., Abdala, V., 2015. Towards the resolution of a long-standing evolutionary question: muscle identity and attachments are mainly related to topological position and not to primordium or homeotic identity of digits. J. Anat. 226, 523–529.
Duprez, D., Lapointe, F., Edom-Vovard, F., Kostakopoulou, K., Robson, L., 1999. Sonic Hedgehog (SHH) specifies muscle pattern at tissue and cellular chick level, in the chick limb bud. Mech. Dev. 82, 151–163.
Francisco Botelho, J., Smith-Paredes, D., Soto-Acuña, S., Mpodozis, J., Palma, V., Vargas, A.O., 2015. Skeletal plasticity in response to embryonic muscular activity underlies the development and evolution of the perching digit of birds. Sci. Rep. 5, 9840.
Friocourt, F., Lafont, A.-G., Kress, C., Pain, B., Manceau, M., Dufour, S., Chédotal, A., 2017. Recurrent *DCC* gene losses during bird evolution. Sci. Rep. 7, 37569.
Gilbert, S.F., 2010. Developmental Biology. Sinauer Associates.
Gouti, M., Metzis, V., Briscoe, J., 2015. The route to spinal cord cell types: a tale of signals and switches. Trends Genet. 31, 282–289.
Front-matter. In: Hall, B.K. (Ed.), 2015. Bones and Cartilage, second ed. Academic Press, San Diego, pp. i–iii.
Hamburger, V., Hamilton, H.L., 1951. A series of normal stages in the development of the chick embryo. J. Morphol. 88, 49–92.
Hayashi, K., Ozawa, E., 1995. Myogenic cell migration from somites is induced by tissue contact with medial region of the presumptive limb mesoderm in chick embryos. Development 121, 661–669.
Huang, A.H., Riordan, T.J., Pryce, B., Weibel, J.L., Watson, S.S., Long, F., Lefebvre, V., Harfe, B.D., Stadler, H.S., Akiyama, H., et al., 2015. Musculoskeletal integration at the wrist underlies the modular development of limb tendons. Development 142, 2431–2441.
Karagogeos, D., Pourquié, C., Kyriakopoulou, K., Tavian, M., Stallcup, W., Péault, B., Pourquié, O., 1997. Expression of the cell adhesion proteins BEN/SC1/DM-GRASP and TAG-1 defines early steps of axonogenesis in the human spinal cord. J. Comp. Neurol. 379, 415–427.
Kardon, G., 1998. Muscle and tendon morphogenesis in the avian hind limb. Development 125, 4019–4032.
Kronenberg, H.M., 2003. Developmental regulation of the growth plate. Nature 423, 332–336.
Lance-Jones, C., Landmesser, L., 1981. Pathway selection by embryonic chick motoneurons in an experimentally altered environment. Proc. R. Soc. Lond. B Biol. Sci. 214, 19–52.
Landmesser, L., 1978. The development of motor projection patterns in the chick hind limb. J. Physiol. 284, 391–414.
Landmesser, L.T., 2001. The acquisition of motoneuron subtype identity and motor circuit formation. Int. J. Dev. Neurosci. 19, 175–182.
Lettice, L.A., Hill, A.E., Devenney, P.S., Hill, R.E., 2008. Point mutations in a distant sonic hedgehog cis-regulator generate a variable regulatory output responsible for preaxial polydactyly. Hum. Mol. Genet. 17, 978–985.
Lopez-Rios, J., Duchesne, A., Speziale, D., Andrey, G., Peterson, K.A., Germann, P., Unal, E., Liu, J., Floriot, S., Barbey, S., et al., 2014. Attenuated sensing of SHH by Ptch1 underlies evolution of bovine limbs. Nature 511, 46–51.
Mehring, C., Akselrod, M., Bashford, L., Mace, M., Choi, H., Blüher, M., Buschhoff, A.-S., Pistohl, T., Salomon, R., Cheah, A., et al., 2019. Augmented manipulation ability in humans with six-fingered hands. Nat. Commun. 10, 2401.
Petit, F., Sears, K.E., Ahituv, N., 2017. Limb development: a paradigm of gene regulation. Nat. Rev. Genet. 18, 245–258.
Pickering, J., Wali, N., Towers, M., 2017. Transcriptional changes in chick wing bud polarization induced by retinoic acid. Dev. Dynam. 246, 682–690.
Preibisch, S., Saalfeld, S., Tomancak, P., 2009. Globally optimal stitching of tiled 3D microscopic image acquisitions. Bioinformatics 25, 1463–1465.
Richardson, M.K., Chipman, A.D., 2003. Developmental constraints in a comparative framework: a test case using variations in phalanx number during amniote evolution. J. Exp. Zool. B Mol. Dev. Evol. 296B, 8–22.
Ros, M.A., Kay Simandl, B., Clark, A.W., Fallon, J.F., 2000. Methods for manipulating the chick limb bud to study gene expression, tissue interactions, and patterning. In: Tuan, R.S., Lo, C.W. (Eds.), Developmental Biology Protocols. Humana Press, Totowa, NJ, pp. 245–266.
Ruegg, M.A., Stoeckli, E.T., Kuhn, T.B., Heller, M., Zuellig, R., Sonderegger, P., 1989. Purification of axonin-1, a protein that is secreted from axons during neurogenesis. EMBO J. 8, 55–63.
Schindelin, J., Arganda-Carreras, I., Frise, E., Kaynig, V., Longair, M., Pietzsch, T., Preibisch, S., Rueden, C., Saalfeld, S., Schmid, B., et al., 2012. Fiji - an Open Source platform for biological image analysis. Nat. Methods 9.
Schramm, C., Solursh, M., 1990. The formation of premuscle masses during chick wing bud development. Anat. Embryol. 182, 235–247.
Schweitzer, R., Zelzer, E., Volk, T., 2010. Connecting muscles to tendons: tendons and musculoskeletal development in flies and vertebrates. Development 137, 2807–2817.
Shapiro, M.D., Hanken, J., Rosenthal, N., 2003. Developmental basis of evolutionary digit loss in the Australian lizard Hemiergis. J. Exp. Zool. B Mol. Dev. Evol. 297, 48–56.
Sharir, A., Stern, T., Rot, C., Shahar, R., Zelzer, E., 2011. Muscle force regulates bone shaping for optimal load-bearing capacity during embryogenesis. Development 138, 3247–3259.
Shubin, N., Tabin, C., Carroll, S., 1997. Fossils, genes and the evolution of animal limbs. Nature 388, 639.
Stirling, R.V., Summerbell, D., 1988. Specific guidance of motor axons to duplicated muscles in the developing amniote limb. Development 103, 97–110.
Sullivan, G., 1962. Anatomy and embryology of the Wing Musculature of the domestic fowl (gallus). Aust. J. Zool. 10, 458.
Susaki, E.A., Tainaka, K., Perrin, D., Kishino, F., Tawara, T., Watanabe, T.M., Yokoyama, C., Onoe, H., Eguchi, M., Yamaguchi, S., et al., 2014. Whole-Brain imaging with single-cell resolution using chemical cocktails and computational analysis. Cell 157, 726–739.
Susaki, E.A., Tainaka, K., Perrin, D., Yukinaga, H., Kuno, A., Ueda, H.R., 2015. Advanced CUBIC protocols for whole-brain and whole-body clearing and imaging. Nat. Protoc. 10, 1709–1727.
Suzuki, T., 2013. How is digit identity determined during limb development? Dev. Growth Differ. 55, 130–138.
Tickle, C., Towers, M., 2017. Sonic hedgehog signaling in limb development. Front. Cell Dev. Biol. 5.
Tickle, C., Alberts, B., Wolpert, L., Lee, J., 1982. Local application of retinoic acid to the limb bond mimics the action of the polarizing region. Nature 296, 564–566.
Tickle, C., Lee, J., Eichele, G., 1985. A quantitative analysis of the effect of all-trans-retinoic acid on the pattern of chick wing development. Dev. Biol. 109, 82–95.
Tschopp, P., Sherratt, E., Sanger, T.J., Groner, A.C., Aspiras, A.C., Hu, J.K., Pourquié, O., Gros, J., Tabin, C.J., 2014. A relative shift in cloacal location repositions external genitalia in amniote evolution. Nature 516, 391–394.
Vallecillo-García, P., Orgeur, M., Hofe-Schneider, S. vom, Stumm, J., Kappert, V., Ibrahim, D.M., Börno, S.T., Hayashi, S., Relaix, F., Hildebrandt, K., et al., 2017. Odd skipped-related 1 identifies a population of embryonic fibro-adipogenic progenitors regulating myogenesis during limb development. Nat. Commun. 8, 1218.
Wagner, G.P., 2014. Homology, Genes, and Evolutionary Innovation. Princeton University Press.
Wagner, G.P., Chiu, C.H., 2001. The tetrapod limb: a hypothesis on its origin. J. Exp. Zool. 291, 226–240.
Wimsatt, W., 2012. Biology of Bats. Elsevier.
Young, N.M., Hallgrímsson, B., 2005. Serial homology and the evolution of mammalian limb covariation structure. Evolution 59, 2691–2704.
Zeller, R., López-Ríos, J., Zuniga, A., 2009. Vertebrate limb bud development: moving towards integrative analysis of organogenesis. Nat. Rev. Genet. 10, 845–858.
Zuniga, A., 2015. Next generation limb development and evolution: old questions, new perspectives. Development 142, 3810–3820.

Received: 21 April 2022 | Revised: 7 June 2022 | Accepted: 8 June 2022

DOI: 10.1002/dvdy.507

TECHNIQUES

Developmental Dynamics WILEY

A method to investigate muscle target-specific transcriptional signatures of single motor neurons

Bianka Berki | **Fabio Sacher** | **Antoine Fages** | **Patrick Tschopp** | **Maëva Luxey**

DUW Zoology, University of Basel, Basel, Switzerland

Correspondence
Maëva Luxey, DUW Zoology, University of Basel, Vesalgasse 1, CH-4051, Basel, Switzerland.
Email: maeva.luxey@unibas.ch

Funding information
Forschungsfonds of the University of Basel; Schweizerischer Nationalfonds zur Förderung der Wissenschaftlichen Forschung, Grant/Award Number: 31003A_170022; Stiftung für die Erforschung der Muskelkrankheiten; Universität Basel; Swiss National Science Foundation; *Olga Mayenfisch Stiftung*

Abstract

Background: Motor neurons in the vertebrate spinal cord have long served as a paradigm to study the transcriptional logic of cell type specification and differentiation. At limb levels, pool-specific transcriptional signatures first restrict innervation to only one particular muscle in the periphery, and get refined, once muscle connection has been established. Accordingly, to study the transcriptional dynamics and specificity of the system, a method for establishing muscle target-specific motor neuron transcriptomes would be required.

Results: To investigate target-specific transcriptional signatures of single motor neurons, here we combine ex-ovo retrograde axonal labeling in mid-gestation chicken embryos with manual isolation of individual fluorescent cells and Smart-seq2 single-cell RNA-sequencing. We validate our method by injecting the dorsal *extensor metacarpi radialis* and ventral *flexor digiti quarti* wing muscles and harvesting a total of 50 fluorescently labeled cells, in which we detect up to 12,000 transcribed genes. Additionally, we present visual cues and cDNA metrics predictive of sequencing success.

Conclusions: Our method provides a unique approach to study muscle target-specific motor neuron transcriptomes at a single-cell resolution. We anticipate that our method will provide key insights into the transcriptional logic underlying motor neuron pool specialization and proper neuromuscular circuit assembly and refinement.

KEYWORDS

axonal backfill, limb motor neuron-muscle connection, manual cell picking, neural tube dissociation, single motor neuron sequencing, Smart-seq2

1 | INTRODUCTION

During Metazoan development, a multitude of various cell types need to be specified to ensure proper functioning of the body. The central nervous system represents one prime example of this emergent cellular complexity. Indeed, in vertebrates, the spinal cord is composed of a high number of molecularly distinct cell

types, interconnected with each other and also with their target organs.[1]

In this context, limb innervating spinal motor neurons are particularly interesting. During their maturation, they go through a series of sub-differentiation steps after which their molecular footprint directly reflects the affinity of their axons toward one particular muscle in the limb periphery.[2,3] They first gain lateral motor column (LMC) identity at the levels of the limb, and thereafter split into lateral and medial LMCs, to ensure dorsal and ventral limb innervation, respectively. Subsequently, they subdivide into so-called motor neuron pools that are spatially segregated from one another, and represent transcriptionally unique sets of neurons innervating one specific muscle.[4-6] To date, only few motoneuron pool-specific genes have been identified, and our knowledge of the developmental specification and muscle target-induced refinement of pool-specific transcriptomes remains incomplete.

The recent development and commercialization of emulsion-based single-cell RNA-sequencing technologies have greatly contributed to our understanding of spinal neuronal subtype specification during development, as well as their distinct molecular signatures in adult individuals.[7-11] However, studying motor neuron pool diversification with these high-throughput methods remains difficult, due to tissue dissociation-induced loss of spatial information and more importantly muscle target-connectivity.[12] Moreover, despite recent studies aiming to account for target connectivity in a high throughput manner,[13-16] the need for a more specific and user-defined method to purify single motor neurons from a given pool, still connected to their cognate muscle within an embryonic time-frame, becomes apparent to study target-specific neuronal transcriptomes with appropriate resolution.

Retrograde axonal labeling has long been used to map the connection between target muscles and the position of the corresponding motor neuron cell bodies in the spinal cord.[17-19] This method consists of injecting a tracer molecule into the target muscle of choice, and let it be transported to the soma of the connected motor neurons in the spinal cord. This method has successfully been applied to create topological maps of limb muscle innervation in chicken embryos.[17,20] Unfortunately, the low number of labeled cell bodies resulting from this method makes the FACS-based (fluorescent-activated cell sorting) isolation of those cells for transcriptional profiling almost impossible. Alternatively, laser-capture microscopy has been used to excise labeled cells from sections of the spinal cord, yet this method does not result in single-cell resolution transcriptomes.[21]

Here, we present an optimized workflow combining ex-ovo fluorescent retrograde axonal labeling followed by manual cell selection, to investigate the transcriptomic signatures of individual motor neurons connected to a specific peripheral muscle target (Figure 1). Our protocol provides details on optimal culture conditions for mid-gestation chicken embryos, focal injection into a single peripheral muscle, spinal cord dissociation, manual purification, and visual inspection of fluorescent cells from plated neurons followed by the highly sensitive Smart-seq2 single-cell RNA-sequencing. As a proof of principle, we purify motor neurons from the pools innervating the *extensor metacarpi radialis* (EMR) and *flexor digiti quarti* (FDQ), two muscles on opposite extremes along with the three axes of the limb, that is, dorso-ventral, proximo-distal, and antero-posterior. In total, we isolate 50 purified EMR- and FDQ-connected cells that were sequenced following the Smart-seq2 protocol.[22] After assessing the overall quality of the cellular transcriptomes and filtering based on the expression levels of mitochondrial genes as an indicator of cellular stress, we reliably detect—in cells with satisfying cDNA profiles—the expression of 8000 to 12,000 genes per cellular transcriptome, including several motor neuron-specific markers.

Collectively, we present a method that provides transcriptomic data from muscle-specific embryonic motor neuron pools at single-cell resolution. Our method has the potential to provide key insights into the transcriptional status of forming motor neuron pools that are connecting to their cognate muscles. Moreover, our technique opens new avenues to elucidate the molecular crosstalk between nerves and muscles that underlies neuromuscular circuit establishment and refinement.

2 | EXPERIMENTAL PROCEDURES AND RESULTS

2.1 | Culture preparation

To set up the ex-ovo chicken embryo culture, we pre-warmed the DMEM/F-12 media (Gibco, without phenol red) at 37°C in a water bath. In the meantime, we connected a sandstone to an oxygen bottle and let it bubble for at least 10 min in autoclaved, deionized water, to wash off dust and other residues (Figure 2B). To prepare the culture dish for embryos, we poured the pre-warmed DMEM/F-12 media into a silicone-coated (SYLGARD) 15 cm Petri dish (Figure 2A). We placed the Petri dish under a heating lamp and used a thermometer to monitor the temperature, adjusting the height level of the lamp to reach and maintain a temperature between 33 and 35°C (Figure 2B). The cleaned sandstone was then

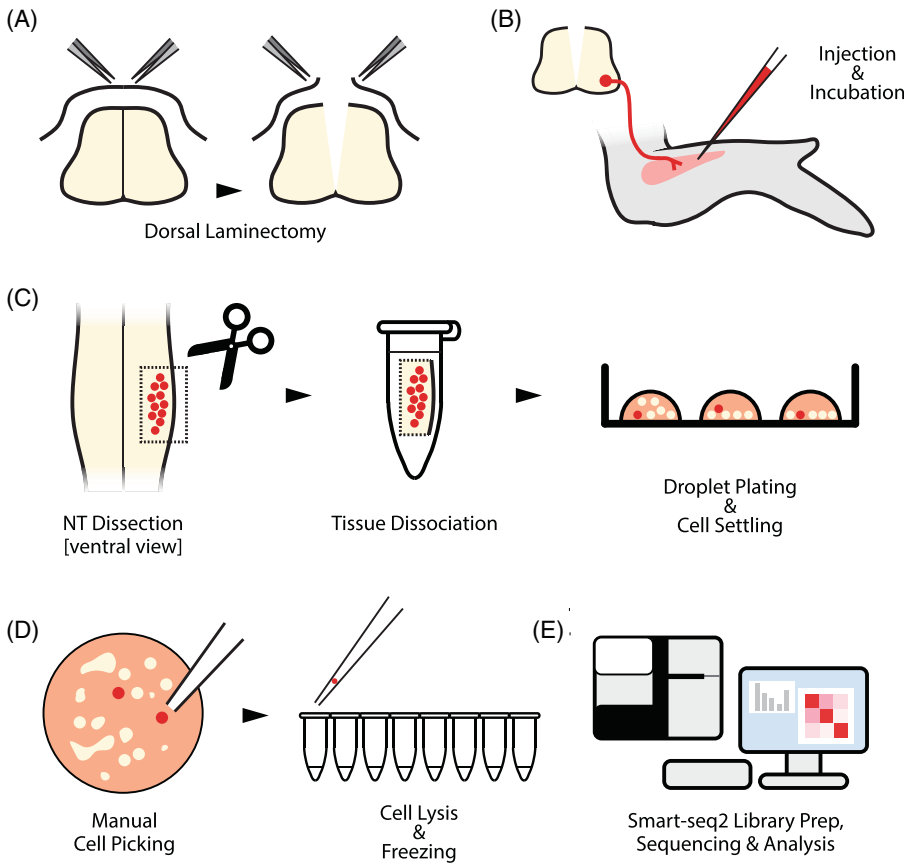

FIGURE 1 Complete workflow of the method. (A) Schematic representing the dorsal laminectomy to ensure good oxygenation of the spinal neurons. The dorsal part of the vertebra is removed, together with the opening of the roof plate. (B) A fluorescent tracer (eg, CTB-555) is injected into the target muscle and embryos are incubated for 5 hours in ex-ovo culture, allowing the fluorescent tracer to be transported to the soma of spiral motor neurons. (C) After backfill culturing, the neural tube is dissected. The success of retrograde tracing is assessed under stereomicroscope and fluorescent neural tissue is isolated. Following papain dissociation, the cells are resuspended and plated in Neurobasal plating media for subsequent manual purification. (D) Healthy-looking fluorescent cells are separated from debris and nonfluorescent cells by aspiration. Once the cells are washed in PBS, they are transferred into lysis buffer in a single tube of a PCR strip on ice. Lysed cells can be kept at −80°C until further processing. (E) Smart-seq2 libraries are prepared and sequenced, and the obtained cell transcriptomes are checked for overall quality and analyzed to detect the expression of specific marker genes

placed in the media and let to bubble thoroughly during the time of dissection and muscle injection.

2.2 | Embryo dissection and limb muscle injection

White Leghorn chicken eggs (*Gallus gallus*) were incubated at 38°C with 60% humidity for 9 days. We gently cracked the egg and poured the content into a glass dish. We then transferred the embryo into a PBS dish, in order to wash all the yolk off, decapitated the embryos, and put it into a black silicone-coated dish (Figure 2A). Ventral side down, we pinned the embryos to the dish by the neck and the tail and made a transversal cut of the spinal cord at the middle of the back, approximately at the level of the last pair of ribs. After checking the entire spinal cord was cut through, we then skinned the back to perform a dorsal laminectomy (Figure 1A). Indeed, at late embryonic stages, it is important to ensure proper oxygenation of spinal neurons. To do so, using forceps, we removed the dorsal part of the vertebra, starting from the caudal part up to the neck while making sure that the underlying spinal cord remains intact. Finally, with a fire-sharpened Tungsten needle, we opened the roof plate for better oxygenation of the ventral spinal neurons during the incubation period. Once the dorsal laminectomy was performed, the

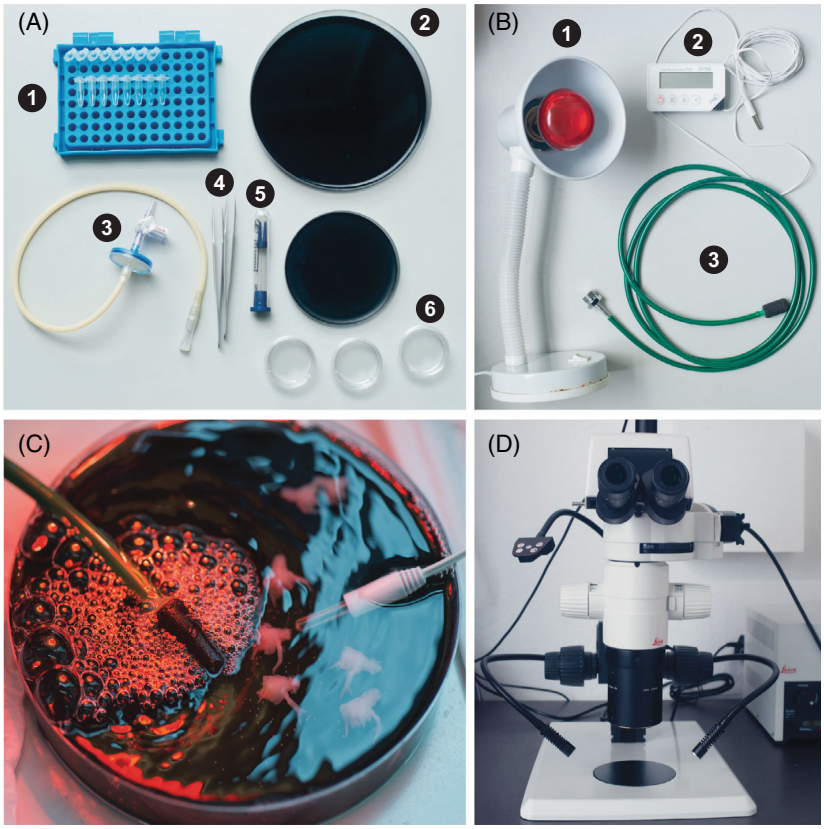

FIGURE 2 Inventory of tools and equipment required. (A) (1) PCR tubes, if possible, with individual lids (Eppendorf), (2) two black SYLGARD coated Petri dishes (10 cm and 15 cm), (3) mouth pipette with a syringe filter and valve to control the flow rate, (4) dissection forceps (FST size 55), (5) sterile micropipettes (ORIGIO MBB-FP-M-0), and (6) clear 6 cm Petri dishes for PBS washes. (B) (1) Heating lamp to maintain culture temperature, (2) thermometer, and (3) sandstone connected via a plastic tube and valve regulator to a pressurized oxygen bottle. (C) Image of embryos in culture during retrograde labeling experiment. The sandstone provides oxygenation, and the temperature is monitored during the entire incubation time. (D) Fluorescent stereomicroscope (Leica MZ10 F, with 1.6× ApoPlan lens, connected to a Leica EL6000 fluorescent light source) used for cell picking

lumbar part with the legs of the embryos could then be removed and discarded.

For limb muscle injection, we pinned the embryo on its side at the level of the neck for better visibility and accessibility of the wing muscles. In this proof of principle experiment, we decided to focus on the EMR and the FDQ, a dorsally and ventrally located wing muscles, respectively.[23,24] Without damaging the muscle bundles, we delicately skinned the forearm. Using a mouth pipette and pulled capillary, we injected a fluorescently labeled tracer molecule, Cholera Toxin Subunit B (CTB-555, 0.1 mg/mL in PBS, Invitrogen), into the target muscle, that is, the EMR or FDQ. If multiple injections are possible all along with the bigger muscle like the EMR, it is important to keep its structure intact and avoid leakage of the tracer into adjacent muscles (Figure 3A). However, a particular focus should be given to injections at the mid-section of the fusiform muscle, as most motor neuron axon termini contact the muscle there (Figure 3B).

After injection, we put the embryos in the previously oxygenated culture dish with pre-warmed DMEM/F-12 media and pinned them down (Figure 2C). During the 5 hours of incubation, we kept on monitoring the temperature, checked for proper oxygenation, and supplemented the dish with fresh, prewarmed media if needed, in order to keep the embryos submerged.

2.3 | Retrograde axonal labeling quality check

Once the incubation time was up, we closed the oxygen bottle and washed the sandstone in autoclaved water until the oxygen stopped running. To isolate the spinal cord, we pinned the embryos face down to a new silicone-coated Petri dish and gently pass closed forceps underneath the neural tube, to release it from its enclosing of the forming vertebrae. Special care had to be taken since the targeted motor neurons are located in the ventral horn, that is, directly above where the spinal cord was released from. The neural tube was pinned down with its ventral side up and inspected for successful backfill. To do so, we placed the dish under binoculars equipped with fluorescent lamps and adequate filters (Figure 2D). In case the axonal tracing was successful, we observed a fluorescent signal in the ventral horn of the spinal cord (Figure 3C). Under the scope, we microdissected only the fluorescent part of the neural tube

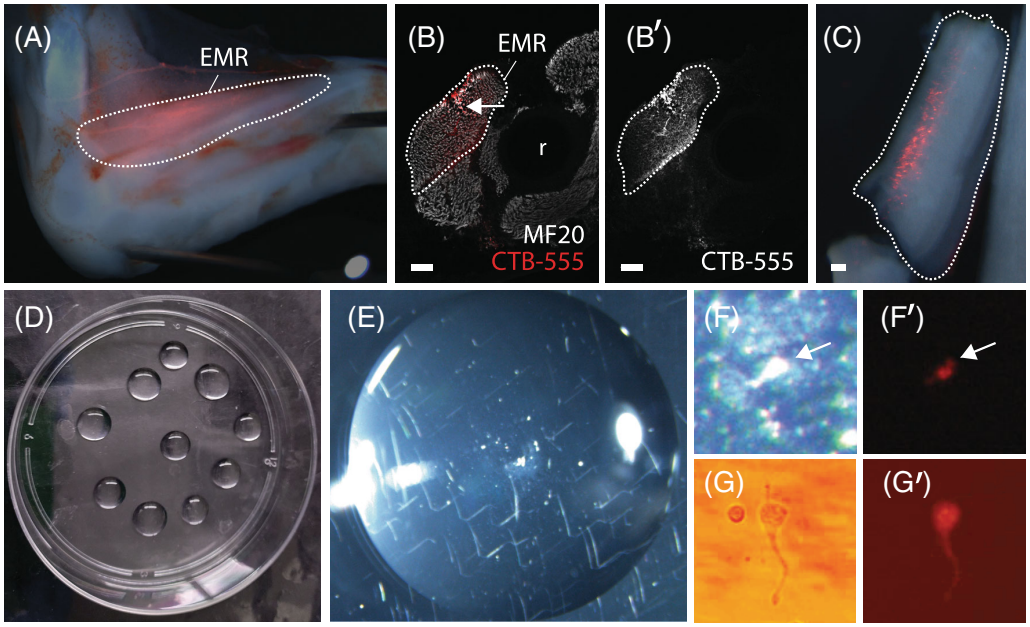

FIGURE 3 Retrograde labeling and EMR muscle injection quality check. (A) CTB-555 injection site in the EMR muscle. The white dotted line shows the extent of the muscle. (B) Transversal cross-section of an injected limb with muscles in gray (MF20). The white dotted line shows the EMR muscle and the white arrow points to deformities at the injection site, r for radius. (B′) Fluorescent image of the CTB-555 injection site in the EMR muscle with no signal in adjacent muscles. (C) Fluorescent signal in the ventral neural tube after retrograde labeling. The white dotted line shows the dissected portion of the neural tube. (D) The post-dissociation cell suspension is plated in drops. (E) Close-up image of a drop of cell suspension. Note that most of the cells are grouped in the middle of the drops. (F and F′) Bright field and fluorescent image of a red fluorescent plated cell. Note the concentration of cells and debris at this first stage of cell picking. The white arrow is showing a single labeled cell. (G and G′) Bright field and fluorescent image of a single isolated red fluorescent cell after several rounds of PBS washes. We can even observe the axon projection of the neuron

(Figure 3C) and placed it in a labeled 2 mL Eppendorf tube with PBS. As they might alter the efficiency of the tissue dissociation, we eliminated all residues present in the culture media by washing the dissected tissue twice with PBS. For an additional injection quality control, we dissected the injected limb, fixed it in PFA 4% overnight, and transversally sectioned it at the correct proximo-distal level, then stained it for Myosin heavy chain (MF20; 1:500, DSHB) to visualize proper CTB-555 injection inside of the targeted muscle (Figure 3B).

2.4 | Neural tube dissociation and cell plating

Neurons, and neuronal tissues in general, are particularly sensitive to tissue dissociation, especially after prolonged periods of ex-ovo incubation. Therefore, a mild papain dissociation method was performed, and dissociated cells were plated in a neuron-specific media (plating media: Neurobasal Gibco, 5% fetal bovine serum [FBS] and 1% GlutaMAX Gibco).[25] One hour and a half before the end of the incubation period required for axonal tracing, we put the Neurobasal plating media in a Petri dish inside a cell culture incubator for CO_2 equilibration. Additionally, half an hour before the end, we mixed FACSmax (Amsbio) dissociation media with papain (Roche) to get a 0.25 mg/mL final concentration of the enzyme. We pre-warmed the mix in a water bath at 37°C until the neural tube was completely dissected. For tissue trituration, we used a P1000 pipette and prepared for each sample the following filtered tips: one pipette cut close to the 250 µL mark, and a second one cut halfway between the 250 µL mark and the end of tip to have a smaller opening. Both pipette tips were flamed briefly, to soften the sharp edges. Additionally, we prepared two more uncut pipette tips for further trituration. After spraying them with ethanol, we placed them under the cell culture hood.

Once the desired piece of neural tissue was dissected, we discarded the PBS to add 1 mL of dissociation media per sample and put them in a water bath at 37°C for 10 minutes, combining it with a gentle flicking step after 5 minutes. With the first cut pipette tip, we triturated the tissue by gently pipetting 20 times up and down, and

then placed the sample back at 37°C for an additional 5 minutes. The last step was repeated with the second cut and the uncut pipette tips, until no visible tissue clumps remained present.

The samples were centrifuged at 300 × *g* for 7 minutes at room temperature. After discarding the supernatant, we resuspended the cell pellet in 600 µL of plating media. Typically, the dissociation of a single spinal cord only gave a small number of cells (around 300,000 cells/mL, with a cell viability of about 90%, as evaluated by Cellometer [Nextcelom Bioscience]). Plating of single drop of ~150 µL of cell suspensions in a bigger Petri dish provided a higher concentration of cells per surface area than covering the entire dish with the cell suspension (Figure 3D). This substantially facilitated the detection and manual purification of fluorescent cells afterwards. We deposited the cell suspension drops in a 10 cm Petri dish and placed them in a cell culture incubator for at least 30 minutes, so that cells had time to settle at the bottom of the drops (Figure 3D,E).

2.5 | Manual cell isolation

First, we prepared the workspace for cell selection and picking, by cleaning all surfaces, instruments, and tools with RNAseZap RNAse inhibitor (Invitrogen). As the plating media contain FBS, which may alter the cell lysis process, picked cells must be washed at least twice in clean, cold PBS before depositing them into the lysis buffer. For these washing steps, we first prepared at least three 3 cm Petri dishes right before proceeding with the cell picking. The dishes and the upturned lids were filled with ice-cold PBS. The first Petri dish was then used to fill the capillary with clean PBS, the second one to eject any liquid between picked cells, and the third one to quickly wash the needle (Figure 2A). The PBS-filled lids were used to wash the picked cells as they are shallower and therefore more convenient to pass from one to the other.

To prepare the cellular extracts for Smart-seq2 single-cell RNA-sequencing, we used a cell lysis buffer compatible with this workflow (0.2% (vol/vol) Triton X-100 and 2 U/µL RNase inhibitor).[22] In labeled PCR strips, we put 2.3 µL of lysis buffer in each tube and kept the buffer cooled before and during the experiment on a metal cooling rack on ice.

We assembled the cell aspirator, consisting of a three-way stopcock, a 0.3 µm syringe filter, a cell aspirator tube, and sterile micropipette (Origio, MBB-FP-M-0), and made sure that all seals were tight (Figure 2A). To check if there were no leaks of air and the liquid was properly entering, we put the sterile capillary at the end of the cell aspirator and aspirated PBS. If a leakage of air was observed, we used paraffin sheets and changed the filter, whenever necessary.

When the set-up was ready, we screened the drops of cell suspension under a fluorescent stereomicroscope and roughly approximated the total number of fluorescent cells. We first took up clean PBS into the needle, to reduce capillary action and have improved control over the suction flow. We then aspirated the targeted fluorescent cells spotted in the cell suspension (Figure 3E,F-F'). At this stage, the isolation of a unique cell of interest is almost impossible. Thus, several rounds of PBS washes are required, in order to ensure the transfer of individual cells into the lysis buffer-filled PCR strips. First, we gently ejected the content of the needle into a PBS-filled Petri dish lid. For this, the focus of the binocular was properly adjusted, and to avoid the cells floating out of the field of vision, the ejection was carried out very slowly. After checking for the presence of the fluorescent cell by turning off the bright field light source, we washed the capillary needle, then re-aspirated the neuron with as few other, nonfluorescent cells as possible. We repeated the previous steps and blew clean PBS around the CTB-555-positive cell, in order to wash away any remaining cells and debris from its surroundings. These washing steps must be repeated as much as needed, using the 3 cm Petri dishes and their upturned lids previously filled with ice-cold PBS, until a single cell is obtained in a completely isolated fashion. A final check should be carried out, with both bright field and fluorescent light sources. Finally, we washed the capillary with PBS again and we aspirated a unique target cell and put it into a PCR stripe tube containing the lysis buffer.

We repeated the process of cell picking until there were no fluorescent cells left in the drops. It is important to note down any observations about the individual picked cells, for example, their shape, relative size to other cells, and fluorescence intensity. All those parameters will be considered, when deciding which resulting cDNA samples will eventually be selected for the following library preparation and sequencing steps. A good example of a healthy-looking motor neuron, with its axon still visible, is shown in Figure 3G-G'. The PCR stripes were then stored at −80°C, until cDNA production and subsequent library preparation.

2.6 | Library preparation, sequencing, and representative results

After reverse transcription (Superscript II) and amplification (Invitrogen), each individual cDNA sample was loaded onto a Fragment Analyzer (Agilent) for quality

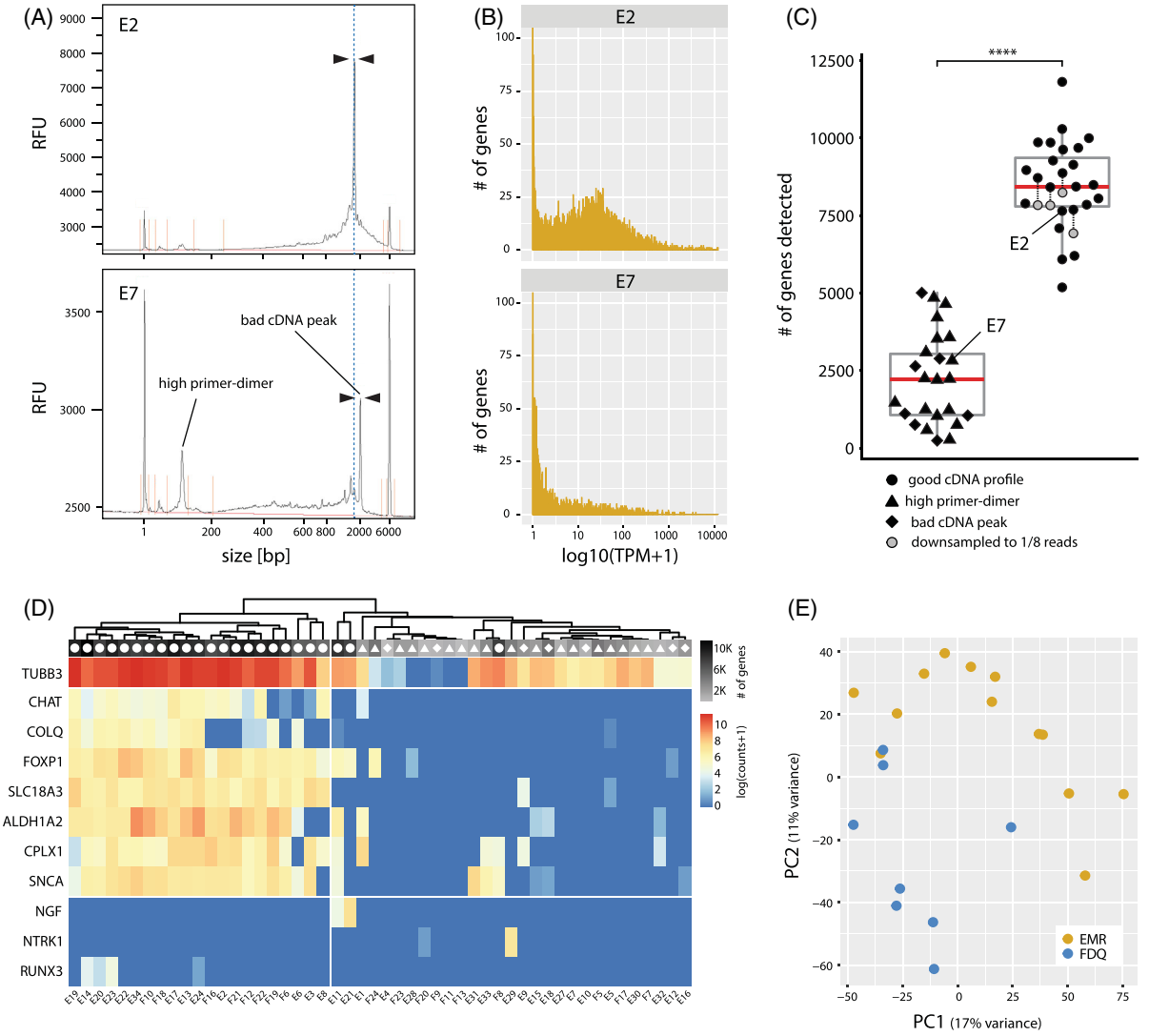

FIGURE 4 Representative results of individual neuron sequencing. (A) Fragment Analyzer cDNA profiles of two individual cells (E2 and E7). The top panel shows the profile of a high-quality cell, with a main peak around 1650 to 1700 bp (black arrowheads, approximately 8000 RFUs).The bottom panel shows the profile of a low-quality cell with the main peak fainter shifted toward 2000 bp (black arrowheads, 3000 RFUs) and the relative primer-dimer concentration is higher. (B) TPM (transcript per million) distribution in a high-quality cell (E2) and low-quality cell (E7). (C) Box plot representing the number of genes detected per sample. Different quality assessments of cDNA profiles are represented by different geometric shapes (circles, triangles, and diamonds). Samples with a good cDNA profile show a significantly higher number of genes detected (Wilcoxon rank sum test, $P < .0001$). (D) Heat map of selected marker transcript numbers. Cells are grouped by unsupervised hierarchical clustering (muscle connectivity labeled by E: EMR and F: FDQ). The overall number of genes detected per cell is indicated by grayscale, and the quality of their cDNA profiles by different geometric shapes (see legend of panel C). (E) Principal component analysis (PCA) of gene expression levels of motor neurons innervating EMR and FDQ, based on the top 500 most variably expressed genes

assessment. Genomic libraries were then prepared from selected cDNA samples using an Illumina Nextera XT kit. All libraries were sequenced on an Illumina Novaseq 6000 SP Sequencer (100 cycles, 50 bp paired-end reads), to a depth of 2.5 to 21.3 million reads per sample. The raw reads were trimmed with Trimmomatic (v.0.39), using the Illuminaclip parameter with the distributed Nextera adapter file, aligned with STAR (v.2.5.2) to the GRCg6a chicken genome, and count tables were created with HTSeq (v.0.6.1).[26-28]

Retrospectively, with the sequencing results of our proof-of-principle experiment at hand, we were able to define cDNA quality metrics that were predictive of sequencing success. Namely, to assess Fragment Analyzer cDNA profile as a potential predictor of expected gene expression library complexity, we correlated the presence/absence of a "bad cDNA peak" and/or "high primer-dimer" content (Figure 4A) with the overall number of genes detected, and their expression level distribution (Figure 4B,C). For example, good-quality cells like sample "E2" were characterized by a cDNA profile containing an overall high peak between 1.6 and 1.7 kb (full-length transcripts), and a small number of fragments below 500 bp. Moreover, only a small peak of primer dimers around 100 bp was visible (Figure 4A, top panel). Contrary to this, in cells yielding low quality transcriptomes like sample "E7" (see Figure 4B,C), a substantially weaker main peak was detected (~3000 Relative Fluorescent Units [RFUs] for "E7" vs ~8000 RFUs for "E2"), reflecting overall lower RNA concentration, and the peak was shifted toward 2 kb (Figure 4A, see blue dotted line for reference). Furthermore, a higher primer-dimer peak was detected in those cells (Figure 4A, bottom panel). After sequencing and transcript quantification, cells with a good cDNA profile presented a bimodal distribution of individual gene expression levels, whereas poor cDNA profiles resulted in a post-sequencing transcript level distribution skewed toward zero (Figure 4B, compare top graph for sample "E2" to bottom one for sample "E7"). Moreover, an overall significantly higher number of genes was detected (8000-12,000 genes) in cells presenting a good cDNA profile, even after down-sampling the number of reads per sample to 1/8 of the original count (Figure 4C, grey circles). However, some samples presented a more puzzling cDNA profile, showing an overall decent cDNA profile—according to the previously defined criteria—but with a slightly more pronounced proportion of shorter fragments (<700 bp) indicative of RNA degradation. Post sequencing, we detected mostly mitochondrial gene transcripts at a high level in these cells, but low expression levels for most other genes. These results thus convinced us that the amount of small (below 500 bp) must also be considered as a criterion, in addition to cDNA peak height and position, and primer-dimer content. In summary, Fragment Analyzer cDNA profiles are a reliable predictor of the number of genes detected after sequencing, which are key indicators of transcriptome information content. As such, a sample selection step based on Fragment Analyzer cDNA profiles before library preparation and sequencing can maximize information gain and reduce overall costs, to streamline the overall efficiency of our experimental workflow.

In order to validate the identity of the sequenced cells as motor neurons, a number of marker gene expression profiles were examined using an expression heatmap plot and unsupervised hierarchical clustering (Figure 4D). Almost all cells expressed the general neuronal differentiation marker *TUBB3* (*TUJ1*). However, cells of the left-most cluster showed a higher transcript count for *TUBB3*, and an overall higher number of genes detected than for the other cluster (greyscale, above). Interestingly, the majority of cells (21 out of the 24) presenting a good cDNA profile, expressed Choline Acetyltransferase (*CHAT*), Acetylcholinesterase subunit Q (*COLQ*), and Vesicular Acetylcholine Transporter (*SLC18A3*), three gene members of the biosynthesis and transport chain of the motor neuron-specific neurotransmitter acetylcholine.[29] *CPLX1* and *SCNA*, both known to be involved in the modulation of neurotransmitter action and implicated in motor neuron diseases were also expressed by these cells.[30,31] Furthermore, the cells also expressed *FOXP1* and *ALDH1A2*, two well-known embryonic marker genes of developing LMC motor neurons (left most cluster in Figure 4D).[32,33] To exclude the possibility of contamination by dorsal root ganglia cells, which are also labeled during axonal backfill procedures, we additionally checked for the expression of sensory neuron marker genes. As expected, none of the sequenced cells did express any sensory neuron markers like *NGF*, *NTRK1*, or *RUNX3*[34,35] at substantial levels, thereby validating our micro-dissection procedure and the fact that the purified cells indeed represent motor neurons coming from the ventral part of the neural tube.

Finally, to assess the ability of our method to transcriptionally differentiate closely related motor neuron subtypes, we compared our data sets of motor neurons connected to two different muscles, the EMR and FDQ, using principal component analysis (PCA) of levels of gene expression. PCA was performed with zinbwave (v.1.12.0) and DESeq2 (v.1.30.0),[36,37] following the respective vignettes' suggestions concerning data transformation and normalization, and using the top 500 most variably expressed genes. On the resulting PCA plot, cellular transcriptomes coming from motor neurons with the same muscle connection appear to cluster together, with a striking separation between the EMR and FDQ motor neuron subsets (Figure 4E). This result demonstrates that our method can reliably detect even minor transcriptional profile differences between closely related motor neuron subsets, which reflects their axonal connections to distinct muscle groups.

Collectively, the following criteria should thus be taken into account, when deciding which cDNA samples to include for library preparation and sequencing, as well as downstream bioinformatics analyses: (1) high cDNA

concentration (>5 μg/μL), with a cDNA profile peak at a size of 1.5 to 1.7 kb and a low proportion of short fragments and primer-dimers; (2) less than ∼50% of mitochondrial gene transcripts per cell; (3) more than 6000 genes detected per cell; (4) expression of motor neuron markers such as *CHAT*, *SLC18A3*, *FOXP1*; and (5) absence of sensory neuron markers expression like, for example, *NGF*, *NTRK1*, and *RUNX3*. Samples meeting all these criteria should generally provide robust and reliable information on the transcriptome of motor neurons connected to a particular muscle group, although certain samples meeting only some of the criteria above might be also considered, on a case-by-case basis, to determine whether their inclusion into further analyses is reasonable.

3 | DISCUSSION AND CONCLUSION

Here, we present a method that successfully combines the classical experimental embryology technique of retrograde axonal tracing with state-of-the-art single-cell RNA-sequencing technology of individual motor neurons, in order to investigate motor neuron pool- and muscle target-specific transcriptomes at individual cell resolution. Our procedure proved efficient not only in detecting motor neuron specific marker gene expression profiles in EMR- and FDQ-connected cells, but also in correlating their respective cDNA metrics to the eventual expected transcriptome quality. Importantly, this procedure can also be used to compare other set of neurons innervating various muscle targets located in different parts of the embryo.

Ex-ovo manipulation and culturing of chicken embryos can be performed more easily at earlier stages (ie, before Hamburger-Hamilton stage HH34, or embryonic day 8) without the need for invasive surgery. The transcriptional logic of the early dorsal-ventral choice point could thereby already be addressed via the dorsal or ventral retrograde labeling of axonal projections. Unfortunately, muscle-specific resolution cannot be achieved at these early stages of muscle formation, due to the absence of fully individualized muscle bundles. For mid-gestation chicken embryos (ie, between Hamburger-Hamilton stage HH34 and HH36, or embryonic day 8 and day 10, when individual muscle bundles have formed), our culture conditions required the optimization of various parameters. Indeed, retrograde axonal labeling at limb levels is influenced by multiple factors, such as the age of the embryo, the size of the muscle, and its position along the proximo-distal axis of the developing limb. Later stage embryos are more difficult to culture, due to their increased size, the reduced diffusion rates to the targeted motor neurons, the formation of vertebral cartilage, and the thickening of the skin. Previous studies described ex-ovo retrograde labeling methods using the more difficult ventral laminectomy which involves the evisceration of the embryo and the detachment of the ventral part of the vertebra.[17] However, this type of anatomical surgery only seems necessary for embryo culture experiments that go beyond day 10 (stage HH36). In this case, an in-ovo approach should also be considered. Owing to the constrained accessibility of the anterior body part—which is due to the turning of the chick embryo, these studies would likely have to be restricted to the muscles of the hindlimb.[38] In our study, we propose to use a less invasive technique, the dorsal laminectomy, allowing us to preserve as much as possible the ventral part of the neural tube while ensuring better oxygenation of the tissue, motor neuron survival, and thereby making a successful axonal tracing more likely. Since the emergence of the retrograde labeling technique in the 1970s in chicken, they have also been extended to mouse embryos, to study neuronal connections at mid-gestation (around 12 days of development). Our study raises the intriguing possibility that the optimized protocol for culturing embryos at later stages could also allow for a transfer of retrograde labeling to later-stage mouse embryology studies.

The overall success of our retrograde labeling method also depends on the target to be injected, and the axonal distance to the neuron cell bodies. Comparing our test studies on the proximal EMR and the distal FDQ muscles, we noticed that smaller and more distally located limb muscles, such as the autopodial FDQ, are far more difficult to properly inject because of their size and elongated shape. Moreover, retrograde transport also becomes less reliable, due to the increased distance between the injected muscle and its connected motoneurons. Indeed, we observed a lower number of fluorescently labeled cells with the smaller and more distal muscles compared to the bigger, domed, and proximal ones. These observations suggest that the number of retrograde labeling experiments would have to be increased, in order to successfully pick a decent number of cells connected to the more distally located and smaller muscle groups and other systems. However, as shown in Figure 4, we were still able to reliably backfill and trace the axons of both subsets of motor neurons, connecting either to the larger, proximally located EMR muscle, as well as for the thinner, distally located FDQ muscle.

The handling of single cells, in order to reliably pick them as individual entities, can appear difficult. Indeed, multiple rounds of successive washes in PBS have proved critical to ensure the picking of single cells. For future

users, generic fluorescent cell markers such as BioTracker dyes (Sigma-Aldrich), labeling cell membrane, or Sytox (Invitrogen), indicating dead cells, might be an option to consider, in order to help the experimenter visualize all cells, and differentiate them from the retrograde-labeled ones. Alternatively, the use of the ubiquitous GFP transgenic lines could be considered.[39,40]

Overall, in our test data set, only 21 of 50 cellular transcriptomes (42%) could unequivocally be identified as originating from motor neurons, based on their gene expression signatures related to the cholinergic pathway and other motor neuron marker genes. However, with our retrospective analysis of cDNA profiles and resultant transcriptome quality, we now have a unique checklist of cDNA quality metrics for future studies. This checklist allows the interested researcher to only select samples whose cDNA profiles pass these criteria to proceed with library preparation and sequencing. For example, from the 50 cDNA profiles generated in this study, only 24 would now be deemed of sufficient quality for library preparation and sequencing (see circles, Figure 4C,D), thereby increasing the percentage of successful motor neuron transcriptomes obtained from 42% to 88% (21 of 24). Nevertheless, the aforementioned percentages can still be considered as a rough guideline for experimental design, when determining the overall number of cells to be purified to obtain a certain number of high-quality cDNA profiles and, by extension, single motor neuron transcriptomes.

Finally, in the era of single-cell sequencing, it has become essential for neurobiologists not only to study the transcriptomes of individual motor neurons, but also to correlate these molecular signatures with their eventual axonal projection patterns. To do so, techniques combining single-cell sequencing with retrograde labeling have already been developed in recent years, in order to decipher the transcriptional logic of neuronal wiring. Most of these studies, however, were performed in early postnatal or adult mice, using virus or CTB injections.[41-44] While these approaches do offer superior labeling efficiency compared to our method and—by extension—higher expected cell numbers, they do so at the expense of temporal resolution. Moreover, they only allow for the probing of developmental time points at which the wiring architecture of neuromuscular circuits has already been well established. Our method presented here opens the possibility to study the dynamics of the system at finer temporal resolution and at much earlier developmental time points, when individualized muscle bundles are just about to establish their connections with incoming motor neuron axons. As such, it will likely help to uncover motor neuron transcriptome signatures relevant for early neuromuscular circuit formation, as well as probe the potential plasticity within the system following pharmacological, genetic, or embryological manipulations.[24,44]

In conclusion, here we present an experimental workflow to investigate muscle target-specific transcriptional signatures of single motor neurons. Through the combination of axonal backfilling with individual cell picking and Smart-seq2 single-cell RNA-sequencing, we demonstrate its ability to generate high-quality transcriptomes of single motor neurons in a pool-specific manner, with known target muscle connectivity. Importantly, by combining it with transcriptional profiling of other involved tissue types, for example, muscles, data produced with our approach may lay the foundation for a comprehensive and integrative understanding of the transcriptional logic underlying motor neuron cell type specification and differentiation, as well as neuromuscular circuit assembly and refinement.

AUTHOR CONTRIBUTIONS

Bianka Berki: Conceptualization (equal); formal analysis (equal); investigation (equal); methodology (equal); validation (equal); visualization (equal); writing – original draft (equal); writing – review and editing (equal). **Fabio Sacher:** Data curation (equal); formal analysis (equal); investigation (equal); methodology (equal); validation (equal); visualization (equal); writing – review and editing (equal). **Antoine Fages:** Formal analysis (equal); methodology (equal); validation (equal); visualization (equal); writing – review and editing (equal). **Patrick Tschopp:** Conceptualization (equal); data curation (equal); formal analysis (equal); funding acquisition (equal); investigation (equal); methodology (equal); project administration (equal); supervision (equal); validation (equal); visualization (equal); writing – review and editing (equal). **Maëva Luxey:** Conceptualization (equal); data curation (equal); formal analysis (equal); funding acquisition (equal); investigation (equal); methodology (equal); supervision (equal); validation (equal); visualization (equal); writing – original draft (equal); writing – review and editing (equal).

ACKNOWLEDGMENTS

The authors wish to thank Elodie Burcklen and Christian Beisel at the "Genomics Facility Basel" for help with library preparation and sequencing, and all members of our group for useful discussions. All calculations were performed at sciCORE (http://scicore.unibas.ch/), the scientific computing center at the Universität Basel. This work was supported by a grant of the *Forschungsfonds* of the Universität Basel to ML, and research funds from the *Olga Mayenfisch Stiftung*, the *Fondation Suisse de Recherche sur les Maladies Musculaires* (FSRMM), the Swiss National Science Foundation (SNSF project grant

31003A_170022), and the Universität Basel to PT. Open access funding provided by Universitat Basel.

DATA AVAILABILITY STATEMENT

Raw sequencing data are available under GEO accession number GSE203595.

ORCID

Patrick Tschopp https://orcid.org/0000-0001-7339-3990
Maëva Luxey https://orcid.org/0000-0003-2752-8756

REFERENCES

1. Sagner A, Briscoe J. Establishing neuronal diversity in the spinal cord: a time and a place. *Development*. 2019;146(22): dev182154. doi:10.1242/dev.182154
2. Arber S, Ladle DR, Lin JH, Frank E, Jessell TM. ETS gene Er81 controls the formation of functional connections between group Ia sensory afferents and motor neurons. *Cell*. 2000; 101(5):485-498. doi:10.1016/S0092-8674(00)80859-4
3. Dasen JS, Tice BC, Brenner-Morton S, Jessell TM. A Hox regulatory network establishes motor neuron pool identity and target-muscle connectivity. *Cell*. 2005;123(3):477-491. doi:10.1016/j.cell.2005.09.009
4. Price SR, De Marco Garcia NV, Ranscht B, Jessell TM. Regulation of motor neuron pool sorting by differential expression of type II cadherins. *Cell*. 2002;109(2):205-216. doi:10.1016/S0092-8674(02)00695-5
5. Price SR, Briscoe J. The generation and diversification of spinal motor neurons: signals and responses. *Mech Dev*. 2004;121(9): 1103-1115. doi:10.1016/j.mod.2004.04.019
6. Demireva EY, Shapiro LS, Jessell TM, Zampieri N. Motor neuron position and topographic order imposed by β- and γ-catenin activities. *Cell*. 2011;147(3):641-652. doi:10.1016/j.cell.2011.09.037
7. Delile J, Rayon T, Melchionda M, Edwards A, Briscoe J, Sagner A. Single cell transcriptomics reveals spatial and temporal dynamics of gene expression in the developing mouse spinal cord. *Development*. 2019;146(12):dev173807. doi:10.1242/dev.173807
8. Blum JA, Klemm S, Shadrach JL, et al. Single-cell transcriptomic analysis of the adult mouse spinal cord reveals molecular diversity of autonomic and skeletal motor neurons. *Nat Neurosci*. 2021;24(4):572-583. doi:10.1038/s41593-020-00795-0
9. Eze UC, Bhaduri A, Haeussler M, Nowakowski TJ, Kriegstein AR. Single-cell atlas of early human brain development highlights heterogeneity of human neuroepithelial cells and early radial glia. *Nat Neurosci*. 2021;24(4):584-594. doi:10.1038/s41593-020-00794-1
10. Rayon T, Maizels RJ, Barrington C, Briscoe J. Single-cell transcriptome profiling of the human developing spinal cord reveals a conserved genetic programme with human-specific features. *Development*. 2021;148(15):dev199711. doi:10.1242/dev.199711
11. Russ DE, Cross RBP, Li L, et al. A harmonized atlas of mouse spinal cord cell types and their spatial organization. *Nat Commun*. 2021;12(1):5722. doi:10.1038/s41467-021-25125-1
12. Blum JA, Gitler AD. Singling out motor neurons in the age of single-cell transcriptomics. *Trends Genet*. Forthcoming 2022. doi:10.1016/j.tig.2022.03.016
13. Kebschull JM, Garcia da Silva P, Reid AP, Peikon ID, Albeanu DF, Zador AM. High-throughput mapping of single-neuron projections by sequencing of barcoded RNA. *Neuron*. 2016;91(5):975-987. doi:10.1016/j.neuron.2016.07.036
14. Han Y, Kebschull JM, Campbell RAA, et al. The logic of single-cell projections from visual cortex. *Nature*. 2018;556(7699):51-56. doi:10.1038/nature26159
15. Hanchate NK, Lee EJ, Ellis A, et al. Connect-seq to superimpose molecular on anatomical neural circuit maps. *Proc Natl Acad Sci USA*. 2020;117(8):4375-4384. doi:10.1073/pnas.1912176117
16. Xu P, Peng J, Yuan T, et al. High-throughput mapping of single-cell molecular and projection architecture of neurons by retrograde barcoded labelling. 2021. doi:10.1101/2021.05.16.444258
17. Landmesser L. The development of motor projection patterns in the chick hind limb. *J Physiol*. 1978;284:391-414.
18. Hollyday M. Organization of motor pools in the chick lumbar lateral motor column. *J Comp Neurol*. 1980;194(1):143-170. doi:10.1002/cne.901940108
19. Hollyday M, Jacobson RD. Location of motor pools innervating chick wing. *J Comp Neurol*. 1990;302(3):575-588. doi:10.1002/cne.903020313
20. Lance-Jones C, Landmesser L, Kuffler SW. Pathway selection by chick lumbosacral motoneurons during normal development. *Proc R Soc Lond B Biol Sci*. 1981;214(1194):1-18. doi:10.1098/rspb.1981.0079
21. Mendelsohn AI, Dasen JS, Jessell TM. Divergent Hox coding and evasion of retinoid signaling specifies motor neurons innervating digit muscles. *Neuron*. 2017;93(4):792-805.e4. doi:10.1016/j.neuron.2017.01.017
22. Picelli S, Faridani OR, Björklund ÅK, Winberg G, Sagasser S, Sandberg R. Full-length RNA-seq from single cells using Smart-seq2. *Nat Protoc*. 2014;9(1):171-181. doi:10.1038/nprot.2014.006
23. Sullivan G. Anatomy and embryology of the Wing Musculature of the domestic fowl (*Gallus*). *Aust J Zool*. 1962;10(3):458-518. doi:10.1071/ZO9620458
24. Luxey M, Berki B, Heusermann W, Fischer S, Tschopp P. Development of the chick wing and leg neuromuscular systems and their plasticity in response to changes in digit numbers. *Dev Biol*. 2020;458(2):133-140. doi:10.1016/j.ydbio.2019.10.035
25. Langlois SD, Morin S, Yam PT, Charron F. Dissection and culture of commissural neurons from embryonic spinal cord. *J Vis Exp*. 2010;39:e1773. doi:10.3791/1773
26. Dobin A, Davis CA, Schlesinger F, et al. STAR: ultrafast universal RNA-seq aligner. *Bioinformatics*. 2013;29(1):15-21. doi:10.1093/bioinformatics/bts635
27. Bolger AM, Lohse M, Usadel B. Trimmomatic: a flexible trimmer for Illumina sequence data. *Bioinformatics*. 2014;30(15): 2114-2120. doi:10.1093/bioinformatics/btu170
28. Anders S, Pyl PT, Huber W. HTSeq—a python framework to work with high-throughput sequencing data. *Bioinformatics*. 2015;31(2):166-169. doi:10.1093/bioinformatics/btu638
29. Petrov KA, Proskurina SE, Krejci E. Cholinesterases in tripartite neuromuscular synapse. *Front Mol Neurosci*. 2021;14: 811220. doi:10.3389/fnmol.2021.811220
30. Drew CJG, Kyd RJ, Morton AJ. Complexin 1 knockout mice exhibit marked deficits in social behaviours but appear to be

cognitively normal. *Hum Mol Genet*. 2007;16(19):2288-2305. doi:10.1093/hmg/ddm181
31. Kline RA, Kaifer KA, Osman EY, et al. Comparison of independent screens on differentially vulnerable motor neurons reveals alpha-synuclein as a common modifier in motor neuron diseases. *PLoS Genet*. 2017;13(3):e1006680. doi:10.1371/journal.pgen.1006680
32. Dasen JS, De Camilli A, Wang B, Tucker PW, Jessell TM. Hox repertoires for motor neuron diversity and connectivity gated by a single accessory factor, FoxP1. *Cell*. 2008;134(2):304-316. doi:10.1016/j.cell.2008.06.019
33. Bonanomi D. Axon pathfinding for locomotion. *Semin Cell Dev Biol*. 2019;85:26-35. doi:10.1016/j.semcdb.2017.11.014
34. Faure L, Wang Y, Kastriti ME, et al. Single cell RNA sequencing identifies early diversity of sensory neurons forming via bipotential intermediates. *Nat Commun*. 2020;11(1):4175. doi:10.1038/s41467-020-17929-4
35. Wu H, Petitpré C, Fontanet P, et al. Distinct subtypes of proprioceptive dorsal root ganglion neurons regulate adaptive proprioception in mice. *Nat Commun*. 2021;12(1):1026. doi:10.1038/s41467-021-21173-9
36. Love MI, Huber W, Anders S. Moderated estimation of fold change and dispersion for RNA-seq data with DESeq2. *Genome Biol*. 2014;15(12):550. doi:10.1186/s13059-014-0550-8
37. Risso D, Perraudeau F, Gribkova S, Dudoit S, Vert JP. A general and flexible method for signal extraction from single-cell RNA-seq data. *Nat Commun*. 2018;9:284. doi:10.1038/s41467-017-02554-5
38. McGrew MJ, Sherman A, Ellard FM, et al. Efficient production of germline transgenic chickens using lentiviral vectors. *EMBO Rep*. 2004;5(7):728-733. doi:10.1038/sj.embor.7400171
39. Davey MG, Balic A, Rainger J, Sang HM, McGrew MJ. Illuminating the chicken model through genetic modification. *Int J Dev Biol*. 2018;62(1–2-3):257-264. doi:10.1387/ijdb.170323mm
40. Tasic B, Yao Z, Graybuck LT, et al. Shared and distinct transcriptomic cell types across neocortical areas. *Nature*. 2018;563(7729):72-78. doi:10.1038/s41586-018-0654-5
41. Golan N, Kauer S, Ehrlich DB, Ravindra N, Dijk D van, Cafferty WB. Single-cell transcriptional profiling of the adult corticospinal tract reveals forelimb and hindlimb molecular specialization. 2021. doi:10.1101/2021.06.02.446653
42. Baek M, Menon V, Jessell TM, Hantman AW, Dasen JS. Molecular logic of spinocerebellar tract neuron diversity and connectivity. *Cell Rep*. 2019;27(9):2620-2635.e4. doi:10.1016/j.celrep.2019.04.113
43. Zampieri N, Jessell TM, Murray AJ. Mapping sensory circuits by anterograde trans-synaptic transfer of recombinant rabies virus. *Neuron*. 2014;81(4):766-778. doi:10.1016/j.neuron.2013.12.033
44. Velten J, Gao X, Van Nierop Y, Sanchez P, et al. Single-cell RNA sequencing of motoneurons identifies regulators of synaptic wiring in *Drosophila* embryos. *Mol Syst Biol*. 2022;18(3):e10255. doi:10.15252/msb.202110255

How to cite this article: Berki B, Sacher F, Fages A, Tschopp P, Luxey M. A method to investigate muscle target-specific transcriptional signatures of single motor neurons. *Developmental Dynamics*. 2022;1-12. doi:10.1002/dvdy.507

References

1. Zhang, X., Shu, D., Li, Y. & Han, J. New sites of Chengjiang fossils: crucial windows on the Cambrian explosion. *Journal of the Geological Society* **158,** 211–218. ISSN: 0016-7649, 2041-479X (2001).
2. Forey, P. & Janvier, P. Agnathans and the origin of jawed vertebrates. *Nature* **361,** 129–134. ISSN: 0028-0836, 1476-4687 (1993).
3. Donoghue & Sansom. Origin and early evolution of vertebrate skeletonization. *Microscopy Research and Technique* **59,** 352–372. ISSN: 1097-0029 (2002).
4. Donoghue & Keating. Early vertebrate evolution. *Palaeontology* **57,** 879–893. ISSN: 1475-4983 (2014).
5. Betancur, R. *et al.* Phylogenetic classification of bony fishes. *BMC Evolutionary Biology* **17,** 162. ISSN: 1471-2148 (2017).
6. Lu, J., Giles, S., Friedman, M. & Zhu, M. A new stem sarcopterygian illuminates patterns of character evolution in early bony fishes. *Nature Communications* **8,** 1932. ISSN: 2041-1723 (Dec. 5, 2017).
7. Shubin, N., Daeschler, E. & Coates, M. The Early Evolution of the Tetrapod Humerus. *Science* **304,** 90–93. ISSN: 0036-8075, 1095-9203 (2004).
8. Stewart, T. A. *et al.* Fin ray patterns at the fin-to-limb transition. *Proceedings of the National Academy of Sciences* **117,** 1612–1620. ISSN: 0027-8424, 1091-6490 (2020).
9. Hirasawa, T. & Kuratani, S. Evolution of the muscular system in tetrapod limbs. *Zoological Letters* **4,** 27. ISSN: 2056-306X (Sept. 20, 2018).
10. Molnar, J. L., Diogo, R., Hutchinson, J. R. & Pierce, S. E. Reconstructing pectoral appendicular muscle anatomy in fossil fish and tetrapods over the fins-to-limbs transition. *Biological Reviews* **93,** 1077–1107. ISSN: 1469-185X (2018).
11. Mednikov, D. N. Urodelans, Ichthyostega and the origin of the tetrapod limb. *Paleontological Journal* **48,** 1092–1103. ISSN: 1555-6174 (2014).
12. Säve-Söderbergh. Preliminary note on Devonian Stegocephalians from East Greenland. By G. Säve-Söderbergh. Meddelelser om Grønland, Bd. 94, Nr. 7, 1932. pp. 1–105, 22 text-figures, 22 pls. Price, Kr. 8·00. *Geological Magazine* **70,** 138–139. ISSN: 1469-5081, 0016-7568 (Mar. 1933).
13. Jarvik, E. & Danske. *On the fish-like tail in the ichthyostegid stegocephalians: with descriptions of a new stegocephalian and a new crossopterygian from the Upper Devonian of east Greenland* (C.A. Reitzel, København, 1952).
14. Lebedev. The first find of a Devonian tetrapod in the U.S.S.R. *Doklady Academii Nauk SSSR* **278,** 1470–1473 (1984).

15. Bole, G. The Tangled Bank: an introduction to evolution. *Evolutionary Applications* **3,** 91–92. ISSN: 1752-4571 (2010).
16. Cloutier, R. *et al.* Elpistostege and the origin of the vertebrate hand. *Nature* **579,** 549–554. ISSN: 1476-4687 (2020).
17. Watson. On the Primitive Tetrapod Limb. *Anat. Anzeiger* **44,** 24–27 (1913).
18. Holmgren, N. Contribution to the question of the Origin of the Tetrapod Limb. *Acta Zoologica* **20,** 89–124. ISSN: 00017272, 14636395 (June 1939).
19. Gregory, W. K. & Raven, H. C. Paired fins and girdles in ostracoderms, placoderms, and other primitive fishes. *Annals of the New York Academy of Sciences* **42,** 275–291. ISSN: 00778923, 17496632 (Nov. 1941).
20. Ahlberg & Milner. The origin and early diversification of tetrapods. *Nature* **368,** 507–514. ISSN: 1476-4687 (1994).
21. Shubin, Tabin & Carroll. Fossils, genes and the evolution of animal limbs. *Nature* **388,** 639. ISSN: 1476-4687 (1997).
22. Sordino, Hoeven & Duboule. Hox gene expression in teleost fins and the origin of vertebrate digits. *Nature* **375,** 678–681. ISSN: 1476-4687 (1995).
23. Hoeven, Zákány & Duboule. Gene Transpositions in the HoxD Complex Reveal a Hierarchy of Regulatory Controls. *Cell* **85,** 1025–1035. ISSN: 0092-8674, 1097-4172 (1996).
24. Shubin, Daeschler & Jenkins. The pectoral fin of Tiktaalik roseae and the origin of the tetrapod limb. *Nature* **440,** 764–771. ISSN: 1476-4687 (Apr. 2006).
25. Boisvert, Mark-Kurik & Ahlberg. The pectoral fin of Panderichthys and the origin of digits. *Nature* **456,** 636–638. ISSN: 1476-4687 (2008).
26. Coates. Polydactyly in the earliest known tetrapod limbs. *Nature* **347,** 66–69. ISSN: 1476-4687 (Sept. 1990).
27. Owen, R. *On the Anatomy of Vertebrates ...: Birds and mammals* 638 pp. (Longmans, Green and Company, 1866).
28. Gadow, F. *Einleitung in die Osteologie der Säugethiere.* `https://www.worldcat.org/title/einleitung-in-die-osteologie-der-saugethiere/oclc/14804581` (2021).
29. May, O. Le pisiforme : sésamoïde ou os carpien. *Annales de Chirurgie de la Main et du Membre Supérieur* **15,** 265–271. ISSN: 11532424 (1996).
30. Galis, F. Why five fingers? Evolutionary constraints on digit numbers. *Trends in Ecology & Evolution* **16,** 637–646. ISSN: 0169-5347 (2001).
31. Kohlsdorf, T. & Wagner, G. P. Evidence for the Reversibility of Digit Loss: A Phylogenetic Study of Limb Evolution in Bachia (gymnophthalmidae: Squamata). *Evolution* **60,** 1896–1912. ISSN: 1558-5646 (2006).
32. Galis, F., Arntzen, J. W. & Lande, R. Dollo's Law and the Irreversibility of Digit Loss in Bachia. *Evolution* **64,** 2466–2476. ISSN: 1558-5646 (2010).
33. Kohlsdorf, T., Lynch, V. J., Rodrigues, M. T., Brandley, M. C. & Wagner, G. P. Data and Data Interpretation in the Study of Limb Evolution: A Reply to Galis Et Al.

on the Reevolution of Digits in the Lizard Genus Bachia. *Evolution* **64,** 2477–2485. ISSN: 1558-5646 (2010).

34. Galis, F., Metz, J. A. & van Alphen, J. J. Development and Evolutionary Constraints in Animals. *Annual Review of Ecology, Evolution, and Systematics* **49,** 499–522 (2018).
35. Baedke, J. & Gilbert, S. F. in *The Stanford Encyclopedia of Philosophy* (ed Zalta, E. N.) Fall 2021 (Metaphysics Research Lab, Stanford University, 2021).
36. Moreau, C. *et al.* Timed Collinear Activation of Hox Genes during Gastrulation Controls the Avian Forelimb Position. *Current Biology* **29,** 35–50.e4. ISSN: 09609822 (2019).
37. Nishimoto, S., Wilde, S. M., Wood, S. & Logan, M. P. O. RA Acts in a Coherent Feed-Forward Mechanism with Tbx5 to Control Limb Bud Induction and Initiation. *Cell Reports* **12,** 879–891. ISSN: 2211-1247 (2015).
38. Gros & Tabin. Vertebrate Limb Bud Formation Is Initiated by Localized Epithelial-to-Mesenchymal Transition. *Science* **343,** 1253–1256. ISSN: 0036-8075, 1095-9203 (2014).
39. Kawakami, Y. *et al.* WNT Signals Control FGF-Dependent Limb Initiation and AER Induction in the Chick Embryo. *Cell* **104,** 891–900. ISSN: 0092-8674, 1097-4172 (2001).
40. Ohuchi, H. *et al.* The mesenchymal factor, FGF10, initiates and maintains the outgrowth of the chick limb bud through interaction with FGF8, an apical ectodermal factor. *Development* **124,** 2235–2244. ISSN: 0950-1991 (1997).
41. Fallon, J. F. *et al.* FGF-2: Apical Ectodermal Ridge Growth Signal for Chick Limb Development. *Science* **264,** 104–107 (1994).
42. Vogel, A., Rodriguez, C. & Izpisua-Belmonte, J. Involvement of FGF-8 in initiation, outgrowth and patterning of the vertebrate limb. *Development* **122,** 1737–1750. ISSN: 0950-1991 (1996).
43. Saunders, G. Ectodermal-mesenchymal interaction in the origin of limb symmetry. *Epithelial-Mesenchymal Interaction,* pp 78–97. (1968).
44. Tickle, Summerbell & Wolpert. Positional signalling and specification of digits in chick limb morphogenesis. *Nature* **254,** 199–202. ISSN: 1476-4687 (1975).
45. Tickle, C., Alberts, B., Wolpert, L. & Lee, J. Local application of retinoic acid to the limb bond mimics the action of the polarizing region. *Nature* **296,** 564–566. ISSN: 0028-0836 (1982).
46. Riddle, R. D., Johnson, R. L., Laufer, E. & Tabin, C. Sonic hedgehog mediates the polarizing activity of the ZPA. *Cell* **75,** 1401–1416. ISSN: 0092-8674 (1993).
47. Pickering, J., Wali, N. & Towers, M. Transcriptional changes in chick wing bud polarization induced by retinoic acid. *Developmental Dynamics* **246,** 682–690. ISSN: 1097-0177 (2017).
48. Chiang, C. *et al.* Manifestation of the Limb Prepattern: Limb Development in the Absence of Sonic Hedgehog Function. *Developmental Biology* **236,** 421–435. ISSN: 0012-1606 (2001).

49. Kraus, P., Fraidenraich, D. & Loomis, C. A. Some distal limb structures develop in mice lacking Sonic hedgehog signaling. *Mechanisms of Development* **100,** 45–58. ISSN: 0925-4773 (2001).
50. Wolpert, L. Positional information and the spatial pattern of cellular differentiation. *Journal of Theoretical Biology* **25,** 1–47. ISSN: 0022-5193 (1969).
51. Yang, Y. *et al.* Relationship between dose, distance and time in Sonic Hedgehog-mediated regulation of anteroposterior polarity in the chick limb. *Development* **124,** 4393–4404. ISSN: 0950-1991 (1997).
52. Adachi, N., Robinson, M., Goolsbee, A. & Shubin, N. H. Regulatory evolution of Tbx5 and the origin of paired appendages. *Proceedings of the National Academy of Sciences* **113,** 10115–10120. ISSN: 0027-8424, 1091-6490 (2016).
53. Drossopoulou, G. *et al.* A model for anteroposterior patterning of the vertebrate limb based on sequential long- and short-range Shh signalling and Bmp signalling. *Development* **127,** 1337–1348. ISSN: 0950-1991, 1477-9129 (2000).
54. Scherz, P. J., McGlinn, E., Nissim, S. & Tabin, C. J. Extended exposure to Sonic hedgehog is required for patterning the posterior digits of the vertebrate limb. *Developmental Biology* **308,** 343–354. ISSN: 0012-1606 (2007).
55. Shapiro, M. D., Hanken, J. & Rosenthal, N. Developmental basis of evolutionary digit loss in the Australian lizard Hemiergis. *Journal of Experimental Zoology Part B: Molecular and Developmental Evolution* **297B,** 48–56. ISSN: 1552-5015 (2003).
56. Cooper, K. L. *et al.* Patterning and post-patterning modes of evolutionary digit loss in mammals. *Nature* **511,** 41–45. ISSN: 1476-4687 (July 2014).
57. Lopez-Rios, J. *et al.* Attenuated sensing of SHH by Ptch1 underlies evolution of bovine limbs. *Nature* **511,** 46–51. ISSN: 1476-4687 (July 2014).
58. Maas, S. A., Suzuki, T. & Fallon, J. F. Identification of spontaneous mutations within the long-range limb-specific Sonic hedgehog enhancer (ZRS) that alter Sonic hedgehog expression in the chicken limb mutants oligozeugodactyly and silkie breed. *Developmental Dynamics* **240,** 1212–1222. ISSN: 1097-0177 (2011).
59. Chiang *et al.* Cyclopia and defective axial patterning in mice lacking Sonic hedgehog gene function. *Nature* **383,** 407–413. ISSN: 1476-4687 (1996).
60. Lettice, L. A. *et al.* Disruption of a long-range cis-acting regulator for Shh causes preaxial polydactyly. *Proceedings of the National Academy of Sciences* **99,** 7548–7553. ISSN: 0027-8424, 1091-6490 (May 28, 2002).
61. Lettice, L. A. *et al.* A long-range Shh enhancer regulates expression in the developing limb and fin and is associated with preaxial polydactyly. *Human Molecular Genetics* **12,** 1725–1735. ISSN: 0964-6906 (2003).
62. Lettice, L. A., Hill, A. E., Devenney, P. S. & Hill, R. E. Point mutations in a distant sonic hedgehog cis-regulator generate a variable regulatory output responsible for preaxial polydactyly. *Human Molecular Genetics* **17,** 978–985. ISSN: 0964-6906 (2008).
63. Lettice, L. A., Devenney, P., De Angelis, C. & Hill, R. E. The Conserved Sonic Hedgehog Limb Enhancer Consists of Discrete Functional Elements that Regulate Precise Spatial Expression. *Cell Reports* **20,** 1396–1408. ISSN: 2211-1247 (2017).

64. Park, K., Kang, J., Subedi, K. P., Ha, J.-H. & Park, C. Canine Polydactyl Mutations With Heterogeneous Origin in the Conserved Intronic Sequence of LMBR1. *Genetics* **179,** 2163–2172. ISSN: 1943-2631 (2008).
65. Xu, C. *et al.* A novel ZRS variant causes preaxial polydactyly type I by increased sonic hedgehog expression in the developing limb bud. *Genetics in Medicine* **22,** 189–198. ISSN: 1530-0366 (2020).
66. Carballo, G. B., Honorato, J. R., de Lopes, G. P. F. & Spohr, T. C. L. d. S. e. A highlight on Sonic hedgehog pathway. *Cell Communication and Signaling* **16,** 11. ISSN: 1478-811X (2018).
67. Litingtung, Y., Dahn, R. D., Li, Y., Fallon, J. F. & Chiang, C. Shh and Gli3 are dispensable for limb skeleton formation but regulate digit number and identity. *Nature* **418,** 979–983. ISSN: 1476-4687 (2002).
68. Te Welscher, P. *et al.* Progression of Vertebrate Limb Development Through SHH-Mediated Counteraction of GLI3. *Science* **298,** 827–830 (2002).
69. Suzuki, T. How is digit identity determined during limb development? *Development, Growth & Differentiation* **55,** 130–138. ISSN: 1440-169X (2013).
70. Tickle, C. & Towers, M. Sonic Hedgehog Signaling in Limb Development. *Frontiers in Cell and Developmental Biology* **5.** ISSN: 2296-634X (2017).
71. Lopez-Rios, D. *et al.* GLI3 Constrains Digit Number by Controlling Both Progenitor Proliferation and BMP-Dependent Exit to Chondrogenesis. *Developmental Cell* **22,** 837–848. ISSN: 1534-5807 (2012).
72. Turing. The chemical basis of morphogenesis. *Philos. Trans. R. Soc. London Ser. B.* **237,** 37 (1952).
73. Sheth, R. *et al.* Hox Genes Regulate Digit Patterning by Controlling the Wavelength of a Turing-Type Mechanism. *Science* **338,** 1476–1480 (2012).
74. Raspopovic, J., Marcon, L., Russo, L. & Sharpe, J. Digit patterning is controlled by a Bmp-Sox9-Wnt Turing network modulated by morphogen gradients. *Science* **345,** 566–570 (2014).
75. Onimaru, K., Marcon, L., Musy, M., Tanaka, M. & Sharpe, J. The fin-to-limb transition as the re-organization of a Turing pattern. *Nature Communications* **7,** 11582. ISSN: 2041-1723 (2016).
76. Hiscock & Tschopp. On the Formation of Digits and Joints during Limb Development. *Developmental Cell* **41,** 459–465. ISSN: 1534-5807 (2017).
77. Lopez-Rios, J. The many lives of SHH in limb development and evolution. *Seminars in Cell & Developmental Biology. Bone development and disease* **49,** 116–124. ISSN: 1084-9521 (2016).
78. Harfe, B. D. *et al.* Evidence for an Expansion-Based Temporal Shh Gradient in Specifying Vertebrate Digit Identities. *Cell* **118,** 517–528. ISSN: 0092-8674 (2004).
79. Zuniga, A. Next generation limb development and evolution: old questions, new perspectives. *Development* **142,** 3810–3820. ISSN: 0950-1991, 1477-9129 (2015).
80. Tajbakhsh, S. & Spörle, R. Somite Development: Constructing the Vertebrate Body. *Cell* **92,** 9–16. ISSN: 0092-8674, 1097-4172 (1998).

81. Daston, G., Lamar, E., Olivier, M. & Goulding, M. Pax-3 is necessary for migration but not differentiation of limb muscle precursors in the mouse. *Development (Cambridge, England)* **122,** 1017–1027. ISSN: 0950-1991 (1996).
82. Seale, P. *et al.* Pax7 Is Required for the Specification of Myogenic Satellite Cells. *Cell* **102,** 777–786. ISSN: 0092-8674 (2000).
83. Brohmann Jagla, B. The role of Lbx1 in migration of muscle precursor cells. *Development* **127,** 437–445. ISSN: 0950-1991 (2000).
84. Gross, M. *et al.* Lbx1 is required for muscle precursor migration along a lateral pathway into the limb. *Development* **127,** 413–424. ISSN: 0950-1991 (2000).
85. Bladt, F., Riethmacher, D., Isenmann, S., Aguzzi, A. & Birchmeier, C. Essential role for the c-met receptor in the migration of myogenic precursor cells into the limb bud. *Nature* **376,** 768–771. ISSN: 1476-4687 (1995).
86. Swartz, M. E., Eberhart, J., Pasquale, E. B. & Krull, C. E. EphA4/ephrin-A5 interactions in muscle precursor cell migration in the avian forelimb. *Development* **128,** 4669–4680. ISSN: 0950-1991 (2001).
87. Vasyutina, E. *et al.* CXCR4 and Gab1 cooperate to control the development of migrating muscle progenitor cells. *Genes & Development* **19,** 2187–2198. ISSN: 0890-9369, 1549-5477 (2005).
88. Mok, G. F. & Sweetman, D. Many routes to the same destination: lessons from skeletal muscle development. *Reproduction* **141,** 301–312. ISSN: 1741-7899, 1470-1626 (2011).
89. Hayashi, K. & Ozawa, E. Vital labelling of somite-derived myogenic cells in the chicken limb bud. *Roux's Archives of Developmental Biology* **200,** 188–192. ISSN: 0930-035X, 1432-041X (1991).
90. Kardon, Harfe & Tabin. A Tcf4-Positive Mesodermal Population Provides a Prepattern for Vertebrate Limb Muscle Patterning. *Developmental Cell* **5,** 937–944. ISSN: 1534-5807 (2003).
91. Mathew, S. J. *et al.* Connective tissue fibroblasts and Tcf4 regulate myogenesis. *Development (Cambridge, England)* **138,** 371–384. ISSN: 0950-1991 (2011).
92. Vallecillo-García, P. *et al.* Odd skipped-related 1 identifies a population of embryonic fibro-adipogenic progenitors regulating myogenesis during limb development. *Nature Communications* **8,** 1218. ISSN: 2041-1723 (2017).
93. Millay, D. P. *et al.* Myomaker is a membrane activator of myoblast fusion and muscle formation. *Nature* **499,** 301–305. ISSN: 1476-4687 (2013).
94. Sampath, Sampath & Millay. Myoblast fusion confusion: the resolution begins. *Skeletal Muscle* **8,** 3. ISSN: 2044-5040 (2018).
95. Esteves de Lima, J. *et al.* Unexpected contribution of fibroblasts to muscle lineage as a mechanism for limb muscle patterning. *Nature Communications* **12,** 3851. ISSN: 2041-1723 (June 22, 2021).
96. Zammit, P. S. Function of the myogenic regulatory factors Myf5, MyoD, Myogenin and MRF4 in skeletal muscle, satellite cells and regenerative myogenesis. *Seminars*

in Cell & Developmental Biology. Skeletal Muscle Development on the 30th Anniversary of MyoD **72,** 19–32. ISSN: 1084-9521 (2017).

97. Comai, G. & Tajbakhsh, S. in *Current Topics in Developmental Biology* (ed Taneja, R.) 1–73 (Academic Press, 2014).
98. Weintraub, H. *et al.* The myoD Gene Family: Nodal Point During Specification of the Muscle Cell Lineage. *Science* **251,** 761–766 (1991).
99. Van Swearingen, J. & Lance-Jones, C. Slow and Fast Muscle Fibers Are Preferentially Derived from Myoblasts Migrating into the Chick Limb Bud at Different Developmental Times. *Developmental Biology* **170,** 321–337. ISSN: 0012-1606 (1995).
100. Schiaffino, S. & Reggiani, C. Fiber Types in Mammalian Skeletal Muscles. *Physiological Reviews* **91,** 1447–1531. ISSN: 0031-9333 (2011).
101. Duprez, D., Lapointe, F., Edom-Vovard, F., Kostakopoulou, K. & Robson, L. Sonic Hedgehog (SHH) specifies muscle pattern at tissue and cellular chick level, in the chick limb bud. *Mechanisms of Development* **82,** 151–163. ISSN: 0925-4773 (1999).
102. Subramanian, A. & Schilling, T. F. Tendon development and musculoskeletal assembly: emerging roles for the extracellular matrix. *Development* **142,** 4191–4204. ISSN: 0950-1991.
103. Edom-Vovard & Duprez, D. Signals regulating tendon formation during chick embryonic development. *Developmental Dynamics* **229,** 449–457. ISSN: 1097-0177 (2004).
104. Schweitzer, Z. & Volk. Connecting muscles to tendons: tendons and musculoskeletal development in flies and vertebrates. *Development (Cambridge, England)* **137,** 2807–2817. ISSN: 0950-1991 (2010).
105. Gaut, L. & Duprez, D. Tendon development and diseases. *WIREs Developmental Biology* **5,** 5–23. ISSN: 1759-7692 (2016).
106. Thorpe, C. T. & Screen, H. R. C. in *Metabolic Influences on Risk for Tendon Disorders* (eds Ackermann, P. W. & Hart, D. A.) 3–10 (Springer International Publishing, Cham, 2016). ISBN: 978-3-319-33943-6.
107. Kardon. Muscle and tendon morphogenesis in the avian hind limb. *Development* **125,** 4019–4032. ISSN: 0950-1991, 1477-9129 (Oct. 15, 1998).
108. Murchison, N. D. *et al.* Regulation of tendon differentiation by scleraxis distinguishes force-transmitting tendons from muscle-anchoring tendons. *Development* **134,** 2697–2708. ISSN: 0950-1991 (2007).
109. Edom-Vovard, Schuler, B., Bonnin, M.-A., Teillet, M.-A. & Duprez, D. Fgf4 Positively Regulates scleraxis and Tenascin Expression in Chick Limb Tendons. *Developmental Biology* **247,** 351–366. ISSN: 0012-1606 (2002).
110. Rodriguez-Guzman, M. *et al.* Tendon-muscle crosstalk controls muscle bellies morphogenesis, which is mediated by cell death and retinoic acid signaling. *Developmental Biology* **302,** 267–280. ISSN: 0012-1606 (Feb. 1, 2007).
111. Storey, K. G., Crossley, J. M. & Stern, C. D. Neural induction and regionalisation in the chick embryo, 16 (1992).

112. Altaba, A. R. i. Induction and axial patterning of the neural plate: Planar and vertical signals. *Journal of Neurobiology* **24,** 1276–1304. ISSN: 0022-3034, 1097-4695 (1993).
113. Spemann, M. Uber Induktion yon Embryonalanlagen durch Implantation artfremder 0rganisatoren (1923).
114. Waddington, C. H. Experiments on the Development of Chick and Duck Embryos, Cultivated in vitro. *Philosophical Transactions of the Royal Society of London. Series B, Containing Papers of a Biological Character* **221,** 179–230. ISSN: 0264-3960 (1932).
115. Waddington, C. H. Induction by the Primitive Streak and its Derivatives in the Chick. *Journal of Experimental Biology* **10,** 38–46. ISSN: 0022-0949 (1933).
116. Copp, A. J., Greene, N. D. E. & Murdoch, J. N. The genetic basis of mammalian neurulation. *Nature Reviews Genetics* **4,** 784–793. ISSN: 1471-0064 (2003).
117. Nikolopoulou, E., Galea, G. L., Rolo, A., Greene, N. D. E. & Copp, A. J. Neural tube closure: cellular, molecular and biomechanical mechanisms. *Development (Cambridge, England)* **144,** 552–566. ISSN: 0950-1991 (2017).
118. Prasad *et al.* Specification and formation of the neural crest: Perspectives on lineage segregation. *Genesis (New York, N.Y. : 2000)* **57,** e23276. ISSN: 1526-954X (2019).
119. Teillet, M.-A., Kalcheim, C. & Le Douarin, N. M. Formation of the dorsal root ganglia in the avian embryo: Segmental origin and migratory behavior of neural crest progenitor cells. *Developmental Biology* **120,** 329–347. ISSN: 0012-1606 (1987).
120. Lallier, T. E. & Bronner-Fraser, M. A spatial and temporal analysis of dorsal root and sympathetic ganglion formation in the avian embryo. *Developmental Biology* **127,** 99–112. ISSN: 0012-1606 (1988).
121. Sagner, A. & Briscoe, J. Establishing neuronal diversity in the spinal cord: a time and a place. *Development* **146.** ISSN: 0950-1991, 1477-9129 (2019).
122. Le Dréau, G. & Martí, E. Dorsal–ventral patterning of the neural tube: A tale of three signals. *Developmental Neurobiology* **72,** 1471–1481. ISSN: 1932-846X (2012).
123. Häring, M. *et al.* Neuronal atlas of the dorsal horn defines its architecture and links sensory input to transcriptional cell types. *Nature Neuroscience* **21,** 869–880. ISSN: 1546-1726 (2018).
124. Briscoe, J. & Ericson, J. Specification of neuronal fates in the ventral neural tube. *Current Opinion in Neurobiology* **11,** 43–49. ISSN: 0959-4388 (2001).
125. Lee, Dietrich, P. & Jessell, T. M. Genetic ablation reveals that the roof plate is essential for dorsal interneuron specification. *Nature* **403,** 734–740. ISSN: 1476-4687 (2000).
126. Roelink, H. *et al.* Floor plate and motor neuron induction by different concentrations of the amino-terminal cleavage product of sonic hedgehog autoproteolysis. *Cell* **81,** 445–455. ISSN: 00928674 (1995).
127. Ericson, J., Morton, S., Kawakami, A., Roelink, H. & Jessell, T. M. Two Critical Periods of Sonic Hedgehog Signaling Required for the Specification of Motor Neuron Identity. *Cell* **87,** 661–673. ISSN: 0092-8674, 1097-4172 (1996).

128. Briscoe, Pierani, A., Jessell, T. M. & Ericson, J. A Homeodomain Protein Code Specifies Progenitor Cell Identity and Neuronal Fate in the Ventral Neural Tube. *Cell* **101,** 435–445. ISSN: 0092-8674 (2000).
129. Briscoe *et al.* Homeobox gene Nkx2.2 and specification of neuronal identity by graded Sonic hedgehog signalling. *Nature* **398,** 622–627. ISSN: 1476-4687 (1999).
130. Sander, M. *et al.* Ventral neural patterning by Nkx homeobox genes: Nkx6.1 controls somatic motor neuron and ventral interneuron fates. *Genes & Development* **14,** 2134–2139. ISSN: 0890-9369 (2000).
131. Mizuguchi, R. *et al.* Combinatorial Roles of Olig2 and Neurogenin2 in the Coordinated Induction of Pan-Neuronal and Subtype-Specific Properties of Motoneurons. *Neuron* **31,** 757–771. ISSN: 0896-6273 (2001).
132. Novitch, B. G., Chen, A. I. & Jessell, T. M. Coordinate Regulation of Motor Neuron Subtype Identity and Pan-Neuronal Properties by the bHLH Repressor Olig2. *Neuron* **31,** 773–789. ISSN: 0896-6273 (2001).
133. Zhou, Q. & Anderson, D. J. The bHLH Transcription Factors OLIG2 and OLIG1 Couple Neuronal and Glial Subtype Specification. *Cell* **109,** 61–73. ISSN: 0092-8674 (2002).
134. Zhou, Q., Choi, G. & Anderson, D. J. The bHLH Transcription Factor Olig2 Promotes Oligodendrocyte Differentiation in Collaboration with Nkx2.2. *Neuron* **31,** 791–807. ISSN: 0896-6273 (2001).
135. Mauti, O., Domanitskaya, E., Andermatt, I., Sadhu, R. & Stoeckli, E. T. Semaphorin6A acts as a gate keeper between the central and the peripheral nervous system. *Neural Development* **2,** 28. ISSN: 1749-8104 (2007).
136. Lee, H. *et al.* Slit and Semaphorin signaling governed by Islet transcription factors positions motor neuron somata within the neural tube. *Experimental Neurology* **269,** 17–27. ISSN: 0014-4886 (2015).
137. Kim, M., Fontelonga, T. M., Lee, C. H., Barnum, S. J. & Mastick, G. S. Motor axons are guided to exit points in the spinal cord by Slit and Netrin signals. *Developmental Biology* **432,** 178–191. ISSN: 0012-1606 (2017).
138. Kim, M., Bjorke, B. & Mastick, G. S. Motor neuron migration and positioning mechanisms: New roles for guidance cues. *Seminars in Cell & Developmental Biology. Axon guidance: Signaling pathways old and new across a variety of developmental contexts* **85,** 78–83. ISSN: 1084-9521 (2019).
139. Dasen, J. S., Tice, B. C., Brenner-Morton, S. & Jessell, T. M. A Hox Regulatory Network Establishes Motor Neuron Pool Identity and Target-Muscle Connectivity. *Cell* **123,** 477–491. ISSN: 0092-8674 (2005).
140. Dasen, J. S., De Camilli, A., Wang, B., Tucker, P. W. & Jessell, T. M. Hox Repertoires for Motor Neuron Diversity and Connectivity Gated by a Single Accessory Factor, FoxP1. *Cell* **134,** 304–316. ISSN: 0092-8674 (2008).
141. Arber, S. *et al.* Requirement for the Homeobox Gene Hb9 in the Consolidation of Motor Neuron Identity. *Neuron* **23,** 659–674. ISSN: 0896-6273 (Aug. 1, 1999).

142. Tsuchida, T. *et al.* Topographic organization of embryonic motor neurons defined by expression of LIM homeobox genes. *Cell* **79,** 957–970. ISSN: 0092-8674, 1097-4172 (1994).
143. Kania, A., Johnson, R. L. & Jessell, T. M. Coordinate Roles for LIM Homeobox Genes in Directing the Dorsoventral Trajectory of Motor Axons in the Vertebrate Limb. *Cell* **102,** 161–173. ISSN: 0092-8674 (2000).
144. Kania, A. & Jessell, T. M. Topographic Motor Projections in the Limb Imposed by LIM Homeodomain Protein Regulation of Ephrin-A:EphA Interactions. *Neuron* **38,** 581–596. ISSN: 0896-6273 (2003).
145. Sockanathan, S. & Jessell, T. M. Motor Neuron–Derived Retinoid Signaling Specifies the Subtype Identity of Spinal Motor Neurons. *Cell* **94,** 503–514. ISSN: 0092-8674 (1998).
146. Luria, V., Krawchuk, D., Jessell, T. M., Laufer, E. & Kania, A. Specification of Motor Axon Trajectory by Ephrin-B:EphB Signaling: Symmetrical Control of Axonal Patterning in the Developing Limb. *Neuron* **60,** 1039–1053. ISSN: 0896-6273 (2008).
147. Price, Garcia, D. M., Ranscht, B. & Jessell, T. M. Regulation of Motor Neuron Pool Sorting by Differential Expression of Type II Cadherins. *Cell* **109,** 205–216. ISSN: 0092-8674 (2002).
148. Hollyday, M. & Jacobson, R. D. Location of motor pools innervating chick wing. *Journal of Comparative Neurology* **302,** 575–588. ISSN: 1096-9861 (1990).
149. Landmesser, L. The distribution of motoneurones supplying chick hind limb muscles. *The Journal of Physiology* **284,** 371–389. ISSN: 0022-3751 (1978).
150. Landmesser. The acquisition of motoneuron subtype identity and motor circuit formation. *International Journal of Developmental Neuroscience* **19,** 175–182. ISSN: 1873-474X (2001).
151. Ensini, M., Tsuchida, T., Belting, H. & Jessell, T. The control of rostrocaudal pattern in the developing spinal cord: specification of motor neuron subtype identity is initiated by signals from paraxial mesoderm. *Development* **125,** 969–982. ISSN: 0950-1991 (1998).
152. Liu, J.-P., Laufer, E. & Jessell, T. M. Assigning the Positional Identity of Spinal Motor Neurons: Rostrocaudal Patterning of Hox-c Expression by FGFs, Gdf11, and Retinoids. *Neuron* **32,** 997–1012. ISSN: 0896-6273 (2001).
153. Dasen, J. S., Liu, J.-P. & Jessell, T. M. Motor neuron columnar fate imposed by sequential phases of Hox-c activity. *Nature* **425,** 926–933. ISSN: 1476-4687 (Oct. 2003).
154. Shah, V., Drill, E. & Lance-Jones, C. Ectopic expression of Hoxd10 in thoracic spinal segments induces motoneurons with a lumbosacral molecular profile and axon projections to the limb. *Developmental Dynamics* **231,** 43–56. ISSN: 1097-0177 (2004).
155. Wu, Y., Wang, G., Scott, S. A. & Capecchi, M. R. Hoxc10 and Hoxd10 regulate mouse columnar, divisional and motor pool identity of lumbar motoneurons. *Development* **135,** 171–182. ISSN: 0950-1991, 1477-9129 (2008).

156. Vermot, J. *et al.* Retinaldehyde dehydrogenase 2 and Hoxc8 are required in the murine brachial spinal cord for the specification of Lim1+ motoneurons and the correct distribution of Islet1+ motoneurons. *Development* **132,** 1611–1621. ISSN: 0950-1991 (2005).
157. Mendelsohn Dasen, J. Divergent Hox Coding and Evasion of Retinoid Signaling Specifies Motor Neurons Innervating Digit Muscles. *Neuron* **93,** 792–805.e4. ISSN: 0896-6273 (2017).
158. Rijli, F. M. *et al.* Cryptorchidism and homeotic transformations of spinal nerves and vertebrae in Hoxa-10 mutant mice. *Proceedings of the National Academy of Sciences* **92,** 8185–8189. ISSN: 0027-8424, 1091-6490 (1995).
159. Lin, A. W. & Carpenter, E. M. Hoxa10 and Hoxd10 coordinately regulate lumbar motor neuron patterning. *Journal of Neurobiology* **56,** 328–337. ISSN: 0022-3034 (2003).
160. Jung, H. *et al.* Global Control of Motor Neuron Topography Mediated by the Repressive Actions of a Single Hox Gene. *Neuron* **67,** 781–796. ISSN: 0896-6273 (2010).
161. Dickson, B. J. Molecular Mechanisms of Axon Guidance. *Science* **298,** 1959–1964. ISSN: 0036-8075, 1095-9203 (2002).
162. Tessier-Lavigne. The Molecular Biology of Axon Guidance. *Science* **274** (1996).
163. Stoeckli, E. T. Understanding axon guidance: are we nearly there yet? *Development* **145.** ISSN: 0950-1991 (2018).
164. Mortimer, D., Fothergill, T., Pujic, Z., Richards, L. J. & Goodhill, G. J. Growth cone chemotaxis. *Trends in Neurosciences* **31,** 90–98. ISSN: 0166-2236 (2008).
165. Okabe, S. & Hirokawa, N. Actin dynamics in growth cones. *Journal of Neuroscience* **11,** 1918–1929. ISSN: 0270-6474, 1529-2401 (1991).
166. Gomez, T. M. & Letourneau, P. C. Actin dynamics in growth cone motility and navigation. *Journal of Neurochemistry* **129,** 221–234. ISSN: 1471-4159 (2014).
167. Gallo, G. & Letourneau, P. C. Regulation of growth cone actin filaments by guidance cues. *Journal of Neurobiology* **58,** 92–102. ISSN: 1097-4695 (2004).
168. Goshima, Y., Ito, T., Sasaki, Y. & Nakamura, F. Semaphorins as signals for cell repulsion and invasion. *The Journal of Clinical Investigation* **109,** 993–998. ISSN: 0021-9738 (2002).
169. Wu, K.-Y. *et al.* Semaphorin 3A activates the guanosine triphosphatase Rab5 to promote growth cone collapse and organize callosal axon projections. *Science Signaling* **7,** ra81–ra81 (2014).
170. Leonardo, E. D. *et al.* Guidance of Developing Axons by Netrin-1 and Its Receptors. *Cold Spring Harbor Symposia on Quantitative Biology* **62,** 467–478. ISSN: 0091-7451, 1943-4456 (1997).
171. Klein, R. Eph/ephrin signaling in morphogenesis, neural development and plasticity. *Current Opinion in Cell Biology* **16,** 580–589. ISSN: 0955-0674 (2004).
172. Klein, R. Eph/ephrin signalling during development. *Development* **139,** 4105–4109. ISSN: 0950-1991 (2012).

173. Comer, J. D., Alvarez, S., Butler, S. J. & Kaltschmidt, J. A. Commissural axon guidance in the developing spinal cord: from Cajal to the present day. *Neural Development* **14,** 9. ISSN: 1749-8104 (2019).
174. Stoeckli & Landmesser. Axon guidance at choice points. *Current Opinion in Neurobiology* **8,** 73–79. ISSN: 0959-4388 (1998).
175. Zou, Y., Stoeckli, E., Chen, H. & Tessier-Lavigne, M. Squeezing Axons Out of the Gray Matter: A Role for Slit and Semaphorin Proteins from Midline and Ventral Spinal Cord. *Cell* **102,** 363–375. ISSN: 0092-8674 (2000).
176. Bourikas, D. *et al.* Sonic hedgehog guides commissural axons along the longitudinal axis of the spinal cord. *Nature Neuroscience* **8,** 297–304. ISSN: 1546-1726 (2005).
177. Domanitskaya, E. *et al.* Sonic Hedgehog Guides Post-Crossing Commissural Axons Both Directly and Indirectly by Regulating Wnt Activity. *The Journal of Neuroscience* **30,** 11167–11176. ISSN: 0270-6474 (2010).
178. Castellani, V. Building Spinal and Brain Commissures: Axon Guidance at the Midline. *ISRN Cell Biology* **2013,** e315387 (2013).
179. De Ramon Francàs, G., Zuñiga, N. R. & Stoeckli, E. T. The spinal cord shows the way – How axons navigate intermediate targets. *Developmental Biology* **432,** 43–52. ISSN: 0012-1606 (2017).
180. Wang, G. & Scott, S. A. The "Waiting Period" of Sensory and Motor Axons in Early Chick Hindlimb: Its Role in Axon Pathfinding and Neuronal Maturation. *Journal of Neuroscience* **20,** 5358–5366. ISSN: 0270-6474, 1529-2401 (2000).
181. Sürmeli, G., Akay, T., Ippolito, G. C., Tucker, P. W. & Jessell, T. M. Patterns of Spinal Sensory-Motor Connectivity Prescribed by a Dorsoventral Positional Template. *Cell* **147,** 653–665. ISSN: 0092-8674 (2011).
182. Shirasaki, R., Lewcock, J. W., Lettieri, K. & Pfaff, S. L. FGF as a Target-Derived Chemoattractant for Developing Motor Axons Genetically Programmed by the LIM Code. *Neuron* **50,** 841–853. ISSN: 0896-6273 (2006).
183. De Marco Garcia, N. V. & Jessell, T. M. Early motor neuron pool identity and muscle nerve trajectory defined by post-mitotic restrictions in Nkx6.1 activity. *Neuron* **57,** 217–231. ISSN: 0896-6273 (2008).
184. Di Sanguinetto, S. A. D. T., Dasen, J. S. & Arber, S. Transcriptional mechanisms controlling motor neuron diversity and connectivity. *Current Opinion in Neurobiology* **18,** 36–43. ISSN: 09594388 (2008).
185. Henderson, C. E. *et al.* Neurotrophins promote motor neuron survival and are present in embryonic limb bud. *Nature* **363,** 266–270. ISSN: 1476-4687 (1993).
186. Lin, J. H. *et al.* Functionally Related Motor Neuron Pool and Muscle Sensory Afferent Subtypes Defined by Coordinate ETS Gene Expression. *Cell* **95,** 393–407. ISSN: 0092-8674 (1998).
187. Arber, S., Ladle, D. R., Lin, J. H., Frank, E. & Jessell, T. M. ETS Gene Er81 Controls the Formation of Functional Connections between Group Ia Sensory Afferents and Motor Neurons. *Cell* **101,** 485–498. ISSN: 0092-8674, 1097-4172 (2000).

188. Haase, G. *et al.* GDNF Acts through PEA3 to Regulate Cell Body Positioning and Muscle Innervation of Specific Motor Neuron Pools. *Neuron* **35,** 893–905. ISSN: 0896-6273 (2002).
189. Zhao, Z. *et al.* Overexpression of glial cell line-derived neurotrophic factor in the CNS rescues motoneurons from programmed cell death and promotes their long-term survival following axotomy. *Experimental Neurology* **190,** 356–372. ISSN: 0014-4886 (2004).
190. Gould, T. W. & Oppenheim, R. W. The Function of Neurotrophic Factor Receptors Expressed by the Developing Adductor Motor Pool In Vivo. *Journal of Neuroscience* **24,** 4668–4682. ISSN: 0270-6474, 1529-2401 (2004).
191. Vrieseling, E. & Arber, S. Target-Induced Transcriptional Control of Dendritic Patterning and Connectivity in Motor Neurons by the ETS Gene Pea3. *Cell* **127,** 1439–1452. ISSN: 0092-8674, 1097-4172 (2006).
192. Meier, T. & Wallace, B. G. Formation of the neuromuscular junction: molecules and mechanisms. *BioEssays* **20,** 819–829. ISSN: 1521-1878 (1998).
193. Li, L., Xiong, W.-C. & Mei, L. Neuromuscular Junction Formation, Aging, and Disorders. *Annual Review of Physiology* **80,** 159–188 (2018).
194. Goda, Y. & Davis, G. W. Mechanisms of Synapse Assembly and Disassembly. *Neuron* **40,** 243–264. ISSN: 0896-6273 (2003).
195. Darabid, H., Perez-Gonzalez, A. P. & Robitaille, R. Neuromuscular synaptogenesis: coordinating partners with multiple functions. *Nature Reviews Neuroscience* **15,** 703–718. ISSN: 1471-0048 (2014).
196. Sugita, S. *et al.* VAChT overexpression increases acetylcholine at the synaptic cleft and accelerates aging of neuromuscular junctions. *Skeletal Muscle* **6,** 31. ISSN: 2044-5040 (2016).
197. Tintignac, L. A., Brenner, H.-R. & Rüegg, M. A. Mechanisms Regulating Neuromuscular Junction Development and Function and Causes of Muscle Wasting. *Physiological Reviews* **95,** 809–852. ISSN: 0031-9333 (2015).
198. Arber, S. Motor Circuits in Action: Specification, Connectivity, and Function. *Neuron* **74,** 975–989. ISSN: 0896-6273 (2012).
199. Feirabend, H. K. P. & Marani, E. in *Encyclopedia of the Neurological Sciences* (eds Aminoff, M. J. & Daroff, R. B.) 28–33 (Academic Press, New York, 2003). ISBN: 978-0-12-226870-0.
200. Shin, M. M., Catela, C. & Dasen, J. Intrinsic control of neuronal diversity and synaptic specificity in a proprioceptive circuit. *eLife* **9** (eds Gleeson, J. G. & Bronner, M. E.) e56374. ISSN: 2050-084X (2020).
201. Zeller, R., López-Ríos, J. & Zuniga, A. Vertebrate limb bud development: moving towards integrative analysis of organogenesis. *Nature Reviews Genetics* **10,** 845–858. ISSN: 1471-0064 (2009).
202. Petit, F., Sears, K. E. & Ahituv, N. Limb development: a paradigm of gene regulation. *Nature Reviews Genetics* **18,** 245–258. ISSN: 1471-0064 (2017).

203. Gilbert, S. F. *Developmental Biology* 711 pp. ISBN: 978-0-87893-564-2 (Sinauer Associates, 2010).
204. Chevallier, A., Kieny, M. & Mauger, A. Limb-somite relationship: origin of the limb musculature. *Development* **41,** 245–258. ISSN: 0950-1991, 1477-9129 (1977).
205. Sharir, A., Stern, T., Rot, C., Shahar, R. & Zelzer, E. Muscle force regulates bone shaping for optimal load-bearing capacity during embryogenesis. *Development* **138,** 3247–3259. ISSN: 0950-1991, 1477-9129 (2011).
206. Francisco Botelho, J. *et al.* Skeletal plasticity in response to embryonic muscular activity underlies the development and evolution of the perching digit of birds. *Scientific Reports* **5,** 9840. ISSN: 2045-2322 (2015).
207. Landmesser. The development of motor projection patterns in the chick hind limb. *The Journal of Physiology* **284,** 391–414. ISSN: 0022-3751 (1978).
208. Bonanomi, D. Axon pathfinding for locomotion. *Seminars in Cell & Developmental Biology. Axon guidance: Signaling pathways old and new across a variety of developmental contexts* **85,** 26–35. ISSN: 1084-9521 (2019).
209. Kronenberg, H. M. Developmental regulation of the growth plate. *Nature* **423,** 332–336. ISSN: 0028-0836 (2003).
210. Cooper, K. L. The Lesser Egyptian Jerboa, *Jaculus jaculus* : A Unique Rodent Model for Evolution and Development: Figure 1. *Cold Spring Harbor Protocols* **2011,** pdb.emo066704. ISSN: 1940-3402, 1559-6095 (2011).
211. Wimsatt, W. *Biology of Bats* 420 pp. ISBN: 978-0-323-15119-1 (Elsevier, 2012).
212. De Bakker, M. A. G. *et al.* Digit loss in archosaur evolution and the interplay between selection and constraints. *Nature* **500,** 445–448. ISSN: 1476-4687 (2013).
213. Wagner, G. P. & Chiu, C.-H. The tetrapod limb: A hypothesis on its origin. *Journal of Experimental Zoology* **291,** 226–240. ISSN: 1097-010X (2001).
214. Richardson, M. K. & Chipman, A. D. Developmental constraints in a comparative framework: A test case using variations in phalanx number during amniote evolution. *Journal of Experimental Zoology Part B: Molecular and Developmental Evolution* **296B,** 8–22. ISSN: 1552-5015 (2003).
215. Stirling, R. V. & Summerbell, D. Specific guidance of motor axons to duplicated muscles in the developing amniote limb. *Development* **103,** 97–110. ISSN: 0950-1991, 1477-9129 (1988).
216. Susaki, E. A. *et al.* Whole-Brain Imaging with Single-Cell Resolution Using Chemical Cocktails and Computational Analysis. *Cell* **157,** 726–739. ISSN: 00928674 (2014).
217. Belle, M. *et al.* Tridimensional Visualization and Analysis of Early Human Development. *Cell* **169,** 161–173.e12. ISSN: 1097-4172 (2017).
218. Schramm, C. & Solursh, M. The formation of premuscle masses during chick wing bud development. *Anatomy and Embryology* **182,** 235–247. ISSN: 0340-2061 (1990).
219. Hayashi, K. & Ozawa, E. Myogenic cell migration from somites is induced by tissue contact with medial region of the presumptive limb mesoderm in chick embryos. *Development* **121,** 661–669. ISSN: 0950-1991, 1477-9129 (1995).

220. Bininda-Emonds, O. R. *et al.* Forelimb-hindlimb developmental timing changes across tetrapod phylogeny. *BMC Evolutionary Biology* **7,** 182. ISSN: 1471-2148 (2007).
221. Lance-Jones, C. & Landmesser, L. Pathway selection by embryonic chick motoneurons in an experimentally altered environment. *Proceedings of the Royal Society of London. Series B, Biological Sciences* **214,** 19–52. ISSN: 0950-1193 (1981).
222. Davey, M. G., Towers, M., Vargesson, N. & Tickle, C. The chick limb: embryology, genetics and teratology. *International Journal of Developmental Biology* **62,** 85–95. ISSN: 0214-6282, 1696-3547 (2018).
223. Friocourt, F. *et al.* Recurrent *DCC* gene losses during bird evolution. *Scientific Reports* **7,** 37569. ISSN: 2045-2322 (2017).
224. Ruegg, M. A., Stoeckli, E. T., Lanz, R. B., Streit, P. & Sonderegger, P. A homologue of the axonally secreted protein axonin-1 is an integral membrane protein of nerve fiber tracts involved in neurite fasciculation. *The Journal of Cell Biology* **109,** 2363–2378. ISSN: 0021-9525, 1540-8140 (1989).
225. Diogo, R., Walsh, S., Smith, C., Ziermann, J. M. & Abdala, V. Towards the resolution of a long-standing evolutionary question: muscle identity and attachments are mainly related to topological position and not to primordium or homeotic identity of digits. *Journal of Anatomy* **226,** 523–529. ISSN: 0021-8782 (2015).
226. Huang, A. H. *et al.* Musculoskeletal integration at the wrist underlies the modular development of limb tendons. *Development (Cambridge, England)* **142,** 2431–2441. ISSN: 0950-1991 (2015).
227. Gouti, M., Metzis, V. & Briscoe, J. The route to spinal cord cell types: a tale of signals and switches. *Trends in genetics: TIG* **31,** 282–289. ISSN: 0168-9525 (2015).
228. Young, N. M. & Hallgrímsson, B. Serial homology and the evolution of mammalian limb covariation structure. *Evolution; International Journal of Organic Evolution* **59,** 2691–2704. ISSN: 0014-3820 (2005).
229. Wagner, G. P. *Homology, Genes, and Evolutionary Innovation* ISBN: 978-1-4008-5146-1 (Princeton University Press, 2014).
230. Askari, M., Christensen, K. N., Heath, S., Moran, S. L. & Lachman, N. Presentation of soft tissue anatomy of mirror hand: an anatomical case report with implications for surgical planning. *Surgical and Radiologic Anatomy* **38,** 855–862. ISSN: 0930-1038, 1279-8517 (2016).
231. Mehring, C. *et al.* Augmented manipulation ability in humans with six-fingered hands. *Nature Communications* **10,** 1–9. ISSN: 2041-1723 (2019).
232. Hamburger, V. & Hamilton, H. L. A series of normal stages in the development of the chick embryo. *Journal of Morphology* **88,** 49–92. ISSN: 0362-2525 (1951).
233. Ros, M. A., Kay Simandl, B., Clark, A. W. & Fallon, J. F. in *Developmental Biology Protocols* (eds Tuan, R. S. & Lo, C. W.) 245–266 (Humana Press, Totowa, NJ, 2000). ISBN: 978-1-59259-066-7.
234. Tickle, C., Lee, J. & Eichele, G. A quantitative analysis of the effect of all-trans-retinoic acid on the pattern of chick wing development. *Developmental Biology* **109,** 82–95. ISSN: 0012-1606 (1985).

235. Susaki, E. A. *et al.* Advanced CUBIC protocols for whole-brain and whole-body clearing and imaging. *Nature Protocols* **10,** 1709–1727. ISSN: 1754-2189, 1750-2799 (2015).
236. Schindelin, J. *et al.* Fiji - an Open Source platform for biological image analysis. *Nature methods* **9.** ISSN: 1548-7091 (2012).
237. Tschopp, P. *et al.* A relative shift in cloacal location repositions external genitalia in amniote evolution. *Nature* **516,** 391–394. ISSN: 1476-4687 (2014).
238. Sullivan, G. Anatomy and embryology of the Wing Musculature of the domestic fowl (gallus) (1962).
239. Marín-Llera, J. C., Garciadiego-Cázares, D. & Chimal-Monroy, J. Understanding the Cellular and Molecular Mechanisms That Control Early Cell Fate Decisions During Appendicular Skeletogenesis. *Frontiers in Genetics* **0.** ISSN: 1664-8021 (2019).
240. Buckingham, M. *et al.* The formation of skeletal muscle: from somite to limb. *Journal of Anatomy* **202,** 59–68. ISSN: 0021-8782 (2003).
241. Yamamoto, M. & Abe, S. Mechanism of muscle–tendon–bone complex development in the head. *Anatomical Science International* **95,** 165–173. ISSN: 1447-073X (2020).
242. Briscoe & Ericson, J. The specification of neuronal identity by graded sonic hedgehog signalling. *Seminars in Cell & Developmental Biology* **10,** 353–362. ISSN: 1084-9521 (1999).
243. Ulloa, F. & Martí, E. Wnt won the war: Antagonistic role of Wnt over Shh controls dorso-ventral patterning of the vertebrate neural tube. *Developmental Dynamics* **239,** 69–76 (2010).
244. Bonanomi, D. & Pfaff, S. L. Motor Axon Pathfinding. *Cold Spring Harbor Perspectives in Biology* **2.** ISSN: 1943-0264 (2010).
245. Hamburger, V. Cell death in the development of the lateral motor column of the chick embryo. *The Journal of Comparative Neurology* **160,** 535–546. ISSN: 0021-9967, 1096-9861 (1975).
246. Shorey, S. The effect of the destruction of peripheral areas on the differentiation of the neuroblasts. *Archiv für Entwicklungsmechanik der Organismen* **29,** 196–198. ISSN: 0949-944X, 1432-041X (1910).
247. Hollyday, M. & Hamburger, V. Reduction of the naturally occurring motor neuron loss by enlargement of the periphery. *Journal of Comparative Neurology* **170,** 311–320. ISSN: 1096-9861 (1976).
248. Maheras, H. M. & Pollack, E. D. Quantitative compensation by lateral motor column neurons in response to four functional hindlimbs in a frog tadpole. *Developmental Brain Research* **19,** 150–154. ISSN: 0165-3806 (1985).
249. Sperry, D. G. & Grobstein, P. Regulation of neuron numbers in Xenopus laevis: Effects of hormonal manipulation altering size at metamorphosis. *Journal of Comparative Neurology* **232,** 287–298. ISSN: 1096-9861 (1985).
250. Tanaka, H. & Landmesser, L. T. Cell death of lumbosacral motoneurons in chick, quail, and chick-quail chimera embryos: a test of the quantitative matching

hypothesis of neuronal cell death. *Journal of Neuroscience* **6,** 2889–2899. ISSN: 0270-6474, 1529-2401 (1986).

251. Pittman, R. H. & Oppenheim, R. W. Neuromuscular blockade increases motoneurone survival during normal cell death in the chick embryo. *Nature* **271,** 364–366. ISSN: 1476-4687 (1978).
252. Oppenheim, R. W. & Núñez, R. Electrical stimulation of hindlimb increases neuronal cell death in chick embryo. *Nature* **295,** 57–59. ISSN: 1476-4687 (1982).
253. Vogel, M. & Landmesser, L. Distribution of fiber types in embryonic chick limb muscles innervated by foreign motoneurons. *Developmental Biology* **119,** 481–495. ISSN: 0012-1606 (1987).
254. McLennan, I. S. Differentiation of muscle fiber types in the chicken hindlimb. *Developmental Biology* **97,** 222–228. ISSN: 0012-1606 (1983).
255. Rafuse, V. F., Milner, L. D. & Landmesser, L. T. Selective Innervation of Fast and Slow Muscle Regions during Early Chick Neuromuscular Development. *Journal of Neuroscience* **16,** 6864–6877. ISSN: 0270-6474, 1529-2401 (1996).
256. Milner, L. D., Rafuse, V. F. & Landmesser, L. T. Selective Fasciculation and Divergent Pathfinding Decisions of Embryonic Chick Motor Axons Projecting to Fast and Slow Muscle Regions. *Journal of Neuroscience* **18,** 3297–3313. ISSN: 0270-6474, 1529-2401 (1998).
257. Landmesser, L. T. & O'Donovan, M. J. Activation patterns of embryonic chick hind limb muscles recorded in ovo and in an isolated spinal cord preparation. *The Journal of Physiology* **347,** 189–204. ISSN: 1469-7793 (1984).
258. Luxey, M., Berki, B., Heusermann, W., Fischer, S. & Tschopp, P. Development of the chick wing and leg neuromuscular systems and their plasticity in response to changes in digit numbers. *Developmental Biology* **458,** 133–140. ISSN: 0012-1606 (2020).
259. Calderó, J. *et al.* Peripheral Target Regulation of the Development and Survival of Spinal Sensory and Motor Neurons in the Chick Embryo. *Journal of Neuroscience* **18,** 356–370. ISSN: 0270-6474, 1529-2401 (Jan. 1, 1998).
260. Soula, C. *et al.* Distinct sites of origin of oligodendrocytes and somatic motoneurons in the chick spinal cord: oligodendrocytes arise from Nkx2.2-expressing progenitors by a Shh-dependent mechanism. *Development (Cambridge, England)* **128,** 1369–1379. ISSN: 0950-1991 (2001).
261. Lu *et al.* Common Developmental Requirement for Olig Function Indicates a Motor Neuron/Oligodendrocyte Connection. *Cell* **109,** 75–86. ISSN: 0092-8674 (2002).
262. Demireva, E. Y., Shapiro, L. S., Jessell, T. M. & Zampieri, N. Motor Neuron Position and Topographic Order Imposed by β- and γ-Catenin Activities. *Cell* **147,** 641–652. ISSN: 0092-8674 (2011).
263. Velten, J. *et al. The molecular logic of synaptic wiring at the single cell level* preprint (Developmental Biology, 2020).

264. Hayashi, S. *et al.* Protocadherin-17 Mediates Collective Axon Extension by Recruiting Actin Regulator Complexes to Interaxonal Contacts. *Developmental Cell* **30,** 673–687. ISSN: 1534-5807 (2014).
265. Stoeckli, E. T. Protocadherins: Not Just Neuron Glue, More Too! *Developmental Cell* **30,** 643–644. ISSN: 1534-5807 (2014).
266. Peek, S., Mah, K. M. & Weiner, J. A. Regulation of Neural Circuit Formation by Protocadherins. *Cellular and molecular life sciences : CMLS* **74,** 4133–4157. ISSN: 1420-682X (2017).
267. Lee, K.-S. *et al.* Runx2 Is a Common Target of Transforming Growth Factor β1 and Bone Morphogenetic Protein 2, and Cooperation between Runx2 and Smad5 Induces Osteoblast-Specific Gene Expression in the Pluripotent Mesenchymal Precursor Cell Line C2C12. *Molecular and Cellular Biology* **20,** 8783–8792 (2000).
268. Jeon, E.-J. *et al.* Bone Morphogenetic Protein-2 Stimulates Runx2 Acetylation *. *Journal of Biological Chemistry* **281,** 16502–16511. ISSN: 0021-9258, 1083-351X (2006).
269. Pierre, A., Pisselet, C., Monget, P., Monniaux, D. & Fabre, S. Testing the antagonistic effect of follistatin on BMP family members in ovine granulosa cells. *Reproduction Nutrition Development* **45,** 419–425. ISSN: 0926-5287, 1297-9708 (2005).
270. Jackson, H. E. & Ingham, P. W. Control of muscle fibre-type diversity during embryonic development: The zebrafish paradigm. *Mechanisms of Development* **130,** 447–457. ISSN: 0925-4773 (2013).
271. Alkaslasi, M. R. *et al.* Single nucleus RNA-sequencing defines unexpected diversity of cholinergic neuron types in the adult mouse spinal cord. *Nature Communications* **12,** 2471. ISSN: 2041-1723 (2021).
272. Blum, J. A. *et al.* Single-cell transcriptomic analysis of the adult mouse spinal cord reveals molecular diversity of autonomic and skeletal motor neurons. *Nature Neuroscience* **24,** 572–583. ISSN: 1546-1726 (2021).
273. Delile, J. *et al.* Single cell transcriptomics reveals spatial and temporal dynamics of gene expression in the developing mouse spinal cord. *Development* **146.** ISSN: 0950-1991, 1477-9129 (2019).
274. Rayon, T., Maizels, R. J., Barrington, C. & Briscoe, J. Single-cell transcriptome profiling of the human developing spinal cord reveals a conserved genetic programme with human-specific features. *Development* **148.** ISSN: 0950-1991 (2021).
275. Palser, A. L., Norman, A. L., Saffell, J. L. & Reynolds, R. Neural cell adhesion molecule stimulates survival of premyelinating oligodendrocytes via the fibroblast growth factor receptor. *Journal of Neuroscience Research* **87,** 3356–3368. ISSN: 1097-4547 (2009).
276. Traiffort, E., Zakaria, M., Laouarem, Y. & Ferent, J. Hedgehog: A Key Signaling in the Development of the Oligodendrocyte Lineage. *Journal of Developmental Biology* **4,** 28 (2016).
277. Klingseisen, A. *et al.* Oligodendrocyte Neurofascin Independently Regulates Both Myelin Targeting and Sheath Growth in the CNS. *Developmental Cell* **51,** 730–744.e6. ISSN: 1534-5807 (2019).

278. Zenker, J. *et al.* A role of peripheral myelin protein 2 in lipid homeostasis of myelinating schwann cells. *Glia* **62,** 1502–1512. ISSN: 1098-1136 (2014).
279. Moore, S. A. The Spinal Ependymal Layer in Health and Disease. *Veterinary Pathology* **53,** 746–753. ISSN: 0300-9858 (2016).
280. Djenoune, L. *et al.* Investigation of spinal cerebrospinal fluid-contacting neurons expressing PKD2L1: evidence for a conserved system from fish to primates. *Frontiers in Neuroanatomy* **8,** 26. ISSN: 1662-5129 (2014).
281. Jalalvand, E. *et al.* Cerebrospinal Fluid-Contacting Neurons Sense pH Changes and Motion in the Hypothalamus. *Journal of Neuroscience* **38,** 7713–7724. ISSN: 0270-6474, 1529-2401 (Aug. 29, 2018).
282. Wang, S. *et al.* The Neural Stem Cell Properties of PKD2L1+ Cerebrospinal Fluid-Contacting Neurons in vitro. *Frontiers in Cellular Neuroscience* **15,** 58. ISSN: 1662-5102 (2021).
283. Preibisch, S., Saalfeld, S. & Tomancak, P. Globally optimal stitching of tiled 3D microscopic image acquisitions. *Bioinformatics* **25,** 1463–1465. ISSN: 1367-4803 (2009).
284. Ginestet, C. ggplot2: Elegant Graphics for Data Analysis. *Journal of the Royal Statistical Society: Series A (Statistics in Society)* **174,** 245–246. ISSN: 1467-985X (2011).
285. Feregrino, C. & Tschopp, P. Assessing evolutionary and developmental transcriptome dynamics in homologous cell types. *Developmental Dynamics* **n/a,** 1–18. ISSN: 1097-0177 (n/a 2021).
286. Russ, D. E. *et al.* A harmonized atlas of mouse spinal cord cell types and their spatial organization. *Nature Communications* **12,** 5722. ISSN: 2041-1723 (2021).
287. Rozen, S. & Skaletsky, H. in *Bioinformatics Methods and Protocols* (eds Misener, S. & Krawetz, S. A.) 365–386 (Humana Press, Totowa, NJ, 1999). ISBN: 978-1-59259-192-3.
288. McGlinn, E. & Mansfield, J. H. in *Vertebrate Embryogenesis: Embryological, Cellular, and Genetic Methods* (ed Pelegri, F. J.) 259–292 (Humana Press, Totowa, NJ, 2011). ISBN: 978-1-61779-210-6.
289. Price, S. R. & Briscoe, J. The generation and diversification of spinal motor neurons: signals and responses. *Mechanisms of Development. The Chick in Developmental Biology* **121,** 1103–1115. ISSN: 0925-4773 (2004).
290. Eze, U. C., Bhaduri, A., Haeussler, M., Nowakowski, T. J. & Kriegstein, A. R. Single-cell atlas of early human brain development highlights heterogeneity of human neuroepithelial cells and early radial glia. *Nature Neuroscience* **24,** 584–594. ISSN: 1546-1726 (2021).
291. Hollyday, M. Organization of motor pools in the chick lumbar lateral motor column. *Journal of Comparative Neurology* **194,** 143–170. ISSN: 1096-9861 (1980).
292. Picelli, S. *et al.* Full-length RNA-seq from single cells using Smart-seq2. *Nature Protocols* **9,** 171–181. ISSN: 1750-2799 (2014).

293. Langlois, S. D., Morin, S., Yam, P. T. & Charron, F. Dissection and Culture of Commissural Neurons from Embryonic Spinal Cord. *JoVE (Journal of Visualized Experiments)*, e1773. ISSN: 1940-087X (2010).
294. Zheng, G. X. Y. *et al.* Massively parallel digital transcriptional profiling of single cells. *Nature Communications* **8,** 1–12. ISSN: 2041-1723 (2017).
295. Oppenheim, R. W., Qin-Wei, Y., Prevette, D. & Yan, Q. Brain-derived neurotrophic factor rescues developing avian motoneurons from cell death. *Nature* **360,** 755–757. ISSN: 1476-4687 (1992).
296. Yan, Q., Elliott, J. & Snider, W. D. Brain-derived neurotrophic factor rescues spinal motor neurons from axotomy-induced cell death. *Nature* **360,** 753–755. ISSN: 1476-4687 (1992).
297. Houenou, L. J., Oppenheim, R. W., Li, L., Lo, A. C. & Prevette, D. Regulation of spinal motoneuron survival by GDNF during development and following injury. *Cell and Tissue Research* **286,** 219–223. ISSN: 0302-766X, 1432-0878 (1996).
298. Fromental-Ramain, C. *et al.* Hoxa-13 and Hoxd-13 play a crucial role in the patterning of the limb autopod. *Development* **122,** 2997–3011. ISSN: 0950-1991 (1996).
299. Schaller, S. *et al.* Novel combinatorial screening identifies neurotrophic factors for selective classes of motor neurons. *Proceedings of the National Academy of Sciences* **114,** E2486–E2493. ISSN: 0027-8424, 1091-6490 (2017).
300. Gurfinkel, V. S. & Shik, M. L. in *Motor Control* (eds Gydikov, A. A., Tankov, N. T. & Kosarov, D. S.) 217–234 (Springer US, Boston, MA, 1973). ISBN: 978-1-4613-4504-6 978-1-4613-4502-2.
301. Mansuit, R. & Herrel, A. The Evolution of Appendicular Muscles During the Fin-to-Limb Transition: Possible Insights Through Studies of Soft Tissues, a Perspective. *Frontiers in Ecology and Evolution* **9,** 508. ISSN: 2296-701X (2021).
302. Zakany, J. & Duboule, D. The role of Hox genes during vertebrate limb development. *Current Opinion in Genetics & Development. Pattern formation and developmental mechanisms* **17,** 359–366. ISSN: 0959-437X (2007).
303. Hall, B. K. *Fins into Limbs: Evolution, Development, and Transformation* (University of Chicago Press, Sept. 15, 2008).
304. Clack, J. A. *Gaining Ground, Second Edition: The Origin and Evolution of Tetrapods* 2nd ed. ISBN: 978-0-253-35675-8 (Indiana University Press, 2012).
305. Malik, S. Polydactyly: phenotypes, genetics and classification. *Clinical Genetics* **85,** 203–212. ISSN: 1399-0004 (2018).
306. Martin, P. Tissue patterning in the developing mouse limb. *International Journal of Developmental Biology* **34,** 323–336. ISSN: 0214-6282, 1696-3547 (May 1, 2002).
307. Kherdjemil, Y. *et al.* Evolution of Hoxa11 regulation in vertebrates is linked to the pentadactyl state. *Nature* **539,** 89–92. ISSN: 1476-4687 (2016).
308. Wanson, G. J. & Lewis, J. The timetable of innervation and its control in the chick wing bud. *Development* **71,** 121–137. ISSN: 0950-1991, 1477-9129 (1982).
309. Livet, J. *et al.* Transgenic strategies for combinatorial expression of fluorescent proteins in the nervous system. *Nature* **450,** 56–62. ISSN: 1476-4687 (Nov. 2007).

310. Cai, D., Cohen, K. B., Luo, T., Lichtman, J. W. & Sanes, J. R. Improved tools for the Brainbow toolbox. *Nature Methods* **10,** 540–547. ISSN: 1548-7105 (2013).
311. Loulier, K. *et al.* Multiplex Cell and Lineage Tracking with Combinatorial Labels. *Neuron* **81,** 505–520. ISSN: 0896-6273 (2014).
312. Weissman, T. A. & Pan, Y. A. Brainbow: New Resources and Emerging Biological Applications for Multicolor Genetic Labeling and Analysis. *Genetics* **199,** 293–306. ISSN: 0016-6731 (2015).
313. Kaprielian, Z., Runko, E. & Imondi, R. Axon guidance at the midline choice point. *Developmental Dynamics* **221,** 154–181. ISSN: 1097-0177 (2001).
314. Kramer, E. R. *et al.* Cooperation between GDNF/Ret and ephrinA/EphA4 Signals for Motor-Axon Pathway Selection in the Limb. *Neuron* **50,** 35–47. ISSN: 0896-6273 (2006).
315. Kolodkin, A. L. in *Progress in Brain Research* (ed Callow, J. A.) 115–132 (Elsevier, Jan. 1, 1998).
316. Xu & Henkemeyer. Ephrin reverse signaling in axon guidance and synaptogenesis. *Seminars in cell & developmental biology* **23,** 58–64. ISSN: 1084-9521 (2012).
317. Noguchi, K. *et al.* Expression patterns of Sema3A in developing amniote limbs: With reference to the diversification of peripheral nerve innervation. *Development, Growth & Differentiation* **59,** 270–285. ISSN: 1440-169X (2017).
318. Croteau, L.-P., Kao, T.-J. & Kania, A. Ephrin-A5 potentiates netrin-1 axon guidance by enhancing Neogenin availability. *Scientific Reports* **9,** 12009. ISSN: 2045-2322 (2019).
319. Tomaszewski, R. & Bulandra, A. Ulnar dimelia-diagnosis and management of a rare congenital anomaly of the upper limb. *Journal of Orthopaedics* **12,** S121–S124. ISSN: 0972-978X (Suppl 1 2015).
320. Mukouyama, Y.-s., Shin, D., Britsch, S., Taniguchi, M. & Anderson, D. J. Sensory Nerves Determine the Pattern of Arterial Differentiation and Blood Vessel Branching in the Skin. *Cell* **109,** 693–705. ISSN: 0092-8674 (2002).
321. Li, W. *et al.* Peripheral Nerve-Derived CXCL12 and VEGF-A Regulate the Patterning of Arterial Vessel Branching in Developing Limb Skin. *Developmental Cell* **24,** 359–371. ISSN: 1534-5807 (2013).
322. Makita, T. Nerve Control of Blood Vessel Patterning. *Developmental cell* **24,** 340–341. ISSN: 1534-5807 (2013).
323. Marangoz, S. & Leblebicioğlu, G. Thumb Polydactyly With Radius Hypoplasia—A Case Report. *The Journal of Hand Surgery* **31,** 1667–1670. ISSN: 0363-5023 (2006).
324. Philandrianos, C., SALAZARD, B. & CASANOVA, D. Two Rare Cases of Association of Thumb Hypoplasia and Polydactyly of the Homolateral Foot. *Journal of Hand Surgery (European Volume)* **34,** 125–127. ISSN: 1753-1934 (2009).
325. Wieczorek, D. *et al.* A specific mutation in the distant sonic hedgehog (SHH) cis-regulator (ZRS) causes Werner mesomelic syndrome (WMS) while complete ZRS duplications underlie Haas type polysyndactyly and preaxial polydactyly

(PPD) with or without triphalangeal thumb. *Human Mutation* **31,** 81–89. ISSN: 1098-1004 (2010).

326. Jameel, J., Khan, A. Q., Ahmad, S. & Abbas, M. Ulnar dimelia variant: a case report. *Journal of Orthopaedics and Traumatology : Official Journal of the Italian Society of Orthopaedics and Traumatology* **12,** 163–165. ISSN: 1590-9921 (2011).
327. Oberg, K. C., Feenstra, J. M., Manske, P. R. & Tonkin, M. A. Developmental Biology and Classification of Congenital Anomalies of the Hand and Upper Extremity. *The Journal of Hand Surgery* **35,** 2066–2076. ISSN: 0363-5023 (2010).
328. Al-Qattan, M. M. The association between preaxial polydactyly and radial longitudinal deficiency in syndromic cases: a report on nine families. *Journal of Hand Surgery (European Volume)* **43,** 744–750. ISSN: 1753-1934 (2018).
329. Al-Qattan, M. M. Zone of Polarizing Activity Regulatory Sequence Mutations/Duplications with Preaxial Polydactyly and Longitudinal Preaxial Ray Deficiency in the Phenotype: A Review of Human Cases, Animal Models, and Insights Regarding the Pathogenesis. *BioMed Research International* **2018,** e1573871. ISSN: 2314-6133 (2018).
330. Lam, W. L. *et al.* Experimental evidence that preaxial polydactyly and forearm radial deficiencies may share a common developmental origin. *Journal of Hand Surgery (European Volume)* **44,** 43–50. ISSN: 1753-1934 (2019).

BIANKA ANNA BERKI

biankaanna.berki@gmail.com https://www.linkedin.com/in/bianka-anna-berki/

WORK EXPERIENCE

Research Associate

University of Basel – Laboratory of Prof. Dr. Patrick Tschopp

Jan 2022 – April 2022 Basel, CH

1. Transfer of experimental expertise to senior lab members
2. Completion and submission of a first-author paper

PhD in Developmental Neurobiology

University of Basel – Laboratory of Prof. Dr. Patrick Tschopp

Oct. 2017 – Dec. 2021 Basel, CH

Under the supervision of Dr. Patrick Tschopp and Dr. Maëva Luxey
Project: Plasticity of the neuromuscular system in response to changes in dactyly

1. Micro-dissections and experimental embryology
2. Lightsheet microscopy and development of a lightsheet data analysis pipeline with Arivis and Imaris to visualize avian limb neuromuscular system in 3D
3. Optimization of neural tissue dissociation for single cell RNA-sequencing (10X Chromium system)
4. Establisment of workflow to disaggregate, culture motoneurons for Smart-seq2

Master's Internship

University of Toulouse III - Laboratory of Dr. Muriel Laffargue

Oct. 2016 – Jun. 2017 Toulouse, FR

Under the supervision of Dr. Damien Ramel
Project: Role of CXCL12/PI3Kgamma pathway in the migration of breast cancer cells

1. Optimization of transfection conditions for various cell types
2. Increase the efficiency of immunostainings on cultured cells
3. Improvement of culture conditions for video microscopy of migrating cells

Master's Internship

University of Toulouse III - Laboratory of Dr. Xiaobo Wang

Oct. 2015 – Jan. 2016 Toulouse, FR

Under the supervision of Dr. Damien Ramel
Project: Investigating the role of PI3K/Akt pathway in the migration of border cells (*D. melanogaster*)

1. Fly stock maintenance and fly crossing
2. siRNA expression in the border cells against actors of the PI3K/Akt pathway and assessment of the migration defect

EDUCATION

MSc. in Genetics, Cell and Developmental Biology

University of Toulouse III

Sept 2015 – Jun 2017 Toulouse, FR

- Courses focused on genomics, genetics and cell signalling during development
- One week courses on Next-Generation Sequencing and visit of the Genotoul Sequencing Facility

BSc. in Cell Biology and Physiology

University of Toulouse III

Sept 2012 – Jun 2015 Toulouse, FR

- **Scholarship** granted by the French Government (Bourse du Gouvernement Français – Campus France)
- Courses on basic molecular biology, cell biology and cell signaling in different model organisms

Hungarian - French Bilingual High School

Mikszáth Kálmán Gimnázium és Kollégium

Sept 2007 – Jun 2012 Pásztó, HU

LANGUAGES

Hungarian – Native
French – Bilingual
English – Fluent
German – Conversational

SOFT SKILLS

Dedicated Team Worker
Outstanding Communication Skills
Excellent Time-Management
Organized and Meticulous Documentation
Self-Motivated and Dynamic

RELEVANT LAB SKILLS

Molecular Biology and Genomics

1. DNA/RNA/protein extraction from tissue and cultured cells
2. PCR; RT-qPCR; *in vitro* transcription; RNA probe production, primer designing
3. **Cloning** into various bacterial and viral vectors
4. Library preparation for NGS (Chromium Next GEM Single Cell 3' v3.1: Dual Index Libraries)
5. Sanger sequencing of vectors

Embryology and Cell Biology

1. Micro-injections; electroporation; various micromanipulations of embryos
2. Culture of primary, immortalised and cancerous cells (BSL1 and BSL2)
3. Transfection of cells (Lipofectamine)
4. Tissue dissociation (embryonic)
5. Cell counting and viability assessment (Trypan blue and Cellometer)

Histology and Imaging

1. Snap freezing; cryosectioning; vibratome sectioning
2. Hematoxylin and Eosin staining; fluorescent immunostaining; *in situ* hybridisation
3. Brightfield microscopy; video microscopy; confocal microscopy (Olympus FV3000, Leica Sp5, Zeiss LSM 710/780); lightsheet microscopy (Zeiss Z1)
4. ImageJ/Fiji; Arivis; Imaris; Huygens (HRM) deconvolution

Software Skills

1. Microsoft Office
2. SnapGene; ApE; Quartzy (lab organization)
3. Adobe Illustrator, Adobe Premier Pro (video editing)
4. R (statistics and data visualization); SLURM, LaTex

PUBLICATIONS

Journal Articles

- Development of the chick wing and leg neuromuscular systems and their plasticity in response to changes in digit numbers – Luxey*, **Berki*** Wolf Heusermann, Sabrina Fischer, Patrick Tschopp – Dev. Biol., 2020 – *co-first authors
- A method to investigate muscle target-specific transcriptional signatures of single motor neurons – **Bianka Berki**, Fabio Sacher, Antoine Fages, Patrick Tschopp, Maëva Luxey - Dev. Dynamics, 2022
- Plasticity and constraint in the vertebrate limb neuromuscular system – **Bianka Berki**, Maëva Luxey, Patrick Tschopp – Frontiers, invited review (*in preparation*)
- Paracrine regulation of neural crest EMT by placodal MMP28 – Nadège Gouignard, Anne Bibonne, Joao Mata, Fernanda Bajanca, **Bianka Berki**, Elias Barriga, Jean-Pierre Saint Jeannet, Eric Theveneau (on BioRxiv)

TEACHING EXPERIENCE

Block Course

University of Basel –DUW

2018 – 2022 Basel, CH

- Each year, supervision of two students during two month in a "mini-project" furthering my PhD project
- Tasks: Proposal writing, introduction to laboratory safety and work in a research lab environment, embryo dissection, pipetting, immunohistochemistry, *in situ* hybridization on sections and whole mount

Tutoring of BSc. Students

University of Basel

2019 Basel, CH

- Semester course for first year students in order to complement their high school level biology knowledge and bring them to the same level

REFERENCES

Prof. Dr. Patrick Tschopp – PhD Supervisor
@ patrick.tschopp@unibas.ch
Zoological Institute, University of Basel
Vesalgasse 1
4051 Basel
+41 61 207 56 49

Dr. Maëva Luxey – PhD Co-supervisor
@ maeva.luxey@unibas.ch
Zoological Institute, University of Basel
Vesalgasse 1
4051 Basel
+41 61 207 59 80

Dr. Damien Ramel – MSc. Supervisor
@ damien.ramel@inserm.fr
Institut des Maladies Métaboliques et Cardiovasculaires
1 avenue du Professeur Jean Poulhès
31432 Toulouse Cedex 4
+33 5 31 22 41 45